QUANTITATIVE PREDICTION OF ADSORPTION AND DIFFUSION IN PURE-SILICA AND CATIONIC ZEOLITES

A Dissertation
Presented to
The Academic Faculty

by

John Findley

In Partial Fulfillment
of the Requirements for the Degree
Doctor of Philosophy in the
School of Chemical and Biomolecular Engineering

Georgia Institute of Technology
August 2020

QUANTITATIVE PREDICTION OF ADSORPTION AND DIFFUSION IN PURE-SILICA AND CATIONIC ZEOLITES

Approved by:

Dr. David S. Sholl, Advisor
School of Chemical and Biomolecular Engineering
Georgia Institute of Technology

Dr. Sankar Nair
School of Chemical and Biomolecular Engineering
Georgia Institute of Technology

Dr. Christopher W. Jones
School of Chemical and Biomolecular Engineering
Georgia Institute of Technology

Dr. Seung Soon Jang
School of Materials Science and Engineering
Georgia Institute of Technology

Dr. Ryan P. Lively
School of Chemical and Biomolecular Engineering
Georgia Institute of Technology

Date Approved: July 23, 2020

To my family.

ACKNOWLEDGEMENTS

First and foremost, I would like to thank my thesis advisor, Dr. David Sholl, for taking me in to his group after I started my second year at Georgia Tech without an advisor. He gave me the freedom to approach problems in ways I saw fit and asked insightful questions to make sure that I paid attention to the motivation behind the research. During my time in this group, I gained valuable written and oral communication skills, as well as time-management skills that I know I will be able to use for the rest of my life.

I would also like to thank my committee members Dr. Christopher Jones, Dr. Ryan Lively, Dr. Sankar Nair, and Dr. Seung Soon Jang for their guidance and interest in my PhD project.

Thank you to, Exxon Mobil Research and Engineering for funding my project. I especially thank Dr. Peter Ravikovitch for his knowledge and insight into both the computational and experimental aspects of adsorption and diffusion in zeolites. His suggestions always kept our projects moving forward.

Thank you to my fellow members of the Sholl group, both past and present, for making my time at Georgia Tech an enjoyable experience. I would like to thank Ross Verploegh and Rebecca Han for being some of my first and best friends I made in the group. I would like to thank Dr. Salah Boulfelfel, Dr. Hanjun Fang, Dr. Jifeng Sun, Omar Knio, and Alan Daou for the great discussions we had while working on the Exxon projects. I would especially like to thank Salah and Hanjun for their hard work and collaboration on

our force-field development projects. This work could not have been completed without Salah's work on molecular dynamics and Hanjun's work on CC-corrections.

Outside of the Sholl group, I was able to spend time with many great friends. The weekly post-seminar Costco trips with Thomas, Jay, Julian, and Jason were always one of the high points of every week. I miss the deals and samples that were a Wednesday staple for about 4 years. I would also like my friends from home (including but not limited to June, Bubba, Bill, Parker, Ryan, and Joseph). It is always great visiting you all during holidays and the occasional weekend. I also would like to thank my roommate, Daniel Struk, for being a great friend (and neighbor back home) for 23 years.

Most importantly, I would like to thank my family. I am thankful to my parents, Tom Findley and Robin Findley, for their support and encouragement. I was especially inspired by my mother's choice to return to school and get a nursing degree around the time I started at Georgia Tech. It taught me that one can always learn new skills and change careers at any point in life. I would like to thank my sisters, Ally Findley and Laurie Findley, for the fun visits home in December. I would not be where I am today without my family's love and support.

John Findley, Georgia Tech, July 2020

TABLE OF CONTENTS

LIST OF TABLES

LIST OF FIGURES

LIST OF SYMBOLS AND ABBREVIATIONS

DFT	Density Functional Theory
DFT/CC	Density Functional Theory/Coupled-Cluster Corrected
GCMC	Grand Canonical Monte Carlo
CCFF	Coupled-cluster Force Field
LJ	Lennard-Jones
MD	Molecular Dynamics
TST	Transition State Theory
vdW	van der Waals

SUMMARY

Zeolites are a class of nanoporous aluminosilicate materials. They are often used industrially for separations and catalysis because of their low cost and high thermal stability. The variety of exchangeable cations, Si/Al ratio and aluminum distribution can affect the adsorption and diffusion properties of these materials. Molecular simulations provide an inexpensive, well-defined way to study the effects of these properties on measurable quantities, such as adsorption and diffusion. In this work, we developed methods to examine the effects of aluminum distribution in zeolites and more accurate force fields for predicting adsorption and diffusion. We first examined the effect of aluminum distribution on CO_2 adsorption in cationic zeolites. We observed a significant dependence of extra-framework cation distributions and CO_2 adsorption properties on aluminum distribution. This indicated that aluminum ordering should be considered when screening cationic zeolites for CO_2 adsorption and that CO_2 adsorption isotherms can be used to probe aluminum distribution. Next, we developed accurate, transferable force field methods that are used to examine adsorption and diffusion in both pure-silica and cationic zeolites. In both cases, the force fields were fit to reproduce DFT/CC energies of both transition state configurations and energy minimum configurations to enable accurate predictions for both adsorption and diffusion data for a wide array of adsorbates in both pure-silica zeolites and cationic zeolites. Overall, in this work we developed more transferable tools for predicting both adsorption and diffusion in both pure-silica and cationic zeolites, which previous classical simulation methods were limited to predicting adsorption for pure-silica, Na-exchanged and K-exchanged zeolites.

CHAPTER 1. INTRODUCTION

1.1 Zeolites

Zeolites are a class of crystalline nanoporous materials that are widely used in the chemical industry for separations and catalysis applications. Zeolite structures are made of tetrahedral building units, which consist of a T-atom, which is usually silicon or aluminum, coordinated to four oxygen atoms. These oxygens form the vertices of the tetrahedral building units. All 245 distinct experimentally synthesized zeolite topologies can be constructed based on these units[1]. These topologies can vary widely in terms of pore shape and pore size, allowing them to be used for separations.

When aluminum is present as tetrahedral atoms in a zeolite, extra-framework cations are required to balance the charge and stabilize the structure. These zeolites are called cationic zeolites. The extra-framework cations can act as adsorption sites for polar and quadrupolar molecules such as H_2O and CO_2 because of strong electrostatic interactions between the cations and adsorbates. Because cationic zeolites are very hydrophilic, they are often used industrially for water removal. One example is the desiccation of petroleum cracking products[2]. Also, strong interactions with quadrupolar adsorbates such as CO_2, makes cationic zeolites useful for CO_2/CH_4 and CO_2/N_2 separations[3-6]. When zeolites are exchanged with H^+, the extra-framework protons act as Brønsted acid sites, which can be used as catalytic sites[7] for applications such as fluid-catalytic cracking[8].

The performance of zeolites can be determined by the amount of Al, as described by the Si/Al ratio, the species of extra-framework cations and the distribution of Al. In many cases, the Al distribution among possible sites is not experimentally known. The most widely accepted rule governing aluminum distribution is Lowenstein's rule, which prohibits Al-O-Al linkages. Additional heuristics have been proposed to describe Al distribution, such as Dempsey's rule[9], which states that the number of Al-O-Si-O-Al linkages are minimized for Si/Al > 1. These generalizations are applicable to all zeolite topologies and compositions, nevertheless, the details of Al distribution are often the result of synthesis conditions[7, 10-12]. In order to effectively screen zeolites for separations applications, a detailed understanding of the adsorbate-adsorbent interactions as well as a model that accounts of differences in adsorbate, zeolite topology, composition, and Al distribution is required.

1.2 Classical Simulations

Classical atomistic simulations use simple analytical potentials called force fields (FFs) to describe interaction energies and forces between atoms or molecules. In this work, all interactions will be described by pairwise potentials. Because force fields allow for forces and energies to be evaluated quickly, classical simulations are an efficient method for determining macroscopic properties such as adsorption isotherms[13, 14], heats of adsorption[15], self-diffusivities[16], vapor-liquid equilibria[17-19], and equations of state[20], which rely on averaging properties over a large ensemble of thousands or millions of configurations. This makes classical simulations an effective tool for materials screening applications[21, 22].

The accuracy of FF-based approaches is determined by the accuracy of the FF itself. Generic FFs, which offer reasonable predictions for simple systems, fail to quantitatively describe adsorption and diffusion in nanoporous materials[22]. Experimentally-derived FFs are fit to reproduce experimental data such as adsorption isotherms, vapor-liquid equilibria or even cation distributions in a zeolite. FFs fit to experimental adsorption isotherms offer good predictions for adsorption in some zeolites, but they are often not transferable to zeolites that are compositionally or topologically different from the source of experimental data[22, 23]. Additionally, experimentally-derived FFs that are fit to adsorption data cannot be expected to also predict diffusion data[24]. First-principles-derived FFs are fit to reproduce energies based on Quantum Mechanics (QM) simulations. These FFs offer true predictions for material properties in the absence of experimental data. However, their accuracy depends on the level of theory used in the QM calculations[14, 22].

1.2.1 Monte Carlo Methods

Monte Carlo (MC) methods use repeated random sampling to numerically address problems with many coupled degrees of freedom. In physical chemistry, Monte Carlo methods are commonly used to determine the equations of state for gases, vapor-liquid equilibrium, adsorption isotherms[13, 14], heats of adsorption[15], Henry's Law coefficients, and distributions of atoms in disordered structures[25].

MC methods can be used to determine equilibrium properties under a given set of constraints. In these simulations, random trial moves such as translation, rotation, insertion and deletion are performed and either accepted or rejected with probabilities based on detailed balance criteria, which states that for a system at equilibrium[26]

$$\pi_i P_{ij} = \pi_j P_{ji} \tag{1.1}$$

Here π_i and π_j are the equilibrium probabilities of the system being observed in state i and state j respectively and P_{ij} is the probability of the system transitioning from state i to state j. The equilibrium probabilities, π, are determined based on the constraints of the ensemble.

One of the most commonly used MC methods used in molecular simulations is Grand Canonical Monte Carlo (GCMC), which generates configurations with a fixed chemical potential, μ, volume, V, and temperature, T.[20] The chemical potential, μ, can be determined based on the fugacity. The fugacity can be determined based on an equation of state, such as Peng-Robinson. Because the number of molecules, N, is not fixed in a GCMC simulation, equilibrium adsorption isotherms can be calculated by taking the average of the number of molecules, <N>, over the GCMC simulation. Isosteric heats of adsorption can also be calculated from GCMC simulations based on a fluctuation formula[15, 27].

$$Q_{st} = RT - \frac{< NV > - < N >< V >}{< N^2 > - < N >^2} \tag{1.1}$$

where N is the number of molecules, V is the sum of interactions of all adsorbed molecules with both the zeolite and one another and < > denotes the ensemble average.

Another type of Monte Carlo simulation that is used to study zeolites is called Parallel Tempering[25] (PT), which is a form of replica-exchange Monte Carlo that can be used to determine the distribution of extra-framework cations in a zeolite framework.. This method uses NVT (fixed number, volume, temperature) MC simulations at multiple different temperatures in parallel and allows configurations to swap between different

temperatures. This approach can be useful when determining a global minimum energy configuration in systems with many deep local minima, such as for extra-framework cations in a cationic zeolite.

1.2.2 Molecular Dynamics

In classical Molecular Dynamics (MD), interatomic forces are calculated based on force fields and atomic coordinates are updated by integrating Newton's Second Law. In zeolites, these methods are used to compute diffusivities, which are based on the mean-squared displacement of the adsorbate[28]. For slow diffusion processes, restrained MD and Transition State Theory (TST) can be applied to determine hopping rates and then diffusivities[29].

1.3 Quantum Chemistry Methods

Quantum mechanical (QM) simulations provide a more accurate description of intermolecular interactions than classical simulations. Highly accurate QM calculations such as Coupled-Cluster (such as CCSD(T)) have computational complexities that scale as $O(N^7)$ where N is the number of electrons[30]. Because of the high computational cost, only simulations containing clusters of tens of atoms are feasible at this level of theory. Therefore, these methods cannot be applied to large periodic structures such as zeolites.

Density Functional Theory (DFT) describe the properties of a many electron system using functionals which depend on electron density[31], making the problems less computationally expensive. One issue with DFT is that it does not accurately predict the energies of dispersion interactions. Methods such as DFT-D[32] and DFT/CC[33, 34] have been

developed to correct this. DFT/CC is a compromise between DFT and more accurate QM methods. This method takes the difference between DFT energies and CCSD(T) energies to make a CC-correction. This CC-correction is applied to DFT energies in periodic systems to improve the accuracy of calculations. The DFT/CC method has been among the best methods of predicting the energetics of adsorbate-adsorbent interactions in zeolites[13, 23, 35, 36]. Force fields fit to DFT/CC energies have also been shown to accurately predict macroscopic properties such as adsorption isotherms and diffusivities in zeolites without relying on experimental data[13, 21, 23].

1.4 Thesis Summary

The objective of this thesis is to develop more transferable, accurate models and methods to predict adsorption and diffusion in pure-silica and cationic zeolites using the methods mentioned above.

In Chapter 2, we discuss the effect of aluminum ordering on CO_2 adsorption in Na-exchanged and K-exchanged zeolites. This was the first study to quantify aluminum distribution using a short-range order parameter and systematically examine the effect of Al distribution on CO_2 adsorption isotherms, CO_2 isosteric heats of adsorption and cation distributions.

Chapter 3 and Chapter 4 focus on improving the force field methods that are used to examine adsorption and diffusion in pure-silica and cationic zeolites respectively. In Chapter 3, we demonstrate that fitting a first-principles-based FF to reproduce DFT/CC energies of both transition state configurations and energy minimum configurations can accurately predict both adsorption and diffusion data for a wide array of adsorbates in pure-

silica zeolites In Chapter 3, we also benchmarked the performance of our CCFF against other FFs from the literature for adsorption and diffusion in silica zeolites.

Chapter 4 extends the CCFF methodology to zeolites exchanged with monovalent cations. This force field was able to accurately predict cation distributions and adsorption isotherms in zeolites exchanged with Li, Na, K, Rb and Cs-exchanged zeolites as well as many mixed-cation zeolites. These true predictions will allow for the accurate computational screening of zeolites across topology, composition and Al distribution.

1.5 Chapter 1 References

1. Baerlocher, C.; McCusker, L. B.; Olson, D. H., *Atlas of zeolite framework types*. Elsevier: 2007.

2. Williams, D. B. G.; Lawton, M., Drying of organic solvents: quantitative evaluation of the efficiency of several desiccants. *The Journal of organic chemistry* **2010,** *75* (24), 8351-8354.

3. Palomino, M.; Corma, A.; Rey, F.; Valencia, S., New Insights on CO_2− Methane separation using LTA zeolites with different Si/Al ratios and a first comparison with MOFs. *Langmuir* **2010,** *26* (3), 1910-1917.

4. Remy, T.; Gobechiya, E.; Danaci, D.; Peter, S.; Xiao, P.; Van Tendeloo, L.; Couck, S.; Shang, J.; Kirschhock, C.; Singh, R., Biogas upgrading through kinetic separation of carbon dioxide and methane over Rb-and Cs-ZK-5 zeolites. *Rsc Adv* **2014,** *4* (107), 62511-62524.

5. Shang, J.; Li, G.; Singh, R.; Gu, Q.; Nairn, K. M.; Bastow, T. J.; Medhekar, N.; Doherty, C. M.; Hill, A. J.; Liu, J. Z., Discriminative separation of gases by a "molecular trapdoor" mechanism in chabazite zeolites. *Journal of the American Chemical Society* **2012,** *134* (46), 19246-19253.

6. Shang, J.; Li, G.; Singh, R.; Xiao, P.; Liu, J. Z.; Webley, P. A., Determination of composition range for "molecular trapdoor" effect in chabazite zeolite. *The Journal of Physical Chemistry C* **2013,** *117* (24), 12841-12847.

7. Di Iorio, J. R.; Gounder, R., Controlling the Isolation and Pairing of Aluminum in Chabazite Zeolites Using Mixtures of Organic and Inorganic Structure-Directing Agents. *Chemistry of Materials* **2016,** *28* (7), 2236-2247.

8. Blauwhoff, P.; Gosselink, J.; Kieffer, E.; Sie, S.; Stork, W., Zeolites as catalysts in industrial processes. In *Catalysis and Zeolites*, Springer: 1999; pp 437-538.

9. Dempsey, E.; Kuehl, G. H.; Olson, D. H., Variation of the lattice parameter with aluminum content in synthetic sodium faujasites. Evidence for ordering of the framework ions. *The Journal of Physical Chemistry* **1969,** *73* (2), 387-390.

10. Gábová, V.; Dědeček, J.; Čejka, J., Control of Al distribution in ZSM-5 by conditions of zeolite synthesis. *Chem Commun* **2003,** (10), 1196-1197.

11. Pinar, A. B.; Gómez-Hortigüela, L.; McCusker, L. B.; Pérez-Pariente, J., Controlling the Aluminum Distribution in the Zeolite Ferrierite via the Organic Structure Directing Agent. *Chemistry of Materials* **2013,** *25* (18), 3654-3661.

12. Herrero, C. P., Short-range order of the silicon, aluminum distribution on the faujasite framework. *The Journal of Physical Chemistry* **1991,** *95* (8), 3282-3288.

13. Fang, H.; Kamakoti, P.; Ravikovitch, P. I.; Aronson, M.; Paur, C.; Sholl, D. S., First principles derived, transferable force fields for CO_2 adsorption in Na-exchanged cationic zeolites. *Physical Chemistry Chemical Physics* **2013,** *15* (31), 12882-12894.

14. Fang, H.; Kamakoti, P.; Zang, J.; Cundy, S.; Paur, C.; Ravikovitch, P. I.; Sholl, D. S., Prediction of CO_2 adsorption properties in zeolites using force fields derived from periodic dispersion-corrected DFT calculations. *The Journal of Physical Chemistry C* **2012,** *116* (19), 10692-10701.

15. Hyla, A. S.; Fang, H.; Boulfelfel, S. E.; Muraro, G.; Paur, C.; Strohmaier, K.; Ravikovitch, P. I.; Sholl, D. S., Significant temperature dependence of the isosteric heats of adsorption of gases in zeolites demonstrated by experiments and molecular simulations. *The Journal of Physical Chemistry C* **2019,** *123* (33), 20405-20412.

16. Fang, H.; Findley, J.; Muraro, G.; Ravikovitch, P. I.; Sholl, D. S., A Strong Test of Atomically-detailed Models of Molecular Adsorption in Zeolites Using Multi-laboratory Experimental Data for CO_2 Adsorption in Ammonium ZSM-5. *The Journal of Physical Chemistry Letters* **2019**.

17. Harris, J. G.; Yung, K. H., Carbon dioxide's liquid-vapor coexistence curve and critical properties as predicted by a simple molecular model. *The Journal of Physical Chemistry* **1995,** *99* (31), 12021-12024.

18. Makrodimitris, K.; Papadopoulos, G. K.; Theodorou, D. N., Prediction of permeation properties of CO_2 and N_2 through silicalite via molecular simulations. *The Journal of Physical Chemistry B* **2001,** *105* (4), 777-788.

19. Potoff, J. J.; Siepmann, J. I., Vapor–liquid equilibria of mixtures containing alkanes, carbon dioxide, and nitrogen. *AIChE journal* **2001,** *47* (7), 1676-1682.

20. Frenkel, D.; Smit, B., *Understanding molecular simulation: from algorithms to applications*. Elsevier: 2001; Vol. 1.

21. Fang, H.; Kulkarni, A.; Kamakoti, P.; Awati, R.; Ravikovitch, P. I.; Sholl, D. S., Identification of high-CO_2-capacity cationic zeolites by accurate computational screening. *Chemistry of Materials* **2016,** *28* (11), 3887-3896.

22. Fang, H.; Demir, H.; Kamakoti, P.; Sholl, D. S., Recent developments in first-principles force fields for molecules in nanoporous materials. *Journal of Materials Chemistry A* **2014,** *2* (2), 274-291.

23. Fang, H.; Awati, R.; Boulfelfel, S. E.; Ravikovitch, P. I.; Sholl, D. S., First-principles-derived force fields for CH_4 adsorption and diffusion in siliceous zeolites. *The Journal of Physical Chemistry C* **2018,** *122* (24), 12880-12891.

24. Jee, S. E.; Sholl, D. S., Carbon dioxide and methane transport in DDR zeolite: insights from molecular simulations into carbon dioxide separations in small pore zeolites. *Journal of the American Chemical Society* **2009,** *131* (22), 7896-7904.

25. Beauvais, C.; Guerrault, X.; Coudert, F.-X.; Boutin, A.; Fuchs, A. H., Distribution of Sodium Cations in Faujasite-Type Zeolite: A Canonical Parallel Tempering Simulation Study. *The Journal of Physical Chemistry B* **2004,** *108* (1), 399-404.

26. Hastings, W. K., Monte Carlo sampling methods using Markov chains and their applications. *Biometrika* **1970,** *57* (1), 97-109.

27. Burtch, N. C.; Jasuja, H.; Dubbeldam, D.; Walton, K. S., Molecular-level insight into unusual low pressure CO_2 affinity in pillared metal–organic frameworks. *Journal of the American Chemical Society* **2013,** *135* (19), 7172-7180.

28. Frenkel, D.; Smit, B., Chapter 6 - Molecular Dynamics in Various Ensembles. In *Understanding Molecular Simulation (Second Edition)*, Academic Press: San Diego, 2002; pp 139-163.

29. Awati, R. V.; Ravikovitch, P. I.; Sholl, D. S., Efficient and accurate methods for characterizing effects of framework flexibility on molecular diffusion in zeolites: CH_4 diffusion in eight member ring zeolites. *The Journal of Physical Chemistry C* **2013,** *117* (26), 13462-13473.

30. Pitoňák, M.; Neograd y, P.; Černý, J.; Grimme, S.; Hobza, P., Scaled MP3 non-covalent interaction energies agree closely with accurate CCSD (T) benchmark data. *ChemPhysChem* **2009,** *10* (1), 282-289.

31. Sholl, D.; Steckel, J. A., *Density functional theory: a practical introduction*. John Wiley & Sons: 2011.

32. Grimme, S., Semiempirical GGA-type density functional constructed with a long-range dispersion correction. *J Comput Chem* **2006,** *27* (15), 1787-1799.

33. Bludsky, O.; Rubes, M.; Soldan, P.; Nachtigall, P., Investigation of the benzene-dimer potential energy surface: DFT/CCSD(T) correction scheme. *J Chem Phys* **2008,** *128* (11), 114102.

34. Nachtigall, P.; Delgado, M. R.; Nachtigallova, D.; Areán, C. O., The nature of cationic adsorption sites in alkaline zeolites—single, dual and multiple cation sites. *Physical Chemistry Chemical Physics* **2012,** *14* (5), 1552-1569.

35. Pulido, A.; Delgado, M.; Bludský, O.; Rubeš, M.; Nachtigall, P.; Areán, C. O., Combined DFT/CC and IR spectroscopic studies on carbon dioxide adsorption on the zeolite H-FER. *Energy & Environmental Science* **2009,** *2* (11), 1187-1195.

36. Pulido, A.; Nachtigall, P.; Zukal, A.; Domínguez, I.; Čejka, J., Adsorption of CO_2 on Sodium-Exchanged Ferrierites: The Bridged CO_2 Complexes Formed between Two Extraframework Cations. *The Journal of Physical Chemistry C* **2009,** *113* (7), 2928-2935.

CHAPTER 2. THE EFFECT OF ALUMINUM SHORT-RANGE ORDERING ON CARBON DIOXIDE ADSORPTION IN ZEOLITES

2.1 Introduction and Literature Review[⊥]

Zeolites are tetrahedral aluminosilicates that are widely used as catalysts in petrochemical reactions and as gas adsorbents. There are more than 200 distinct zeolite topologies that have been synthesized[1]. Cationic zeolites (that is, materials with a finite Si/Al ratio) are particularly important in catalysis. The locations of the extra-framework cations in these materials can be influenced by the distribution of framework aluminum[2-6]. Acid strength has been linked to the differences in the aluminum distribution for a given zeolite topology[7]. As a result, understanding the aluminum distribution in zeolites is important. A widely accepted rule of thumb related to aluminum distribution is Lowenstein's rule, which states that occupancy of neighboring T sites by Al atoms is prohibited. Dempsey et al. proposed a rule to complement Lowenstein's rule, stating that aluminum is distributed in a manner which minimizes the number of next nearest neighbors[8]. Although this was true for the faujisite (FAU) systems studied by Dempsey et al., the rule is not generally valid for all zeolites. Examples include the dealuminated

[⊥] Material in this chapter has been published previously as Findley, J. M.; Ravikovitch, P. I.; Sholl, D. S., The effect of aluminum short-range ordering on carbon dioxide adsorption in zeolites. *The Journal of Physical Chemistry C* **2018,** *122* (23), 12332-12340

faujisites studied by Herrero[9], and the MOR and FER zeolites studied by Kato and coworkers[10].

Sastre and coworkers noticed that the structure directing agent (SDA) used in zeolite synthesis can play a role in directing the aluminum distribution[11]. Since then, strides have been made in controlling the aluminum distribution in zeolites. Dwyer et al. showed that FAU synthesized in the presence of crown ethers had a different aluminum distribution than FAU that was dealuminated using sulfur hexafluoride[12]. The size of the SDA has also been shown to affect the aluminum distribution in FER and MFI-type zeolites[13, 14]. DiIorio and Gounder recently developed a method to isolate framework aluminum atoms in chabazite (CHA) zeolites by controlling the ratio of Na^+ to $TMAda^+$ present during synthesis[15].

Although the locations of extra-framework cations can be studied using diffraction techniques, it is difficult to distinguish Al and Si using these methods[16]. Aluminum locations are typically determined by using ^{27}Al magic-angle spinning (MAS) NMR or by ^{29}Si MAS NMR[14, 16]. It is challenging, however, to use these methods to explore the combined effects of zeolite topology, Si/Al ratio and structure directing agent on aluminum distribution. Titration with divalent cations has also been used to determine the fraction of isolated framework Al atoms[15, 16]. However, this method does not completely define the aluminum distribution on the framework and it yields limited information at low Si/Al ratios.

Molecular simulations provide a well-defined way to examine topological and compositional effects of zeolites on measurable quantities such as adsorption isotherms[6].

Liu et al. examined the effects of aluminum distribution on adsorption isotherms and Henry's constants for alkanes in several zeolites. That work suggested that one could potentially determine the aluminum distribution based on a comparison of adsorption isotherms with experiment. However, it was found that the isotherms that were examined were not sensitive to aluminum ordering in LTA or FAU[6].

In this chapter, we use molecular simulations to investigate the use of CO_2 adsorption isotherms as a method for probing the aluminum distribution in zeolites. It is known that extra-framework cations prefer to be located near framework aluminum atoms due to the more negative charges on the adjacent framework oxygen atoms[2, 3, 5, 6]. Therefore, CO_2 is therefore a potentially useful probe molecule because its quadrupolar nature makes it sensitive to local electric fields[17]. CO_2 has been shown to prefer to adsorb at sites in which it acts as a bridge between two extra-framework cations in Na-FER, K-FER, NaA, NaY and Na-ZSM-5[2, 3, 5, 18]. The availability of these sites may therefore result in changes in adsorption isotherms when the distribution of framework Al is varied. Our calculations use a high quality force field for interactions of CO_2 with cationic zeolites and the methods to efficiently sample the location of extra-framework cations in zeolites introduced by Fang et al.[4]. This makes it possible to use the methods we introduce here to quantitatively assess the degree of aluminum ordering in zeolites when experimental CO_2 adsorption isotherms are available.

2.2 Materials and Methods

2.2.1 Adsorbate and Framework Models

The TraPPE force field was used to describe CO_2 – CO_2 interactions because of its ability to accurately describe bulk CO_2 properties such as saturation pressure[19]. The CO_2, Na and K interaction potentials with the zeolite framework. were taken from the CCFF force field from Fang et al.[4]. The CCFF force field was developed from extensive quantum chemistry calculations[20] and shows close agreement with experiments for zeolites NaX, NaY, 4A[4] and CHA[21]. The atomic coordinates for all zeolite structures were taken from the IZA database[1] unless otherwise indicated.

2.2.2 Generation of Aluminum Distribution by Reverse Monte Carlo

To enable our calculations, we must be able to create zeolite structures with a variety of well-defined Al distributions. Throughout our calculations, we characterized the distribution of framework Al using the Warren-Cowley parameter[22-24]

$$\alpha_j = 1 - \frac{P_j^{Al(Si)}}{x_{Si}} \tag{2.1}$$

Here, $P_j^{Al(Si)}$ is the probability of finding Si as the *j*-th nearest neighbor of Al and x_{Si} is the mole fraction of Si in the framework. We assume that Lowenstein's rule prohibiting Al-O-Al linkages is valid, so $j = 2$ describes the closest possible location of two framework Al. We describe materials solely in terms of their Warren-Cowley parameter with $j = 2$, although in principle more detailed descriptions could be made by also using information from larger values of *j*. We denote the Warren-Cowley parameter as α below. If Al atoms

are randomly distributed among framework atoms, $\alpha = 0$. Values of α that are close to 1 describe a clustered distribution of aluminum, while more negative values of α describe a sparser distribution of aluminum.

Starting with a pure silica frameworks from the IZA database[1], unit cells were expanded until they contained 100 or more T-atoms to allow for more variability in aluminum distribution. An initial distribution of aluminum was generated by randomly substituting Al in place of Si under the constraints of Lowenstein's rule until the desired Si/Al ratio was reached. Subsequently, a Reverse Monte Carlo (RMC) algorithm[22] was used to obtain the desired distribution of aluminum by swapping framework Al and Si under the constraints of Lowenstein's rule.

We will use the terms sparse, random, and clustered to describe three different distributions of aluminum that were compared for a given topology (LTA, FAU, CHA, KFI, RHO, FER and MOR) and Si/Al ratio (Si/Al = 11, 5, 2) using Na^+ or K^+ as extra-framework cations. The sparse distribution is defined by the minimum Warren-Cowley parameter that could be obtained in 10^5 attempted Si/Al swaps in our RMC simulation when the target is $\alpha = -1$. The value of this parameter is bounded by –Al/Si, which corresponds to the presence of zero Al-O-Si-O-Al linkages. The random distribution describes the average Warren-Cowley parameter obtained for 100 random distributions of aluminum that were only subject to Lowenstein's rule. Our assumption that Lowenstein's rule holds means that this situation does not correspond exactly to $\alpha = 0$, especially for low Si/Al ratios. Once the target Warren-Cowley parameter for this situation was known, aluminum distributions were generated using RMC using this parameter as the goal. The

clustered distribution is described by the maximum Warren-Cowley parameter that could be obtained in 10^5 attempted Si/Al swaps when the target is $\alpha = 1$.

2.2.3 Initialization of Cation Configurations

It has been shown that adsorption isotherms in cationic zeolites are sensitive to the positions of the extra-framework cations in some zeolites[4, 6, 17, 25]. It is therefore important that cation positions in structures for simulating adsorption isotherms are carefully equilibrated. Following the work of Fang et al., extra-framework cation positions were equilibrated using parallel tempering[21]. These simulations were performed using the open-source RASPA package[26]. As in Fang et al.[21], 9 structural replicas were used at T = 300 K, 390 K, 507 K, 659 K, 857 K, 1114 K, 1448 K, 1882 K and 2447 K using the temperature spacing suggested by Beauvais et al.[27]. The force field used was the CCFF force field derived in Fang et al.[4, 5]. Electrostatic energies were calculated using the Ewald summation with a relative error of 10^{-6} and dispersion potentials had a cutoff of 12.0 Å. In these and all of our molecular simulations, the positions of all framework atoms were assumed to be rigid. Parallel tempering and the following GCMC simulations were performed in triplicate for three distinct initial configurations of extra-framework cations in each material studied.

2.2.4 Grand Canonical Monte Carlo Simulation Details

Single component CO_2 adsorption isotherms were simulated at 300 K using RASPA[26]. Simulations were performed using a rigid framework, although translation moves were allowed for extra-framework cations. Sodalite cages in LTA and FAU, which are inaccessible to CO_2, were blocked[28, 29]. Electrostatic energies were calculated using Ewald summation with a precision of 10^{-6}, and dispersion interactions were calculated

using a 12.0 Å cutoff using periodic boundary conditions. If the lattice parameter was smaller than 24.0 Å in any direction, then the unit cell was expanded along that direction until it was large enough to satisfy the minimum image convention. Sampling was started after the completion of 5×10^4 initialization cycles. Thermodynamic properties were sampled over 10^5 cycles. Initial tests indicated that this amount of sampling gave well converged results. The standard deviation in calculated loadings, computed using block averages, was typically less than 1% of the loadings.

2.3 Results and Discussion

2.3.1 Sensitivity of CO_2 Adsorption Isotherms to Aluminum Distribution

The effect of Al distribution on CO_2 adsorption isotherms in Na-LTA with Si/Al=2, Na-CHA with Si/Al=11 and Na-FER with Si/Al=8.7 is shown in Figure 2.1. In all cases, experimental CO_2 isotherms are available for comparison.

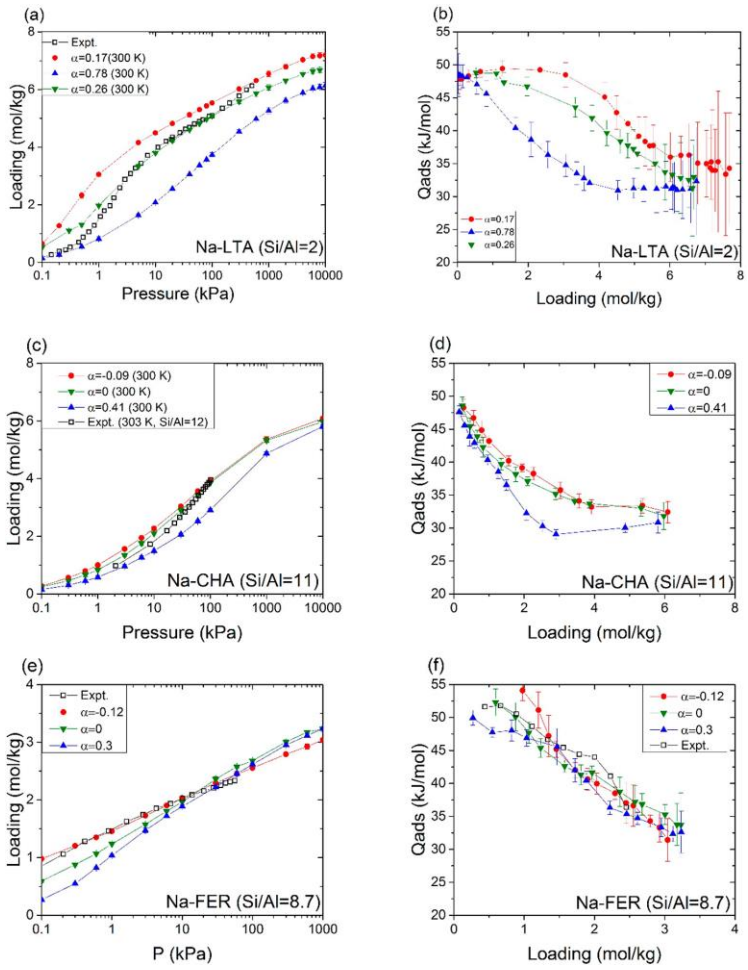

Figure 2.1 - CO_2 adsorption isotherms (a,c,e) and heats of adsorption (b,d,f) at T=300 K are shown for Na-LTA with Si/Al=2 (a,b), Na-CHA with Si/Al=11 (c,d), and Na-FER with Si/Al = 8.7 (e,f). Simulated adsorption isotherms for sparse aluminum structures are shown in red, random are shown in green and clustered aluminum are shown in blue. The Warren-Cowley parameters are listed in the legend. Experimental data is taken from Palomino et al. for LTA[30] , Pham et al. for CHA[31] and Pulido et al. for FER[2].

Figure 2.1(a) shows that there are considerable differences between the CO_2 isotherms for the sparse (red), random (green), and clustered (blue) Al distributions in Na-LTA (Si/Al=2). For these simulations of LTA (Si/Al=2), the 4A coordinates from Pluth and Smith were used in order to account for slight differences in the framework caused by the high aluminum content[32]. At 100 kPa, for example, the predicted isotherms vary by almost a factor of two between the sparse and clustered materials. The origins of these

effects are straightforward to understand in terms of the heat of adsorption for CO_2 in each material, as shown in Figure 2.1(b). For moderate CO_2 loadings (2-4 mol/kg), the heats of adsorption (Q_{ads}) in the sparse and clustered structures differ by 15-20 kJ/mol, leading to large differences in the adsorbed loading. It is well known that the existence of so-called dual and single cation sites can significantly enhance the heat of adsorption of CO_2[2, 3, 5]. Dual cation sites, which have higher heats of adsorption, are present for all three Al-distributions, as shown by the low loading Q_{ads}, which does not vary with Al-distribution. However, the higher heats of adsorption at moderate CO_2 in the sparse material are the result of a larger density of dual and single cation sites.

Figure 2.1(c) shows simulated and experimental CO_2 adsorption isotherms for Na-CHA with Si/Al=11. In this example, the difference between the CO_2 adsorption isotherm for sparse (red) and random (green) Al distributions is almost negligible (less than 0.3 mol/kg at all pressures). However, the isotherm for the clustered (blue) distribution was shows significantly less adsorption than the other two isotherms. These differences can again be explained by examining the heat of adsorption in Figure 2.1(d), where the heat of adsorption for the clustered (blue) Al distribution was 3-8 kJ/mol lower than the heats of adsorption than the heats of adsorption for the sparse (red) and random (green) Al distributions for moderate CO_2 loadings (2-4 mol/kg). When compared to the adsorption isotherms for Na-LTA with Si/Al=2, the isotherms for Na-CHA with Si/Al = 11 are much less sensitive to the Al distribution, especially in the case of the sparse (red) distribution. This observation hints that the zeolite topology and Si/Al ratio both play a role in the sensitivity of CO_2 adsorption isotherms to Al distribution.

For both Na-LTA with Si/Al = 2 and Na-CHA with Si/Al = 11, the CO_2 adsorption isotherm for the random Al distribution is in better agreement with experimental results than the isotherms from sparse or clustered Al distributions. CO_2 adsorption isotherms for a random Al distribution Na-FAU (Si/Al=5.1), which can be found in Appendix A.5, also provide the best agreement with experimental results. More potential orderings in Na-LTA (Si/Al = 2) were investigated in the Appendix A.5. Because the CCFF approach used in our molecular simulations is expected to have a high level of accuracy[4, 21], it is therefore reasonable to use our calculations as evidence that the experimental Al distribution in these two materials is approximately random. It is important to note, however, that other zeolite topologies, such as Na-FER (Si/Al=8.7), are known to have nonrandom distributions of framework Al. In the work by Dedecek et al. on Na-FER (Si/Al = 8.6)[16], no two Al atoms were second nearest neighbors to one another. Based on our definition of the Warren-Cowley parameter, this would correspond to a value of $\alpha = -0.12$. Figure 2.1(e) and Figure 2.1(f) show simulated and experimental CO_2 adsorption isotherms for Na-FER (Si/Al = 8.7). The simulated isotherm corresponding to $\alpha = -0.12$ gave the best agreement with experimental results, consistent with Dedecek et al.'s analysis of the Al distribution.

2.3.2 The Effect of Aluminum Distribution on Cation Distribution

It is well known that the distribution of framework Al in zeolites can affect the position of extra-framework cations[6, 15, 33]. In the previous section, differences in CO_2 adsorption isotherms for different distributions of Al were stated to be a result of differences in the number of dual-cation sites available. Figure 2.1 also showed that the adsorption isotherms for the sparse distribution of Al had the largest loadings at low and intermediate pressures. To explain this, it is useful to describe the distribution of extra-

framework cations for each distribution of Al. Figure 2.2 shows the site occupancies for 8-membered window sites and Na-Na radial distribution function (RDF) to describe the distribution of extra-framework Na^+ in Na-LTA (Si/Al=2) and Na-CHA(Si/Al=11). For these topologies and compositions, each Na^+ cation was observed to sit in either an 8-membered window or a 6-membered window. As expected, the Al distribution affects the location of extra-framework cations for these two topologies and compositions.

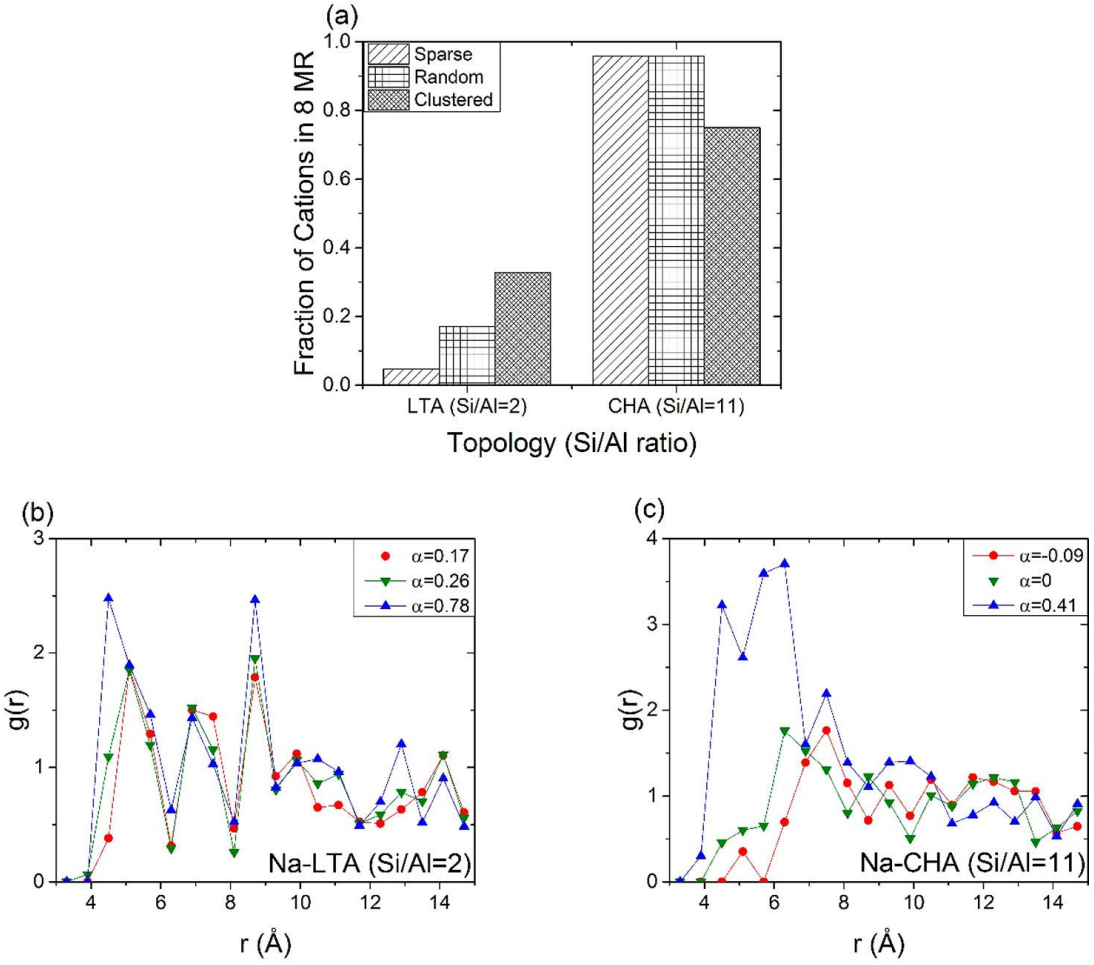

Figure 2.2 - The cation distributions for Na-LTA (Si/Al=2) and Na-CHA (Si/Al=11) are described by the fraction of Na^+ occupying 8-membered ring sites (a) and the Na-Na radial distribution function in Na-LTA (Si/Al = 2) (b) and Na-CHA (Si/Al = 11) (c).

The first peaks (r = 4-6 Å) in Figure 2.2(b) and (c) show that the clustering of Al leads to clustering of extra-framework cations and a sparse distribution of Al results in a sparser cation distribution, as might be expected. This effect is more visible in Figure 2.2 (c) because of the lower density of cations in the framework with Si/Al=11 than when Si/Al=2. The first set of Na-Na distances in these RDFs (r = 4-6 Å) are shorter than any known or predicted dual-cation sites, which typically have cation-cation distances between 6 and 8 Å[2, 5, 18]. That is, the pairs associated with the first peak in the RDF are too short to be bridged by a CO_2 molecule. The presence of these cation pairs therefore results in a lower number of dual-cation sites in frameworks with a more clustered distribution of aluminum. This is consistent with the Q_{ads} trends in Figure 2.1, where there was a higher density of favorable sites in frameworks with a sparser distribution of Al, even when the Na-Na radial distribution function shows a similar number of Na-Na distances between 6 Å and 8 Å.

Figure 2.2(a) and (b) show how changing the Al distribution affects the locations of Na^+ in Na-LTA (Si/Al=2). The first peak in the Na-Na RDF corresponds to distances between two adjacent 6-membered rings on the sodalite cage as well as Na^+ in a 6-membered ring near another Na^+ in the nearest corner of an 8-membered ring. CO_2 was not observed to bridge either of these cation pairs in our GCMC simulations. This peak is less significant, although still present, for the sparse and random Al distributions in LTA (Si/Al=2). Figure 2.2(a) shows that sparser Al distributions place more Na^+ into the 6-membered ring sites. This is favorable for CO_2 adsorption because the 6-membered ring Na^+ sites in in the LTA cage are spaced 7 Å apart, which should allow for the formation of dual-cation sites. This feature of LTA cages could cause LTA-type topologies to exhibit

sensitivity to CO_2 adsorption at even lower Si/Al ratios. When compared to Na-LTA (Si/Al=2), Na-CHA (Si/Al=11) exhibits much lower sensitivity to a sparse aluminum distribution (see Figure 2.2(a) and (c)). Both the sparse and random Al distribution in Na-CHA (Si/Al=11) yield the same population of 8-membered ring Na^+ and comparable Na-Na RDFs at distances of 4-6 and 6-8 Å.

2.3.3 Isotherm Sensitivity Across Si/Al Ratio and Topology

Having discussed several specific examples, it is useful to introduce an approach that can allow the sensitivity of CO_2 adsorption to Al distribution to be compared for a larger number of materials. To this end, we define an isotherm's sensitivity using a range of evenly spaced data in log(pressure):

$$\frac{1}{5}\sum_{i=1}^{i=5}\left|Loading\left(ordered, P = 10^{i+2}\right) - Loading\left(random, P = 10^{i+2}\right)\right| \qquad (2.2)$$

where P is the pressure in Pa and ordered can mean either sparse or clustered Al. With this definition, a sensitivity of 0.5 mmol/g implies that the difference in the adsorbed amount of CO_2 between the ordered and random systems is 0.5 mmol/g (on average) at all pressures. The results are shown as a function of Si/Al ratio for seven zeolite topologies in Figure 2.3.

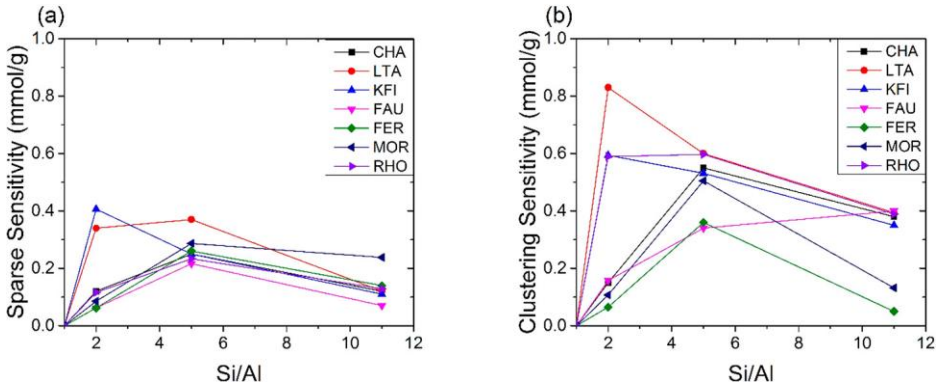

Figure 2.3 - The sensitivity of adsorption isotherms for seven Na-exchanged zeolites to a sparse distribution of aluminum (a) and a clustered distribution of aluminum (b) are shown as a function of Si/Al ratio.

The sensitivity of CO_2 adsorption to Al distribution is strongly influenced by the Si/Al ratio. At Si/Al=1, the sensitivity is zero by definition because Lowenstein's rule only allows for an alternating distribution of Al and Si. For pure silica materials (Si/Al = ∞), the sensitivity will also be zero by definition. This means that for any given topology there is an intermediate Si/Al ratio that maximizes the sensitivity. As shown in Figure 2.3, the maximum sensitivity for both clustered and sparse Al distributions typically occurs close to Si/Al = 5, with a sparse sensitivity of 0.2-0.4 mmol/g and a clustering sensitivity of 0.3-0.6 mmol/g..

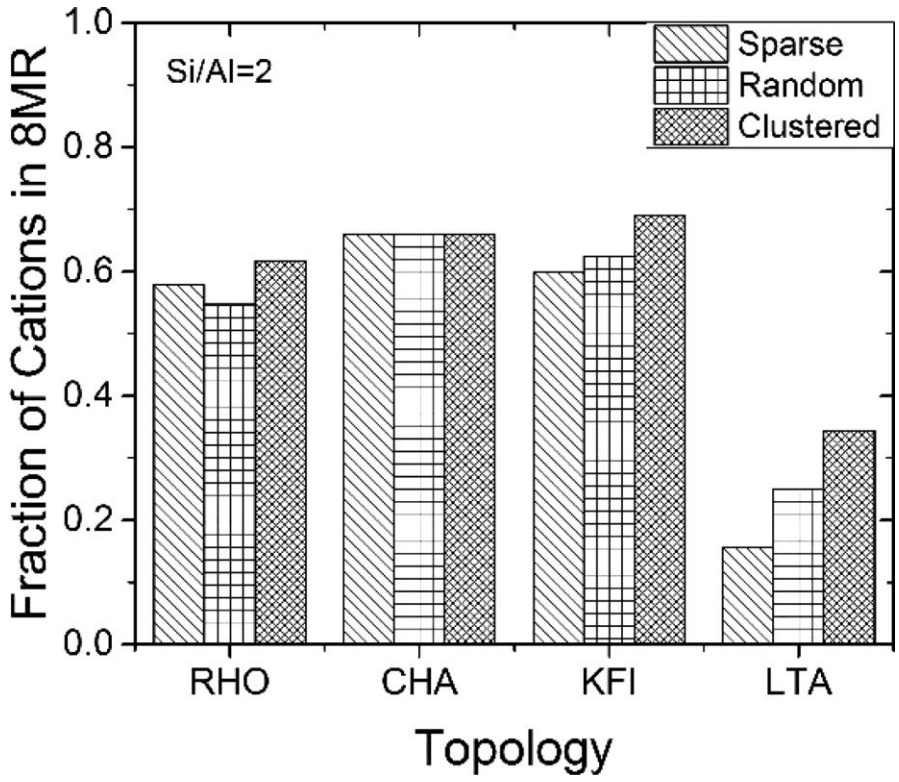

Figure 2.4 - The fraction of cations in 8-membered ring sites is shown for different Al distributions in Na-LTA,RHO,CHA and KFI at Si/Al=2. There is more variability in the cation distribution for LTA and KFI, which also have more sensitive isotherms at this Si/Al ratio.

The CO_2 sensitivity is typically the highest at Si/Al ~ 5 because this allows a large number of dual-cation sites while also having enough unfilled cation positions to allow for multiple ways to distribute cations in the framework. At both Si/Al=2 and Si/Al=5, there are many dual-cation sites present for each topology we considered. As the Si/Al ratio decreases from 5 to 2, however, more of the cation locations are occupied, which places additional constraints upon the cation distribution. Figure 2.4 demonstrates the effect of this site-filling that occurs at higher Al content. LTA and KFI have higher variability in the number of cations in the 8-membered rings than RHO and CHA, resulting in a higher sensitivity to Al distribution even at Si/Al=2. Na-CHA (Si/Al=2) is insensitive to Al

distribution, because there is almost no variability in the distribution of Na^+. At the same Si/Al ratio, Na-KFI and Na-LTA both have large variability in the Na^+ distribution and adsorption is therefore sensitive to the Al distribution.

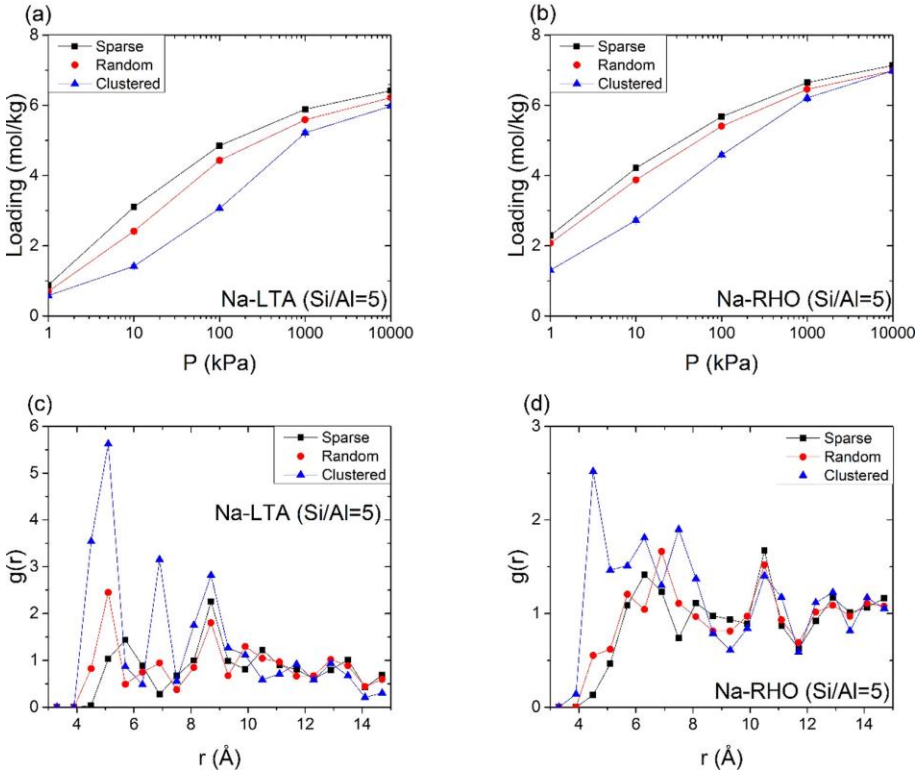

Figure 2.5 - The adsorption isotherms for Na-LTA (Si/Al=5) (a) and Na-RHO (Si/Al=5) (b) and the Na-Na RDFs for Na-LTA (Si/Al=5) (c) and Na-RHO (Si/Al=5) (d) are shown for three different distributions of aluminum. Despite having a similar cage type, LTA and RHO have different sensitivity due to constraints in the cation distribution caused by the double 8-membered ring Na sites in Na-RHO.

This site-filling can also be observed when comparing the sparse sensitivity of Na-LTA (Si/Al=5) and Na-RHO (Si/Al=5). The only differences between these two topologies are that double 8-membered rings connect the LTA cages in RHO and that RHO does not have a sodalite cage[34]. However, the sparse sensitivity of CO_2 adsorption in LTA (Si/Al=5) is nearly double that of RHO (Si/Al=5) (see Figure 2.3(a)). Figure 2.5 shows the adsorption isotherms and Na-Na RDFs for Na-LTA and Na-RHO. Despite the similarity in topology,

the differences in Na-Na RDF for sparse and clustered aluminum are much more noticeable for LTA. This can be attributed to the strong electrostatic repulsion that discourages two Na^+ from sitting in the same double 8-membered window, as these two sites can be approximately 4 Å apart. In experiments, Na^+ has not been observed in adjacent 8-membered rings in Na-RHO (Si/Al=3.9)[35]. Our simulated Na^+ distributions are in agreement with this experimental observation when the Al distribution is sparse or random at Si/Al=5. Our clustered distribution, however, is in disagreement with this experimental observation, as shown by the large first peak in Figure 2.5(d). Due to the strong electrostatic repulsion when placing two Na^+ at opposite sides of the same double 8-membered window, effectively half of the 8-membered ring sites in RHO are available for Na^+ siting, provided there is limited Al clustering. This can be observed by examining the sharp first peak in the Na-Na RDF for RHO with Si/Al=5. This additional constraint on the distribution of Na^+ in RHO results in a smaller difference in the Na^+ distribution in RHO (Si/Al=5), leading to reduced sensitivity to a sparse aluminum distribution.

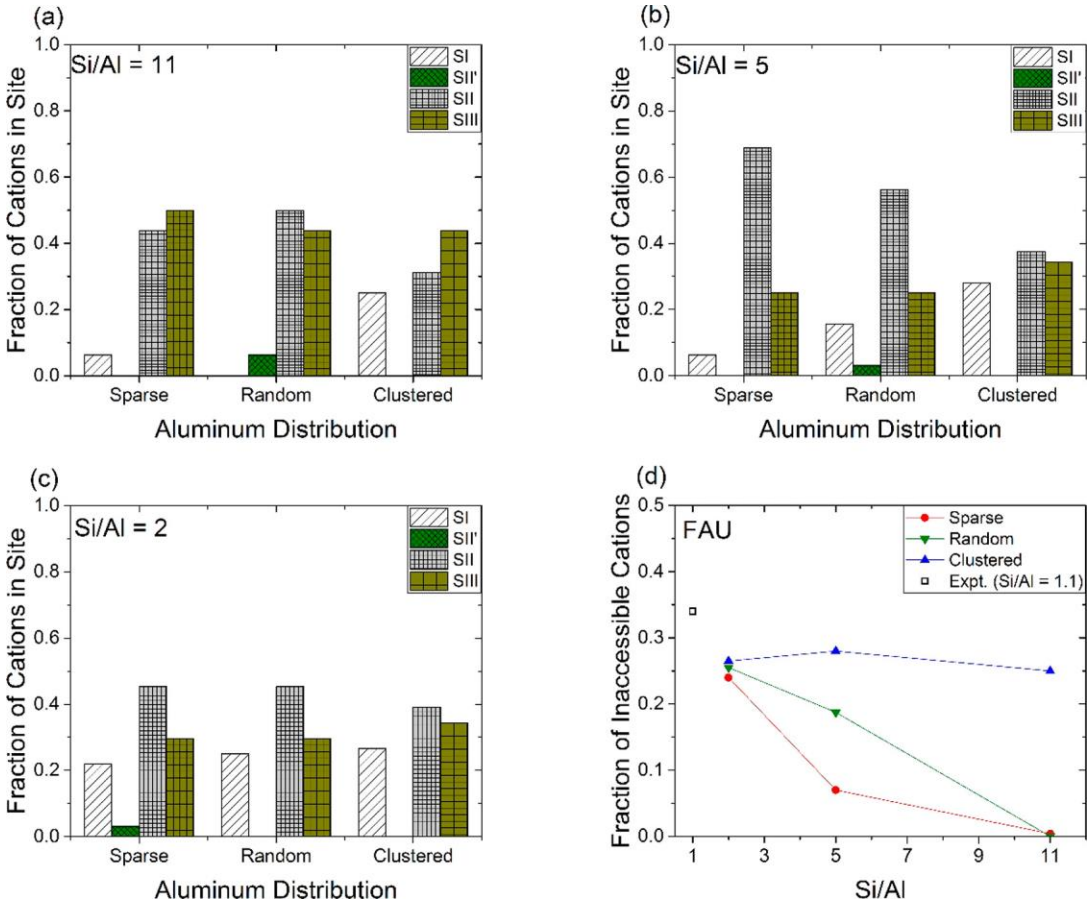

Figure 2.6 - The fraction of Na^+ in each type of extra-framework site in Na-FAU is shown for Si/Al=11 (a), Si/Al=5 (b), and Si/Al=2(c). The total fraction of Na^+ that is inaccessible to CO_2 adsorption (d) is also shown as a function of Si/Al ratio.

Although most of the zeolites we examined had the highest sensitivity at Si/Al=5, FAU exhibited a monotonic decrease in sensitivity to Al clustering from Si/Al=11 to Si/Al=2. The FAU unit cell contains sodalite cages and hexagonal prisms that are inaccessible to CO_2 adsorption[36]. It has been shown that Na^+ can be located in each of these units[37]. Figure 2.6 shows the distribution of Na^+ in the sites that were identified in Jaramillo et al. [38] at Si/Al=11, 5 and 2. For the purposes of our analysis, SI and SI′ are grouped together because they are both at the 6-membered ring between the sodalite cage and the hexagonal prism, which are both inaccessible to CO_2. Site SII′ is also located inside of the

sodalite cage and therefore inaccessible to CO_2 adsorption. Figure 2.6 shows that Al clustering results in a larger population of type SI cations, which indicates that the clustering of Al occurs on sodalite cages and hexagonal prisms. As the Si/Al ratio is decreased from 11 to 5, more Na^+ are placed in the inaccessible sites SI and SII′ when Al is randomly distributed. This is a result of doubling the number of Al that are second nearest neighbors when decreasing the Si/Al from 11 to 5. Second-nearest neighboring aluminum are more likely to be located on the same sodalite cage or hexagonal prism, resulting in a higher probability that Na^+ will occupy these sites. When going from Si/Al=5 to Si/Al=2, even more cations are placed in inaccessible locations for all three distributions of aluminum. This results in a low sparse and clustering sensitivity at Si/Al=2. Figure 2.6(d) shows the total fraction of Na^+ in inaccessible locations as a function of Si/Al ratio. The differences in cation accessibility between the sparse or clustered Al and random Al distributions are in qualitative agreement with the sensitivity trends in sensitivity shown in Figure 2.3. The experimentally determined fraction of inaccessible cations obtained by Zhu et al.[37] for Si/Al = 1.1 is shown for comparison in Figure 2.6(d). The experimentally observed fraction of inaccessible cations is close to that of the clustered Al distribution because both Si/Al = 1.1 and clustered Al distributions have significant regions of alternating Si and Al due to Lowenstein's rule.

2.3.4 Comparison of Na^+ and K^+ Zeolites

It is interesting to extend our results from above by comparing the sensitivities of Na-exchanged and K-exchanged zeolites. Figure 2.7 shows a comparison of the sensitivities, calculated in the same manner as in Figure 2.3, of Na-exchanged LTA and CHA and K-exchanged LTA and CHA. Generally, the sensitivity of the Na-exchanged zeolite was higher than the K-exchanged zeolite. It is well-documented that K^+ prefers to be located close to the center of 8-membered rings[39]. This preference reduces the influence of Al distribution on the cation distribution when compared to Na-zeolites, in which Na^+ does not have a strong preference between 8-membered and 6-membered ring sites. The differences in sensitivity are the higher for the LTA topology than the CHA topology because CHA has a higher number of 8-membered ring sites (on a per atom basis) than LTA. For example, Figure 2.2(a) shows that at Si/Al=11, most of the Na^+ is already located in 8-membered rings for all distributions of aluminum. Therefore, there is little effect of cation type on isotherm sensitivity for CHA at Si/Al=11 for sparse or clustered Al distributions. In LTA, there are fewer 8-membered windows than in CHA. Therefore, the preference of K^+ for the 8-membered ring centers leads to a larger influence of cation type on adsorption sensitivity.

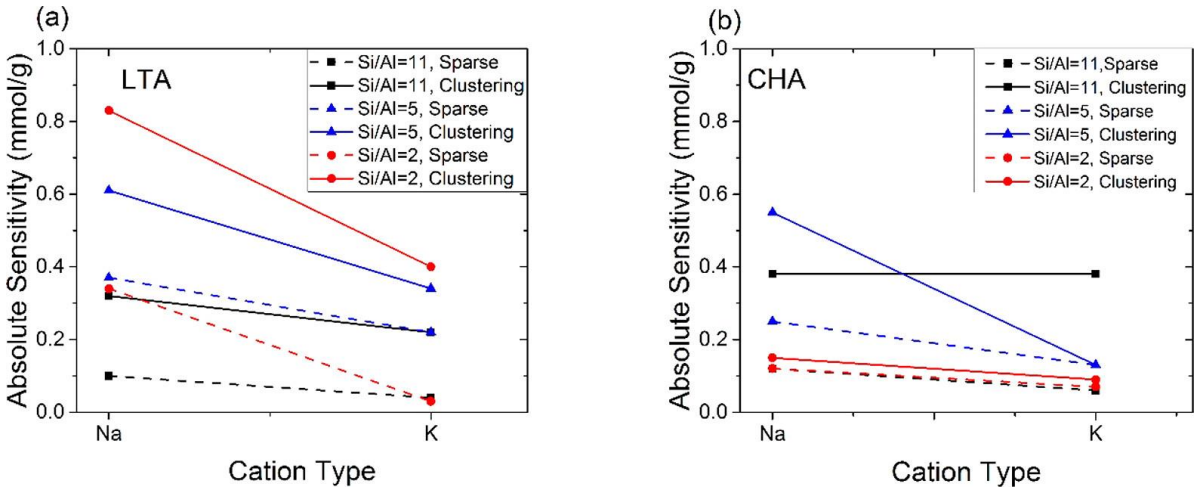

Figure 2.7 - The sensitivities of CO_2 adsorption isotherms for LTA (a) and CHA (b) exchanged with Na^+ and K^+ are compared based on the type of extra-framework cation for Si/Al=11 (black), Si/Al=5 (blue) and Si/Al=2 (red). Sparse sensitivities are shown by dashed lines and clustering sensitivities are connected by solid lines.

2.4 Conclusions

Characterization of the aluminum distribution in cationic zeolites is important to understanding the catalytic and adsorptive properties of these materials. We have used simulated CO_2 adsorption isotherms using high quality force fields to examine the impact of aluminum distribution in a range of zeolites. Comparison with experimental data showed that simulations of this kind can distinguish between various degrees of aluminum ordering. For example, prior experiments with Na-LTA (Si/Al=2) and Na-CHA (Si/Al=11) were shown to be consistent with random ordering of Al, while experiments with Na-FER (Si/Al = 8.6) were found to be consistent with non-random Al orderings.

We used simulated CO_2 adsorption isotherms to assess the sensitivity of these isotherms to Al ordering in seven industrially relevant zeolites. In general terms, the CO_2 isotherms are most sensitive to Al ordering for Si/Al ratios around 5, and the isotherms in Na-exchanged zeolites are more sensitive than in K-exchanged zeolites. The differences

that can exist between CO_2 isotherms in materials with different Al ordering but otherwise identical composition stem from differences in the number of favorable CO_2 adsorption sites. These sites, in turn, are related to the distribution of cation-cation distances in the material. Clustering of aluminum in general results in cation-cation distances that are too small to enable favorable CO_2 adsorption. This effect means that the amount of adsorbed CO_2 at a given external pressure is typically smaller in materials with clustered aluminum than in materials with more random or sparse orderings.

Our results indicate that high quality measurements of CO_2 adsorption can be combined with molecular simulations to deduce the degree of Al ordering in materials for which this ordering is previously unknown. Given the challenges associated with directly measuring Al ordering in zeolites with other experimental methods, the ability to achieve this goal with relatively accessible experimental data may create opportunities to study the connections between zeolite synthesis and treatment conditions and aluminum ordering in a far wider range of materials than has been previously contemplated.

2.5 Chapter 2 References

1. Baerlocher, C.; McCusker, L. B.; Olson, D. H., *Atlas of zeolite framework types*. Elsevier: 2007.

2. Pulido, A.; Nachtigall, P.; Zukal, A.; Domínguez, I.; Čejka, J., Adsorption of CO_2 on Sodium-Exchanged Ferrierites: The Bridged CO_2 Complexes Formed between Two Extraframework Cations. *The Journal of Physical Chemistry C* **2009,** *113* (7), 2928-2935.

3. Zukal, A.; Pulido, A.; Gil, B.; Nachtigall, P.; Bludsky, O.; Rubes, M.; Cejka, J., Experimental and theoretical determination of adsorption heats of CO_2 over alkali metal exchanged ferrierites with different Si/Al ratio. *Phys Chem Chem Phys* **2010,** *12* (24), 6413-22.

4. Fang, H.; Kamakoti, P.; Ravikovitch, P. I.; Aronson, M.; Paur, C.; Sholl, D. S., First principles derived, transferable force fields for CO_2 adsorption in Na-exchanged cationic zeolites. *Phys Chem Chem Phys* **2013,** *15* (31), 12882-94.

5. Fang, H.; Kamakoti, P.; Zang, J.; Cundy, S.; Paur, C.; Ravikovitch, P. I.; Sholl, D. S., Prediction of CO_2 Adsorption Properties in Zeolites Using Force Fields Derived from Periodic Dispersion-Corrected DFT Calculations. *The Journal of Physical Chemistry C* **2012,** *116* (19), 10692-10701.

6. Liu, B.; García-Pérez, E.; Dubbeldam, D.; Smit, B.; Calero, S., Understanding Aluminum Location and Non-framework Ions Effects on Alkane Adsorption in Aluminosilicates: A Molecular Simulation Study. *The Journal of Physical Chemistry C* **2007,** *111* (28), 10419-10426.

7. Beagley, B.; Dwyer, J.; Fitch, F. R.; Mann, R.; Walters, J., Aluminum distribution and properties of faujasites. Basis of models and zeolite acidity. *The Journal of Physical Chemistry* **1984,** *88* (9), 1744-1751.

8. Dempsey, E.; Kuehl, G. H.; Olson, D. H., Variation of the lattice parameter with aluminum content in synthetic sodium faujasites. Evidence for ordering of the framework ions. *The Journal of Physical Chemistry* **1969,** *73* (2), 387-390.

9. Herrero, C. P., Short-range order of the silicon, aluminum distribution on the faujasite framework. *The Journal of Physical Chemistry* **1991,** *95* (8), 3282-3288.

10. Kato, M.; Itabashi, K.; Matsumoto, A.; Tsutsumi, K., Characteristics of MOR-Framework Zeolites Synthesized in Fluoride-Containing Media and Related Ordered Distribution of Al Atoms in the Framework. *The Journal of Physical Chemistry B* **2003,** *107* (8), 1788-1797.

11. Sastre, G.; Fornes, V.; Corma, A., On the Preferential Location of Al and Proton Siting in Zeolites: A Computational and Infrared Study. *The Journal of Physical Chemistry B* **2002,** *106* (3), 701-708.

12. Dwyer, J.; Karim, K.; Smith, W. J.; Thompson, N. E.; Harris, R. K.; Apperley, D. C., A comparison of siliceous faujasitic zeolites produced by direct synthesis or by secondary synthesis. *The Journal of Physical Chemistry* **1991,** *95* (22), 8826-8831.

13. Gábová, V.; Dědeček, J.; Čejka, J., Control of Al distribution in ZSM-5 by conditions of zeolite synthesis. *Chemical Communications* **2003,** (10), 1196-1197.

14. Pinar, A. B.; Gómez-Hortigüela, L.; McCusker, L. B.; Pérez-Pariente, J., Controlling the Aluminum Distribution in the Zeolite Ferrierite via the Organic Structure Directing Agent. *Chemistry of Materials* **2013,** *25* (18), 3654-3661.

15. Di Iorio, J. R.; Gounder, R., Controlling the Isolation and Pairing of Aluminum in Chabazite Zeolites Using Mixtures of Organic and Inorganic Structure-Directing Agents. *Chemistry of Materials* **2016,** *28* (7), 2236-2247.

16. Dedecek, J.; Lucero, M. J.; Li, C.; Gao, F.; Klein, P.; Urbanova, M.; Tvaruzkova, Z.; Sazama, P.; Sklenak, S., Complex Analysis of the Aluminum Siting in the Framework of Silicon-Rich Zeolites. A Case Study on Ferrierites. *The Journal of Physical Chemistry C* **2011,** *115* (22), 11056-11064.

17. Bonenfant, D.; Kharoune, M.; Niquette, P.; Mimeault, M.; Hausler, R., Advances in principal factors influencing carbon dioxide adsorption on zeolites. *Science and Technology of Advanced Materials* **2008,** *9* (1), 013007.

18. Nachtigall, P.; Delgado, M. R.; Nachtigallova, D.; Arean, C. O., The nature of cationic adsorption sites in alkaline zeolites--single, dual and multiple cation sites. *Phys Chem Chem Phys* **2012,** *14* (5), 1552-69.

19. Potoff Jeffrey, J.; Siepmann, J. I., Vapor–liquid equilibria of mixtures containing alkanes, carbon dioxide, and nitrogen. *AIChE Journal* **2004,** *47* (7), 1676-1682.

20. Fang, H.; Demir, H.; Kamakoti, P.; Sholl, D. S., Recent developments in first-principles force fields for molecules in nanoporous materials. *Journal of Materials Chemistry A* **2014,** *2* (2), 274-291.

21. Fang, H.; Kulkarni, A.; Kamakoti, P.; Awati, R.; Ravikovitch, P. I.; Sholl, D. S., Identification of High-CO_2-Capacity Cationic Zeolites by Accurate Computational Screening. *Chemistry of Materials* **2016,** *28* (11), 3887-3896.

22. Kamakoti, P.; Sholl, D. S., Ab initiolattice-gas modeling of interstitial hydrogen diffusion in CuPd alloys. *Physical Review B* **2005,** *71* (1).

23. Cowley, J. M., Short- and Long-Range Order Parameters in Disordered Solid Solutions. *Physical Review* **1960,** *120* (5), 1648-1657.

24. Jayachandrababu, K. C.; Verploegh, R. J.; Leisen, J.; Nieuwendaal, R. C.; Sholl, D. S.; Nair, S., Structure Elucidation of Mixed-Linker Zeolitic Imidazolate Frameworks by Solid-State 1H CRAMPS NMR Spectroscopy and Computational Modeling. *Journal of the American Chemical Society* **2016,** *138* (23), 7325-7336.

25. Yang, X.; Epiepang, F. E.; Liu, Y.; Yang, R. T., Heats of adsorption on mixed-cation LiNa-LSX: Estimating SIII site occupancy by Li. *Chemical Engineering Science* **2018,** *178*, 194-198.

26. Dubbeldam, D.; Calero, S.; Ellis, D. E.; Snurr, R. Q., RASPA: molecular simulation software for adsorption and diffusion in flexible nanoporous materials. *Molecular Simulation* **2016,** *42* (2), 81-101.

27. Beauvais, C.; Guerrault, X.; Coudert, F.-X.; Boutin, A.; Fuchs, A. H., Distribution of Sodium Cations in Faujasite-Type Zeolite: A Canonical Parallel Tempering Simulation Study. *The Journal of Physical Chemistry B* **2004,** *108* (1), 399-404.

28. Bates, S. P.; van Well, W. J.; van Santen, R. A.; Smit, B., Energetics of n-alkanes in zeolites: a configurational-bias Monte Carlo investigation into pore size dependence. *Journal of the American Chemical Society* **1996,** *118* (28), 6753-6759.

29. Keffer, D.; Gupta, V.; Kim, D.; Lenz, E.; Davis, H. T.; McCormick, A. V., A compendium of potential energy maps of zeolites and molecular sieves. *Journal of molecular graphics* **1996,** *14* (2), 108-116.

30. Palomino, M.; Corma, A.; Rey, F.; Valencia, S., New insights on CO_2-methane separation using LTA zeolites with different Si/Al ratios and a first comparison with MOFs. *Langmuir* **2010,** *26* (3), 1910-7.

31. Pham, T. D.; Liu, Q.; Lobo, R. F., Carbon dioxide and nitrogen adsorption on cation-exchanged SSZ-13 zeolites. *Langmuir* **2013,** *29* (2), 832-9.

32. Pluth, J. J.; Smith, J. V., Accurate redetermination of crystal structure of dehydrated zeolite A. Absence of near zero coordination of sodium. Refinement of silicon, aluminum-ordered superstructure. *Journal of the American Chemical Society* **1980,** *102* (14), 4704-4708.

33. Takaishi, T.; Kato, M.; Itabashi, K., Determination of the ordered distribution of aluminum atoms in a zeolitic framework. Part II. *Zeolites* **1995,** *15* (1), 21-32.

34. Bates, S. P.; van Well, W. J. M.; van Santen, R. A.; Smit, B., Energetics of n-Alkanes in Zeolites: A Configurational-Bias Monte Carlo Investigation into Pore Size Dependence. *Journal of the American Chemical Society* **1996,** *118* (28), 6753-6759.

35. Lozinska, M. M.; Mangano, E.; Mowat, J. P. S.; Shepherd, A. M.; Howe, R. F.; Thompson, S. P.; Parker, J. E.; Brandani, S.; Wright, P. A., Understanding Carbon Dioxide Adsorption on Univalent Cation Forms of the Flexible Zeolite Rho at Conditions Relevant to Carbon Capture from Flue Gases. *Journal of the American Chemical Society* **2012,** *134* (42), 17628-17642.

36. Shiralkar, V. P.; Kulkarni, S. B., Sorption of carbon dioxide in cation exchanged Y type zeolites: Sorption isotherms and state of sorbed molecule. *Zeolites* **1984,** *4* (4), 329-336.

37. Zhu, L.; Seff, K., Reinvestigation of the Crystal Structure of Dehydrated Sodium Zeolite X. *The Journal of Physical Chemistry B* **1999,** *103* (44), 9512-9518.

38. Jaramillo, E.; Auerbach, S. M., New Force Field for Na Cations in Faujasite-Type Zeolites. *The Journal of Physical Chemistry B* **1999,** *103* (44), 9589-9594.

39. Ikeda, T.; Kodaira, T.; Oh, T.; Nisawa, A., K^+ ion distribution in zeolite ZK-4's with various Si/Al ratios and the contribution of K^+ ions to K cluster formation. *Microporous and Mesoporous Materials* **2003,** *57* (3), 249-261.

40. Snurr, R. Q.; Bell, A. T.; Theodorou, D. N., Prediction of adsorption of aromatic hydrocarbons in silicalite from grand canonical Monte Carlo simulations with biased insertions. *The Journal of Physical Chemistry* **1993,** *97* (51), 13742-13752.

41. Burtch, N. C.; Jasuja, H.; Dubbeldam, D.; Walton, K. S., Molecular-level insight into unusual low pressure CO_2 affinity in pillared metal–organic frameworks. *Journal of the American Chemical Society* **2013,** *135* (19), 7172-7180.

CHAPTER 3. A COUPLED-CLUSTER FORCE FIELD FOR PREDICTING ADSORPTION AND DIFFUSION OF SMALL MOLECULES IN SILICA ZEOLITES

3.1 Introduction and Literature Review

Zeolites are tetrahedral aluminosilicates that are widely used as adsorbents and catalysts due to their low cost and high thermal stability. More than 200 distinct zeolite topologies have been synthesized[1]. The performance of these materials depends on the adsorption and diffusion of molecules in their pores. Molecular simulations are often used to complement experiments in determining the viability of nanoporous materials such as zeolites for separations[2].

First-principles quantum mechanical methods (QM) can be used to accurately determine geometry and binding energies of molecules in nanoporous materials[3-6]. In particular, Density Functional Theory combined with coupled-cluster corrections (DFT/CC)[7] provides quantitatively accurate predictions for adsorbate-host interaction energies in zeolites[3, 5, 8]. However, it is too time-consuming to compute macroscopic properties such as adsorption isotherms, isosteric heat of adsorption and molecular diffusivities using these methods, because these properties require averaging over thousands or millions of configurations. This limitation is especially acute in settings where it is desirable to screen a large number of possible structures for some application of

interest. It is possible, however, to use Grand Canonical Monte Carlo (GCMC) and Molecular Dynamics (MD) simulations based on classical force fields to efficiently compute adsorption isotherms and diffusivities, respectively[9-14].

An obvious limitation of FF-based GCMC and MD simulations is that they can only make accurate predictions if accurate force fields (FFs) are available. The development of FFs that are simultaneously accurate and transferable is a difficult task. Generic FFs can predict adsorption isotherms in simple systems but can have issues with transferability in porous materials[15-17]. Experimentally-derived FFs can be fit to accurately reproduce adsorption isotherms in zeolites, but they can have limited transferability across zeolite topologies and cannot be systematically extended to additional adsorbates[9]. First-principles QM methods provide an accurate description of interatomic interactions without experimental input, so fitting FFs to reproduce energies from QM calculations provides a promising solution[9, 18]. However, these methods require either corrections to DFT (vdW-DF, DFT-D2, DFT-D3…) or a higher level of theory (post Hartree-Fock methods) to account for the dispersion interactions that are critical in adsorbate–adsorbent interactions in physisorption processes. Earlier work by our group developed first-principles-derived FFs to predict adsorption isotherms in pure-silica, Na-exchanged and K-exchanged zeolites for CO_2 and CH_4[2-4, 8]. This method relied on fitting a force field to reproduce the energies from electronic structure calculations for hundreds of randomly generated adsorption configurations. Similar methods for deriving FFs for adsorbates from QM calculations in nanoporous materials such as MOFs have been explored by multiple groups[19-22].

Another significant drawback of FFs for adsorption based on experimental adsorption data is that there is no reason to expect these FFs to accurately predict molecular

diffusivities. Fang et al.[3] and Jee at el.[23] have given examples in silica zeolites of FFs that reproduce experimental adsorption data but make predictions for diffusivities of CH_4 and CO_2 that are incorrect by orders of magnitude. This situation occurs because adsorption isotherms only require a correct description of configurations near energy minima (i.e. adsorption sites), while diffusion calculations must additionally have a correct description of configurations near transition states. Because transition states are less energetically favorable they have very little to no influence on adsorption isotherms, which in turn implies that information about these transition states cannot be obtained from adsorption data. Our group has shown previously that this issue can be systematically addressed in QM-derived FFs by using restrained molecular dynamics (or similar methods) to cover the whole volume accessible for adsorbates in a porous material[3].

In this work, we developed a first-principles-derived transferable FF that can be used to predict adsorption and diffusion for linear alkanes and alkenes, CO_2, N_2 and H_2O in pure silica zeolites at a coupled cluster level of accuracy. In Section 3.1, we describe the sampling approach used to fit the FF. We also assess the performance of our new FF for adsorption compared to experimental adsorption isotherms and simulated adsorption isotherms using other FFs. In Section 3.2, we used umbrella sampling (US) combined with transition state theory (TST) to predict self-diffusivities for several hydrocarbons in pure-silica zeolites. Our predicted diffusivities are compared to diffusivities predicted using other FFs and experimental data. We anticipate that this FF will be useful for making accurate predictions about the properties of the broad range of molecules we have considered in the enormous number of silica zeolites that are known experimentally and predicted *in silico*.

3.2 Materials and Simulation Details

3.2.1 Molecular and Zeolite Models

Adsorbate-adsorbate interactions were described by the TraPPE united atom (TraPPE-UA) potential for hydrocarbons[24], EPM-2[25] for CO_2, the 2LJ3CB.MSKM[26, 27] potential used by Makrodimitris et al. was used for N_2 interactions and the SPC/E model[28] was used for H_2O.

Experimental frameworks for the following pure-silica zeolites ITQ-3[29], ITQ-12[30], ITQ-29[31], ITQ-55[32], CHA[33], DDR[34], MFI[35] and TON[36] were used in our GCMC simulations. The modified Hill-Sauer force field was used to account for zeolite framework flexibility in MD simulations because of its ability to accurate predict window size distributions.[37]

3.2.2 Dispersion-Corrected Density Functional Theory Calculations

Periodic DFT calculations were performed using the VASP code[38, 39] based on the projector augmented wave formalism and pseudopotentials.[40, 41] A kinetic energy cutoff of 520 eV was used for plane-wave basis set to represent valence electrons (Si:$3s^2 3p^2$, O:$2s^2 2p^4$, C:$2s^2 2p^2$, N:$2s^2 2p^3$, and H:$1s^1$). Because of the large unit cells of the zeolites used in the calculations, a single *k*-point centered at the Γ-point of the Brillouin zone was used. The Perdew-Burke-Ernzerhof (PBE) exchange and correlation functional with the D2 dispersion correction from Grimme[42] was used for all DFT calculations. The density derived electrostatic and chemical method (DDEC6)[43, 44] was used to assign atomic charges based on DFT electronic densities. In order to account for the magnetic ground

state of oxygen molecule, spin-polarized calculations were used to determine the energy of O_2 in silica zeolites.

For interaction energies between molecules and zeolites, the coupled-cluster corrected density functional theory (DFT/CC) method was used.[7] This method assumes that the interaction can be decomposed as a sum of pairwise interactions between atoms and uses corrections accounting for the difference between coupled cluster results with large basis sets and DFT results for sets of judiciously chosen interacting molecules and clusters representing the zeolite[5, 6].

3.2.3 Molecular Dynamics Simulations

Classical molecular dynamics were carried out using LAMMPS code[45]. Simulations were performed at 300, 400, 500, 600, and 700 K in the NVT ensemble using a Nosé-Hoover thermostat[46, 47] with a chain length of 6 and a relaxation time of 0.1 ps. The velocity-Verlet algorithm was used to integrate the equations of motion with a time-step of 1 fs. The Ewald method[48] was used to compute long-range electrostatic interactions with a precision equal to 10^{-6}. A cutoff of 11 Å was set for both electrostatics and van der Waals interactions. Adsorbate-adsorbate interactions were described by the TraPPE united atom model[24]. The modified Hill-Sauer force field was used to account for zeolites framework flexibility in MD simulations.[37]

MD simulations are reported below for supercells of the experimental structures of ITQ-29[31] ($2 \times 2 \times 2$), CHA[33] ($3 \times 3 \times 3$, trigonal setting), DDR[34] ($2 \times 2 \times 1$), and MFI[35] ($2 \times 2 \times 2$). The volume and dimensions of each simulation box were equilibrated at the desired temperature using NPT MD simulations before using them in NVT MD production

runs. Each NPT MD simulation was performed at a pressure of 1 atm using a time step of 1 fs and a stress damping parameter of 100 fs. Periodic boundary conditions were used in all simulations.

Self-diffusion constants were derived through a linear fit of time evolution of mean-squared displacement (MSD) to Einstein equation, $\langle r^2 \rangle = 2dD_s t$ (r is adsorbate displacement, t is time, d is dimensionality of the system, and D_s is self-diffusion coefficient).[11] Each diffusion constant was averaged over data from five independent NVT MD runs with different initial velocity distributions. Each NVT MD trajectory was equilibrated for 1 ns and propagated for a production period of 30 ns.

3.2.4 Restrained Molecular Dynamics and Umbrella Sampling Simulations

Restrained molecular dynamics simulations were used to thoroughly sample the accessible volume in silica zeolites. The LTA zeolite framework was divided into slabs or bins parallel to a reference plane defined by atoms of the 8-ring window. A single probe molecule was then propagated in time using NVT MD for each window while restrained to the bin plane along the reaction coordinate direction. The bins were spaced by 1 Å covering a distance of 5 Å between LTA cage center and 8-ring window. The restraint was a harmonic spring bias with a force constant equal to 15 kcal/mol/Å^2 applied along the [001] direction using the collective variable module COLVRS[49] implemented in LAMMPS package. Each restrained NVT MD simulation was propagated for 200 ps after a 100 ps equilibration period. Configurations were recorded every 0.5 ps, resulting into 400 configurations per bin (2400 in total). A rigid zeolite framework was used in all restrained NVT MD simulations.

The same strategy described above was used for umbrella sampling (US) simulations to construct free energy profile for molecular hopping process of hydrocarbons. Instead of a rigid framework, the modified Hill-Sauer forcefield[37] was used to account for flexibility of different zeolites. The length of restrained NVT MD trajectories in each bin was 500 ps and configurations were recorded every 1 ps. The harmonic spring constant used in the bias was reduced to 5 kcal/mol/Å^2 in these calculations for better overlap between reaction coordinate histograms of adjacent bins. After data was generated using US simulations, the applied bias was removed and the free energy profile of the hopping process was constructed using the weighted histogram analysis method[50] (WHAM) implemented by Grossfield.[51]

3.2.5 GCMC Simulations

Single-component adsorption isotherms were performed using RASPA[52]. GCMC simulations were performed in a rigid zeolite frameworks. Although including framework vibrations can be important in making accurate adsorption predictions in some MOFs[53, 54], these effects are small for zeolites[55-57]. Sodalite cages in LTA (ITQ-29) and other regions inaccessible to adsorbates were blocked[58, 59]. Electrostatics were calculated using Ewald summation with a precision of 10^{-6} and dispersion interactions were computed using a 12 Å cutoff for a truncated potential with a tail correction. If the lattice parameter was smaller than 24 Å in any direction, the framework was expanded until the cell was large enough to satisfy the minimum image convention.

Sampling was started after the completion of 5×10^4 initialization cycles and thermodynamic properties were sampled over 10^5 cycles. This was shown in initial tests to

give well-converged results. Heats of adsorption[60] were calculated using a fluctuation formula.

3.3 Force Field Fitting Procedure

Our new force field was fit to DFT/CC energies because previous work by Fang et al. showed that DFT/CC can accurately predict adsorption energies in zeolites for methane[3] and CO_2[4, 8]. Additionally, previous FFs fit to DFT/CC energies showed good performance for CO_2 and CH_4 adsorption in pure-silica, Na-exchanged and K-exchanged zeolites[2]. The CC-corrections for CO_2 were taken from Pulido et al.[6]. The CC-correction curves for CH_4 were taken from Fang et al[3]. The remaining CC-correction curves were computed using the methods of Nachtigall and coworkers[6, 61].

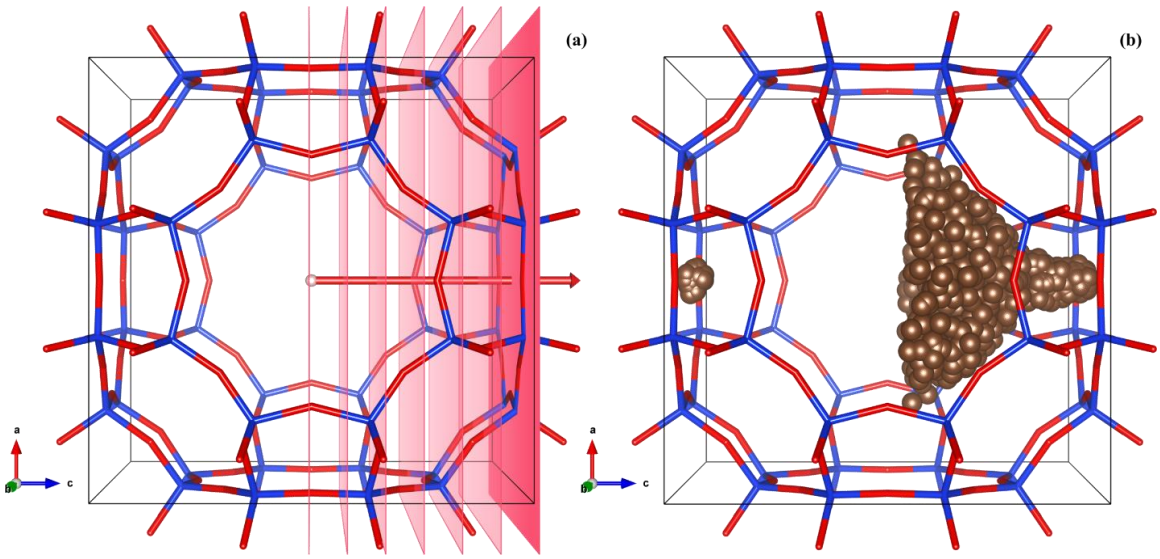

Figure 3.1 - An illustration of generating a set of configurations for CH_4 in Si-LTA using restrained molecular dynamics. (a) Configurational space is divided into bins (pink planes) along a reaction coordinate (pink arrow). (b) Configurations generated for CH_4 in Si-LTA used to fit the CCFF.

We generated a training set of configurations for each molecule using the constrained Molecular Dynamics methods shown in Figure 3.1. The parameters we used to generate the initial training sets were obtained using Lorentz-Berthelot mixing rules with zeolite silicon and oxygen parameters were represented by the Clay Force Field (CLAYFF)[62] and adsorbates were represented by TraPPE united atom (TraPPE-UA) potential for hydrocarbons[24], EPM-2[25] for CO_2, 2LJ3CB.MSKM[26, 27] for N_2 interactions and the SPC/E model[28] for H_2O. To ensure that our FF parameters were independent of our choice of initial force field we employed an iterative approach. After fitting our force field, we used the new force field parameters to generate another set of configurations. A force field was then fitted to reproduce the DFT/CC energies of the new set of configurations. This process continued until the force field parameters converged to within 5% of the previous iteration.

For each adsorbate, we generated configurations by performing Umbrella Sampling (US) along the **[001]** direction in ITQ-29 unless otherwise specified. The ITQ-29 atomic coordinates are taken from the experimental pure-silica ITQ-29 structure by Corma et al.[31]. Generating configurations using US ensured that both low energy configurations, which are relevant to adsorption predictions, and transition states, which are important for predicting diffusivities, were represented in the training set.

For our FF we assume interactions between each adsorbate atom and each zeolite atom can be described by pairwise van der Waals (vdW) and Coulombic terms,

$$E_{FF}(R_{ij}) = E_{vdW} + E_{Coul} = 4\varepsilon_{ij}\left[\left(\frac{\sigma_{ij}}{R_{ij}}\right)^{12} - \left(\frac{\sigma_{ij}}{R_{ij}}\right)^{6}\right] + \frac{q_i q_j}{R_{ij}} \qquad (3.1)$$

where ε_{ij} and σ_{ij} are the Lennard-Jones parameters that describe van der Waals interactions for a given pair, R_{ij}, is the distance between an adsorbate atom and zeolite atom, and q_i and q_j are the point charges on the adsorbate atom and framework atoms, respectively. Point charges on framework atoms (q_j) were computed based on the DDEC6 method[43, 44]. Point charges on adsorbate atoms were taken from the adsorbate-adsorbate potentials defined above.

The Coulombic energy was subtracted from the DFT/CC energy, and the Lennard-Jones potential terms were expressed in the same manner as in the work of Fang et al.[4],

$$E_{DFT/CC}(R_{ij}) - E_{Coul} = E_{vdW} = s_{12}\sum \frac{C_{12}^{ij}}{R_{ij}^{12}} - s_6 \sum \frac{C_6^{ij}}{R_{ij}^{6}} \qquad (3.2)$$

where C_6^{ij} and C_{12}^{ij}, interaction constants between species i and j, are based on Grimme's empirical dispersion expression[63] in the DFT-D2 method. s_{12} and s_6 are scaling factors for the repulsive and attractive vdW terms respectively. Linear least-squares regression was used to fit s_{12} and s_6. Next, we algebraically solved for the values of ε_{ij} and σ_{ij} based on the values of s_{12} and s_6, C_{12}^{ij} and C_6^{ij}. In order to ensure that our parameters were independent of the initial training set, we used the new values of σ_{ij} and ε_{ij} to generate a new training set of configurations. This procedure was repeated until the values of ε_{ij} and σ_{ij} were converged to within 5% of the previous iteration. Table 3.1 shows the final vdW parameters and charges for our new CCFF. We emphasize that no experimental data except the crystal structure data for ITQ-29 was used in determining this force field.

Table 3.1 - The final Lennard-Jones parameters and point charges for the CCFF.

Cross Species	ε/k_B (K)	σ (Å)	Element	Point Charge (e)
C_co2 – Si	49.946	3.616	Si	1.8708
C_co2 – Oz	29.228	3.189	Oz	-0.9354
O_co2 – Si	39.050	3.490	O_co2	-0.3256
O_co2 – Oz	23.523	3.063	C_co2	0.6512
N_n2 – Si	43.530	3.652	N_n2	-0.40484
N_n2 – Oz	25.838	3.213	N_com	0.80986
O_o2 - Oz	32.577	3.506	O_o2	-0.112
O_SPCE – Oz	41.721	3.385	O_com	0.224
CH_4_sp^3 - Oz	109.26	3.417	O_SPCE	-0.8476
CH_3_sp^3 - Oz	90.858	3.403	H_SPCE	0.4238
CH_2_sp^3 - Oz	57.481	3.660		
CH_sp^3 - Oz	25.649	4.101		
C_sp^3 - Oz	12.545	4.719		
CH_2_sp^2 – Oz	85.287	3.349		
CH_sp^2 – Oz	66.477	3.525		
C_sp^2 - Oz	12.197	4.470		

3.4 Force Field Predictions for Adsorption

3.4.1 Performance for Short, Linear Hydrocarbons

To evaluate the performance of our force field, we performed GCMC for short linear hydrocarbons in several common pure silica zeolites. The large number of experimental adsorption isotherms that are available[64] provides a rigorous test for our FF's prediction. Figure 3.2 shows a comparison between simulated (closed symbols) and experimental (open symbols) adsorption isotherms for methane, ethane, ethylene, propane and propylene. The simulated and experimental adsorption loadings typically differ by less than 0.1 mmol/g for most pressures, temperatures and topologies. The results in Figure 2 include 16 sets of experimental data for 5 distinct adsorbates, 5 distinct topologies and 7 distinct temperatures, demonstrating the transferability of the CCFF for adsorption. Additional adsorption isotherms for methane(Figure C.1), ethane(Figure C.2),

ethylene(Figure C.3), propane(Figure C.4) and propylene(Figure C.5) can be found in Appendix C.

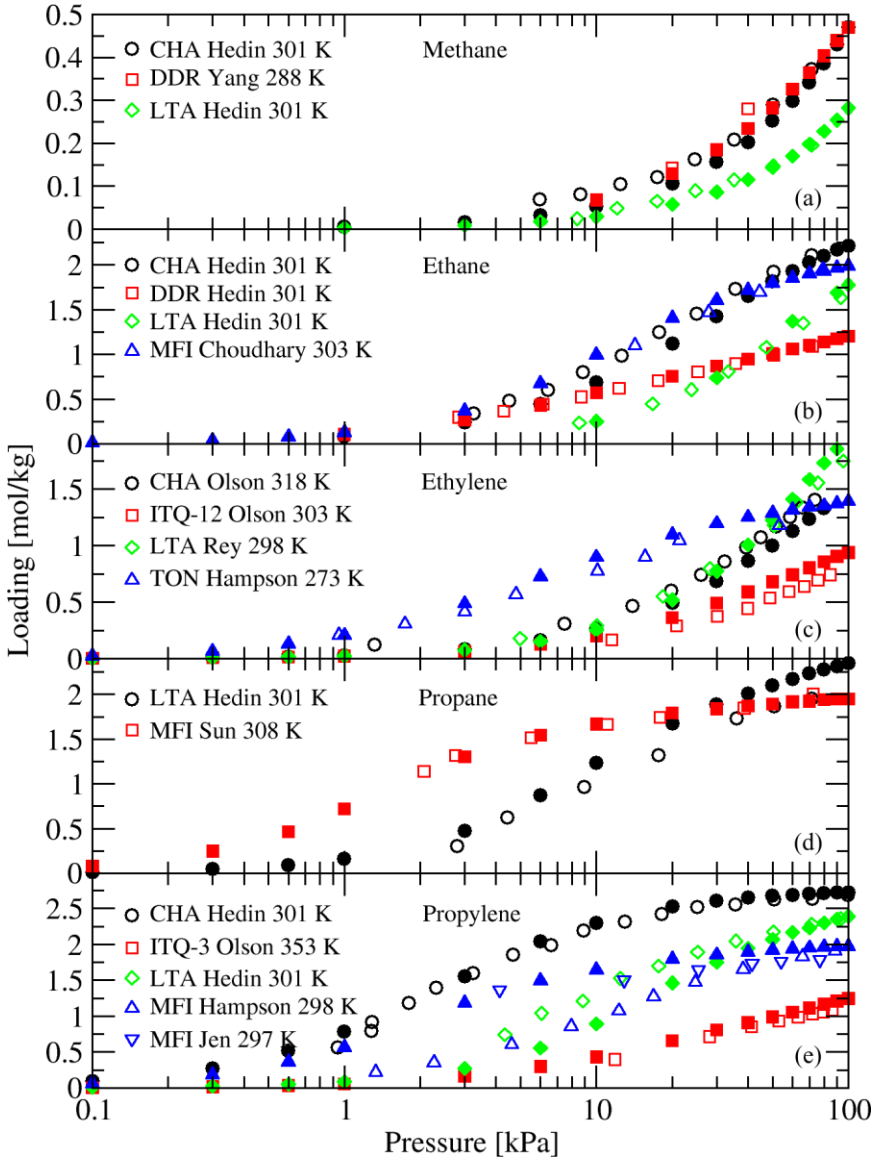

Figure 3.2 - A comparison of simulated (filled symbols) with experimental data[32, 64-68] (open symbols) for adsorption of (a) methane[64, 69], (b) ethane[64, 70], (c) ethylene[65, 67, 71], (d) propane[64, 72], and (e) propylene[64-66, 71]. The legends indicate the framework topology and temperature for each set of experimental data. The filled symbols correspond to the same topologies and temperatures.

The agreement between simulations and experiments was best for small, simple molecules like methane, ethane and ethylene in Figure 3.2(a-c). The low-pressure region of all methane, ethane and ethylene adsorption isotherms shows excellent agreement between simulated and experimental adsorption isotherms. The agreement at low pressure is a result of the increased importance of adsorbate-framework interactions at low pressures. Any smaller deviations at higher pressures are likely caused by the united atom approximation for adsorbate-adsorbate interactions.

The CCFF was also used to predict adsorption isotherms for C3 hydrocarbons in Figure 3.2(d and e). For propane, the experimental isotherms are in excellent agreement with experiments. In ITQ-29, propane diffusion is known to be slow[64]. However, the comparison between experiments and our simulations strongly suggests that Hedin et al.'s propane adsorption[64] measurements in ITQ-29 were equilibrated, because if they were not they would be highly unlikely to yield data that is consistent with all the other examples in Figure 3.2. Figure 3.2(e) shows more noticeable differences between simulated and experimental propylene adsorption isotherms in ITQ-29 and MFI. The adsorption of propylene is between the two sets of experimental data for Si-MFI (silicalite-1)[66, 71], so the results of simulations are within the experimental range. In ITQ-29, there is an underprediction of propylene adsorption by about 0.3 mmol/g in the 1-10 kPa pressure range. However, agreement is good at both low pressures and high pressures.

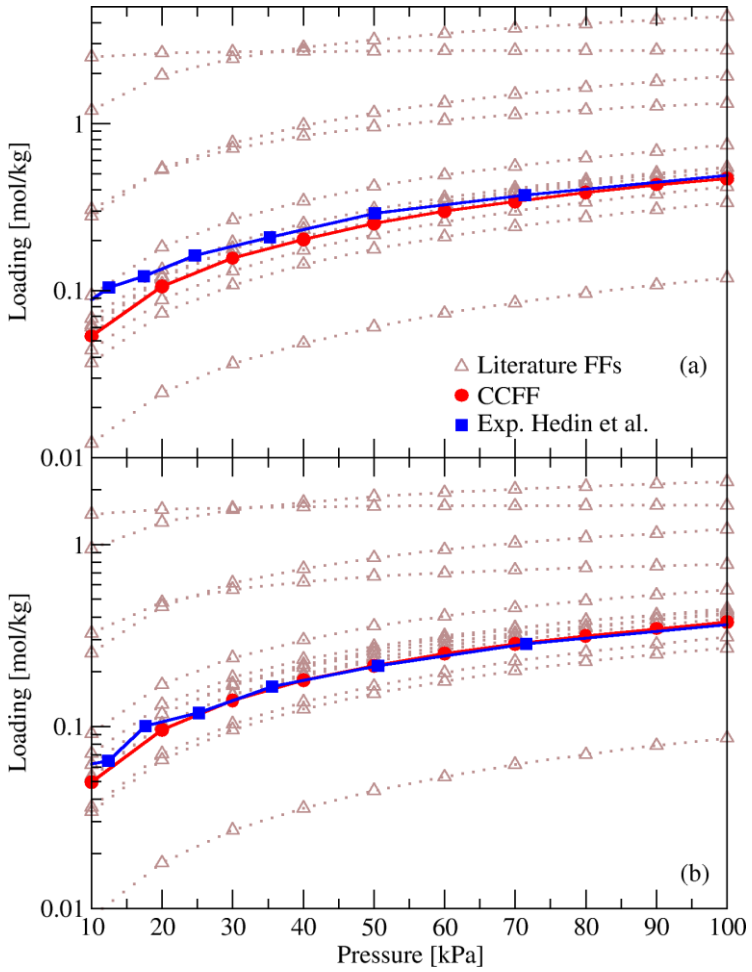

Figure 3.3 - Adsorption isotherms for CH_4 in (a) Si-CHA and (b) Si-DDR computed using CCFF (red) and 14[73-89] other FFs (black) from the literature. Most of the FFs show reasonable agreement with the experimental results of Hedin et al[64]. (blue symbols).

Many previous FFs have been fit to predict methane adsorption in silica zeolites[73-89]. To more rigorously benchmark our CCFF, we simulated CH_4 adsorption in Si-CHA and Si-DDR using the CCFF from this work and 14 other united-atom FFs from the literature. A table of all FF parameters and references can be found in Table C.1. Figure 3.3 shows the results of these simulations for CHA (Figure 3.3a) and DDR (Figure 3.3b). Our CCFF (red) showed excellent quantitative agreement when compared to experimental (blue) adsorption data from Hedin et al.[64] Of the fourteen literature FFs (black), eight predicted

FFs also predicted isotherms within 0.1 mmol/g of experimental adsorption isotherms over the pressure range 10 to 100 kPa. The best performing literature FFs were fit to large, robust experimental datasets, which included adsorption isotherms in multiple zeolite topologies[73, 76]. Of force fields that provided less accurate predictions, many were not originally intended to predict adsorption in Si-CHA or Si-DDR; they were fit, for example, to study diffusion in silicalite-1[74, 89], KFI[77], NaX[90] or zeolite 5A[88].

Even though many of these FFs predict quantitatively similar adsorption isotherms, these FFs span a wide range of Lennard-Jones parameters. This reinforces an observation from earlier work that adsorption isotherms in these kinds of systems are not specified by unique set of Lennard-Jones parameters.

3.4.2 Performance for CO_2 and N_2

The availability of experimental CO_2[68, 91, 92] and N_2[69, 92] adsorption isotherms in multiple pure-silica zeolites provides us with another rigorous test of our FF fitting methods. CO_2 and N_2 are both quadrupolar molecules with negatively charged ends and a positively charged center. To demonstrate the applicability of our approach to charged adsorbates, we compared experimental adsorption isotherms for CO_2 with our simulated adsorption isotherms in several commonly studied zeolites (LTA, MFI, CHA and DDR).

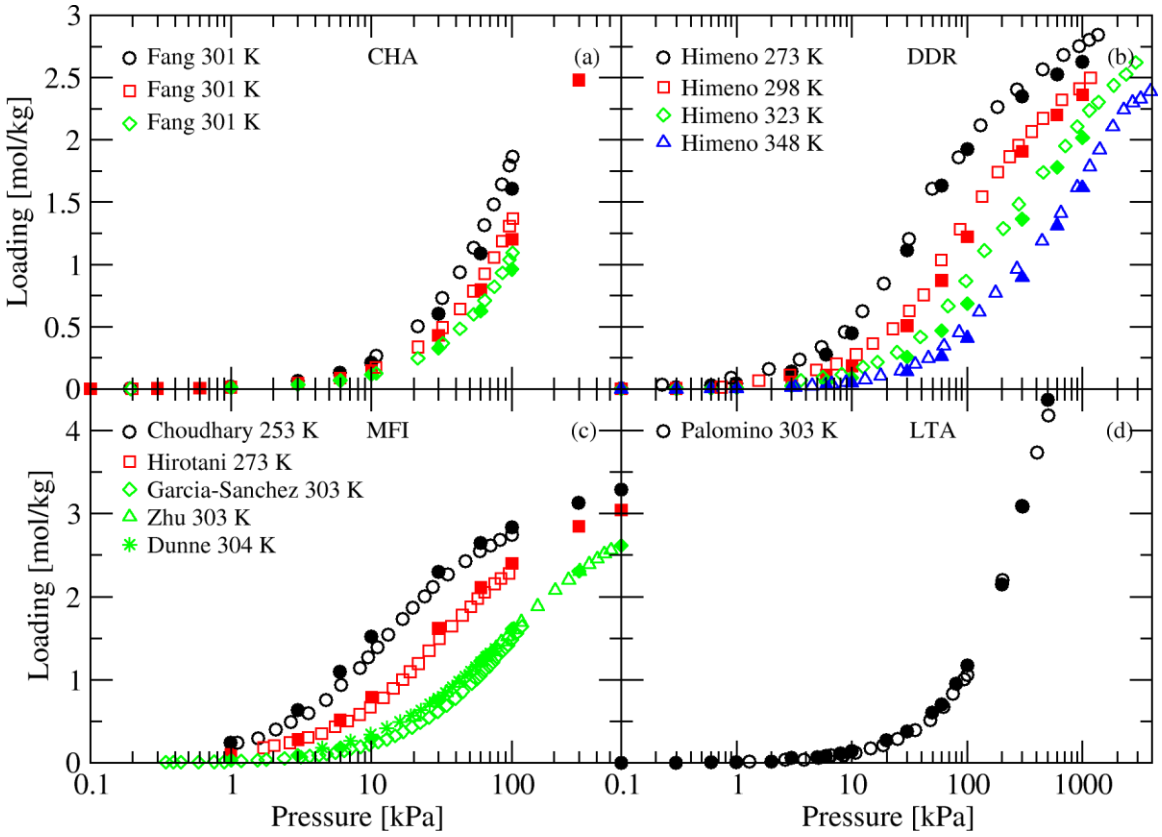

Figure 3.4 - Simulated (closed symbols) and experimental (open symbols) are shown for CO_2 in (a) CHA[4], (b) DDR[93], (c) MFI[70, 94, 95], and (d) and LTA[68] topologies.

Figure 3.4 shows a comparison of simulated and experimental CO_2 adsorption isotherms in pure-silica CHA, DDR, MFI and LTA. Every simulated loading was less than 10% different from the experimentally measured loadings at the same pressure. We also observe agreement between simulated and experimental heats of adsorption (see Figure 3.6). The CCFF predictions are the most accurate at low loadings, because we fit the adsorbate-framework interactions to DFT/CC energies, while adsorbate-adsorbate interactions play a larger role at higher loadings of CO_2. This indicates that our model accurately captures both the electrostatics and vdW interactions of CO_2 in pure-silica zeolites.

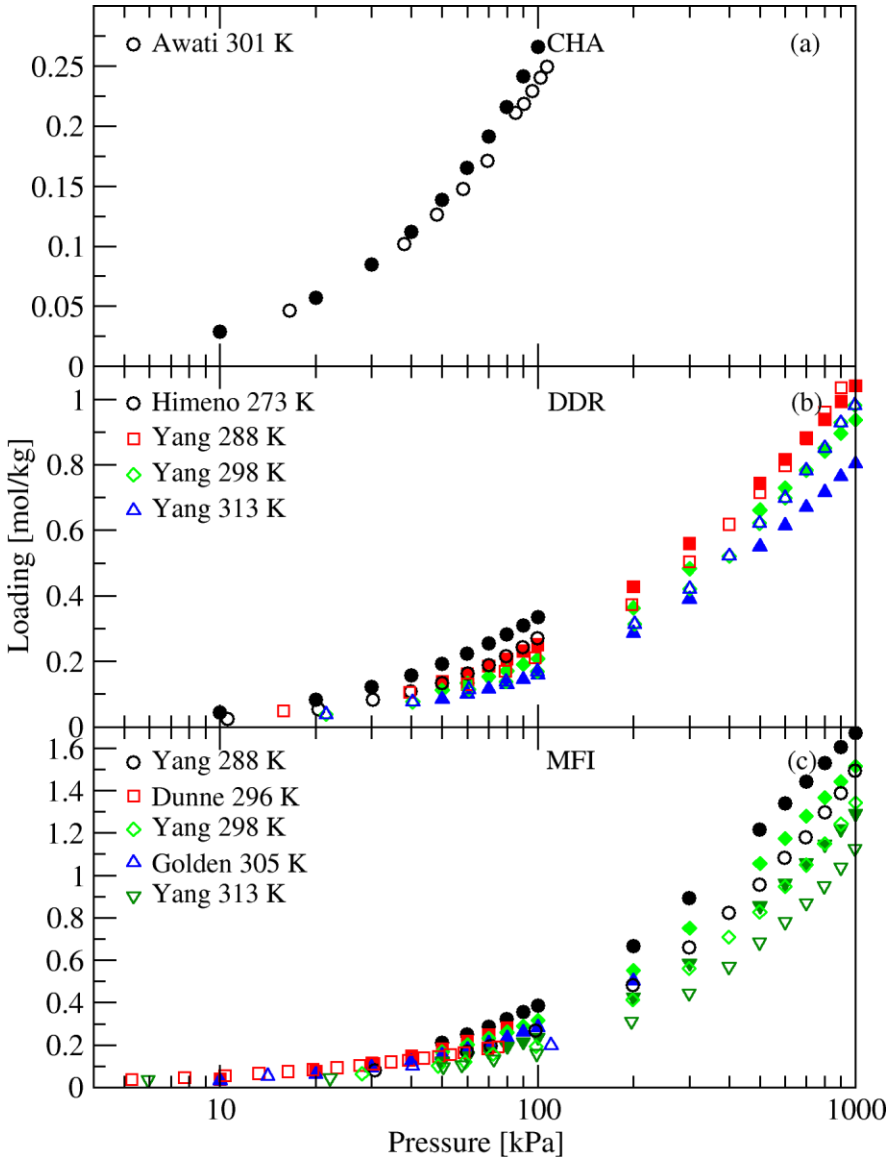

Figure 3.5 - Simulated (closed symbols) and experimental (open symbols) are shown for N_2 in (a) CHA[96], (b) DDR[69, 92], and (c) and MFI topologies[69, 95, 97].

Figure 3.5 shows a comparison of experimental and simulated N_2 adsorption isotherms in CHA, DDR and MFI. Overall, we see good agreement between simulations and experiments for 10 distinct sets of experimental data for three distinct topologies.

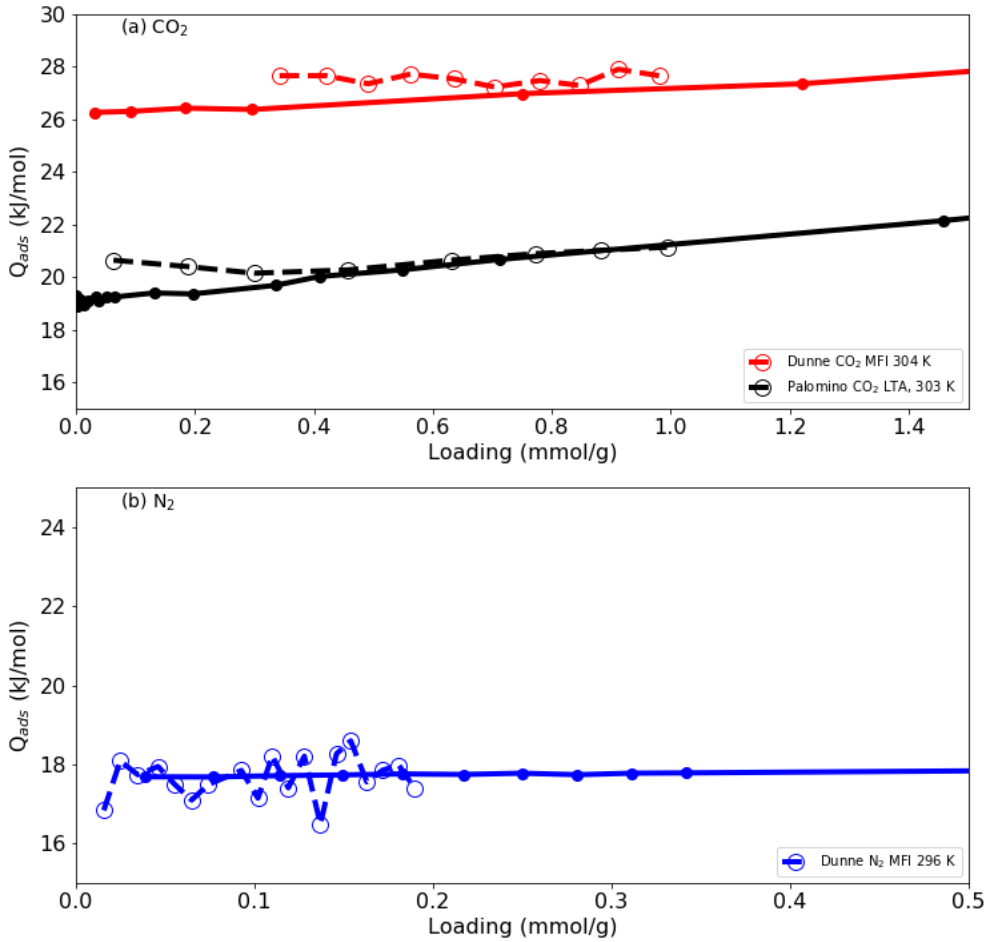

Figure 3.6 – Simulated (closed symbols) and experimental (open symbols) heats of adsorption for (a) CO_2 in MFI[98] (red) and LTA[68] (black) and (b) N_2 in MFI[98].

Figure 3.6 compares the heats of adsorption predicted by the CCFF with experimental data for both CO_2 and N_2. Simulated heats of adsorption were within 2 kJ/mol of experimental data for all loadings.

3.4.3 Fitting and Performance for H_2O

A rigorous test for our new CCFF methodology is to predict water intrusion in silica zeolites. Silica zeolites are typically very hydrophobic, resulting almost no water entering defect-free silica zeolites until pressures on the order of MPa are reached. The

hydrophobicity of silica zeolites causes the intrusion pressure to be extremely sensitive to heat of adsorption. Therefore, when attempting to predict the results of Trzpit et al.[99] for water intrusion in silicalite we fit our H_2O-zeolite interactions in a pure-silica MFI framework instead of the LTA framework we used above for CO_2, N_2 and hydrocarbons.

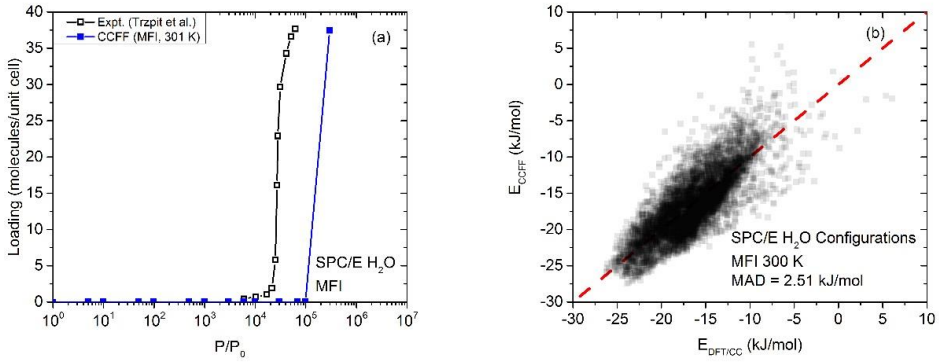

Figure 3.7 - A comparison of simulated (blue) with experimental (black) adsorption isotherms (a) for CCFF for H_2O and a comparison of DFT/CC energies and CCFF energies for SPC/E water (b) in pure-silica MFI. We observe reasonable agreement between simulated and experimental adsorption isotherms (a) and good agreement between DFT/CC energies and CCFF energies (b).

Figure 3.7(a) shows the experimental (black) and simulated (blue) H_2O adsorption isotherms in pure-silica MFI. According to simulations by NIST, SPC/E water model predicts a saturation pressure of 1.017 kPa[100] at 300 K, while the experimental saturation pressure (P_0) of water is 3.533 kPa at 300 K[101]. In order to make a better comparison of experimental and simulated adsorption isotherms, both sets of pressure were divided by their corresponding value of P_0. Our force field correctly predicts the order of magnitude of P/P_0 for water intrusion in pure-silica MFI. We did see that our FF slightly overpredicts the H_2O intrusion pressure, however our simulations assumed a defect-free MFI, while it

is very difficult to synthesize a completely defect-free zeolite. The presence of any Si(OH) groups could cause a decrease in intrusion pressure[99].

To demonstrate that our FF accurately predicted DFT/CC energies, we applied the constrained molecular dynamics methods from Figure 3.1 to the straight channels in MFI and calculated the energies using DFT/CC. The results are shown in Figure 3.7(b), which demonstrate excellent agreement between our CCFF energies and DFT/CC energies with a mean absolute deviation (MAD) of 2.51 kJ/mol.

3.5 Force Field Predictions for Diffusion

Because of the way we generated the training set of configurations for the CCFF we were able to fit the CCFF to capture the energetics of all states relevant to both adsorption and diffusion with DFT/CC-level accuracy. Previous sections demonstrated that the methods used to fit CCFF were transferable across zeolite topology and adsorbates. To test the performance of our CCFF in predicting diffusivities, we compared predictions of methane self-diffusivities to the experimental results from Hedin et al.[64] and to predictions we performed using the other FFs that were used to predict methane adsorption in Figure 3.3. A table of all FF parameters and references can be found in Table C.1.This comparison is shown for LTA, CHA and DDR topologies in Figure 3.8. These topologies were selected because of the high-quality experimental data as well as the small (8MR) window size of these materials.

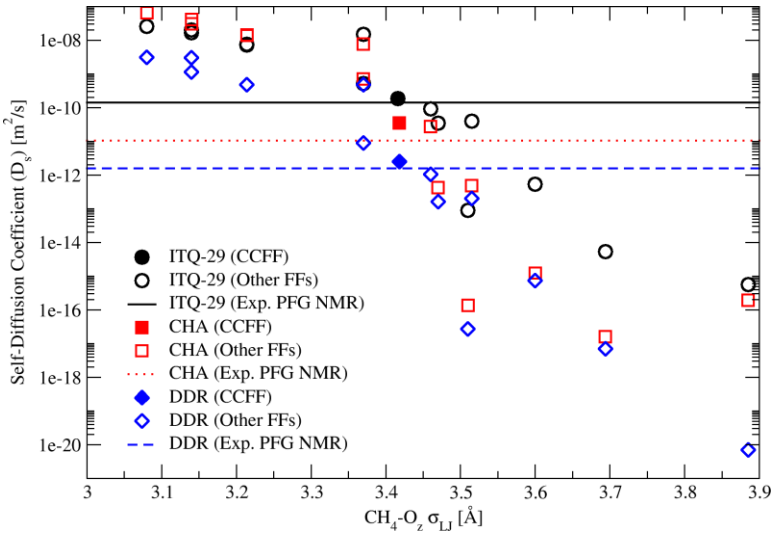

Figure 3.8 – Self-diffusivities were computed for CH_4 in ITQ-29 (black), CHA (red) and DDR (blue) using the CCFF (filled symbols) and the other FFs from Figure 3.3 (open symbols). The results were compared to the experimental results of Hedin et al.[64] (horizontal lines). Calculations were performed by Dr. Salah Boulfelfel.

Our CCFF's predictions, shown using filled symbols in Figure 3.8, for methane diffusivity in 8MR zeolites are better than any of the FFs that we compared to (open symbols). In fact, many of the predictions using other FFs predict diffusivities that are orders of magnitude faster or slower than the experiments of Hedin et al.[64] This further supports previous work by Fang et al.[3] and Jee at el.[23] that also show that FFs that can accurately predict adsorption isotherms do not necessarily predict self-diffusivities. Figure 3.8 shows a strong dependence of predicted self-diffusivities on the Lennard-Jones parameters, σ. Force fields with $\sigma_{CH4\text{-}O}$ between 3.4 and 3.5 made the most accurate predictions. The parameter. σ. is related to the size of the atom or united atom in the model. Larger values of sigma have a higher energy barrier for crossing the small 8MRs present in ITQ-29 (LTA), CHA and DDR. This dependence shows that an accurate value of σ is much more necessary for predicting diffusion than predicting adsorption.

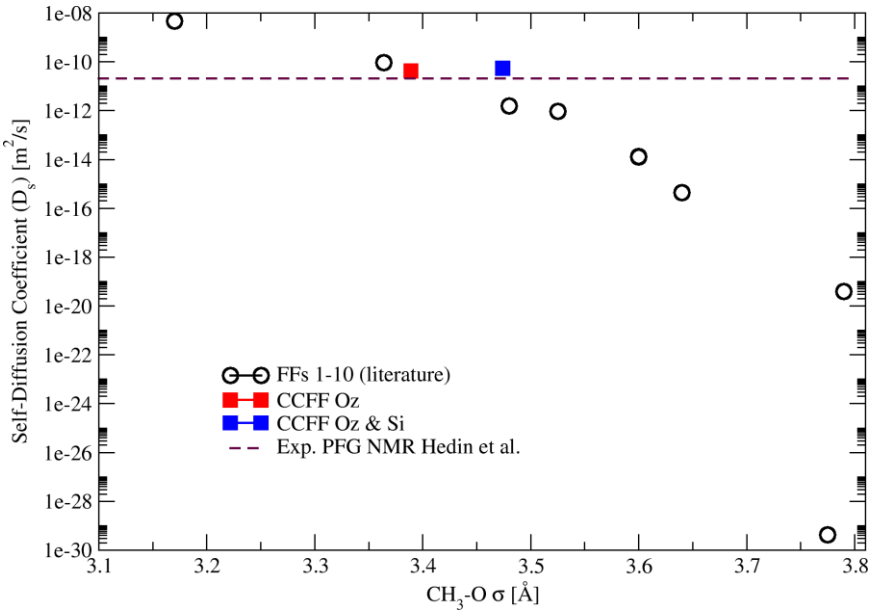

Figure 3.9 - Self-diffusivities were computed for C_2H_6 in ITQ-29 using the CCFF (red, filled symbol) and the other FFs from the literature[67, 73, 75, 76, 81, 82, 86, 102-108] (open symbols). The results were compared to the experimental results of Hedin et al.[64] (horizontal line). Calculations were performed by Dr. Salah Boulfelfel.

The same benchmarking procedure was also applied to ethane in ITQ-29. Ten force fields from previous literature[67,73,75,76,81,82, 86, 102-108] were compared to the CCFF for predicting ethane self-diffusivities in ITQ-29. These predictions were compared to the experimental results of Hedin et al[64] in Figure 3.9. Once again, the CCFF (red, closed symbols) performed better than any of the available literature FFs. The results also showed the same dependence of σ on ethane self-diffusivity as in Figure 3.8.

3.6 Conclusions

Fitting a transferable force field that can predict both adsorption and diffusion across a variety of adsorbates is a difficult task. Fitting FFs to reproduce experimental data can often lead to issues for transferability and these experimentally-derived FFs cannot be expected to predict diffusion, even when they offer accurate predictions for adsorption.

Fitting force fields to energies from accurate QM calculations provides a promising solution to the transferability issue in porous materials. However, many previous QM-derived force fields focus on fitting around energy minima, which are important for predicting adsorption, rather than including the energies from transition states, which are relevant to predicting diffusion, in their training sets.

In this work, we fit a force field for molecules in pure silica zeolites to highly accurate DFT/CC energies. When generating our training set, we forced each adsorbate to explore both energy minimum states as well as transition states by using restrained molecular dynamics. This ensured that the energies predicted by our CCFF were able to reproduce DFT/CC energies for both energy minimum states as well as transition states. Adsorption isotherms predicted by this CCFF were shown to agree with more than 20 sets of experimental adsorption isotherms spanning 5 distinct zeolite topologies, and 9 different adsorbates, which differed in size, shape and polarity. This indicates that our CCFF fitting methodology is transferable across topology and adsorbate.

The CCFF was also benchmarked against 14 other FFs from the literature and experimental data in 8MR zeolites. Although the CCFF and 7 other FFs were shown to accurately predict methane adsorption isotherms, the CCFF was the only FF to quantitatively predict methane diffusion for each zeolite topology tested. Our CCFF also had the best predictions for ethane diffusion in ITQ-29 when compared to 10 other FFs from the literature.

Our results indicate that our CCFF method can be used to model silica zeolites accurately and efficiently for separations that rely on both adsorption and diffusion.

Additionally, our CCFF fitting method has been demonstrated to be transferable to many different types of adsorbates, ranging from alkanes to H_2O. This greatly opens up the space of adsorbates and zeolite adsorbents that can be studied using these methods.

3.7 Chapter 3 References

1. Baerlocher, C.; McCusker, L. B.; Olson, D. H., *Atlas of zeolite framework types*. Elsevier: 2007.

2. Fang, H.; Kulkarni, A.; Kamakoti, P.; Awati, R.; Ravikovitch, P. I.; Sholl, D. S., Identification of high-CO_2-capacity cationic zeolites by accurate computational screening. *Chemistry of Materials* **2016,** *28* (11), 3887-3896.

3. Fang, H.; Awati, R.; Boulfelfel, S. E.; Ravikovitch, P. I.; Sholl, D. S., First-principles-derived force fields for CH_4 adsorption and diffusion in siliceous zeolites. *The Journal of Physical Chemistry C* **2018,** *122* (24), 12880-12891.

4. Fang, H.; Kamakoti, P.; Zang, J.; Cundy, S.; Paur, C.; Ravikovitch, P. I.; Sholl, D. S., Prediction of CO_2 adsorption properties in zeolites using force fields derived from periodic dispersion-corrected DFT calculations. *The Journal of Physical Chemistry C* **2012,** *116* (19), 10692-10701.

5. Nachtigall, P.; Delgado, M. R.; Nachtigallova, D.; Areán, C. O., The nature of cationic adsorption sites in alkaline zeolites—single, dual and multiple cation sites. *Physical Chemistry Chemical Physics* **2012,** *14* (5), 1552-1569.

6. Pulido, A.; Delgado, M.; Bludský, O.; Rubeš, M.; Nachtigall, P.; Areán, C. O., Combined DFT/CC and IR spectroscopic studies on carbon dioxide adsorption on the zeolite H-FER. *Energy & Environmental Science* **2009,** *2* (11), 1187-1195.

7. Bludsky, O.; Rubes, M.; Soldan, P.; Nachtigall, P., Investigation of the benzene-dimer potential energy surface: DFT/CCSD(T) correction scheme. *J Chem Phys* **2008,** *128* (11), 114102.

8. Fang, H.; Kamakoti, P.; Ravikovitch, P. I.; Aronson, M.; Paur, C.; Sholl, D. S., First principles derived, transferable force fields for CO_2 adsorption in Na-exchanged cationic zeolites. *Physical Chemistry Chemical Physics* **2013,** *15* (31), 12882-12894.

9. Fang, H.; Demir, H.; Kamakoti, P.; Sholl, D. S., Recent developments in first-principles force fields for molecules in nanoporous materials. *Journal of Materials Chemistry A* **2014,** *2* (2), 274-291.

10. Fuchs, A. H.; Cheetham, A. K., Adsorption of guest molecules in zeolitic materials: computational aspects. ACS Publications: 2001.

11. Sholl, D. S., Understanding macroscopic diffusion of adsorbed molecules in crystalline nanoporous materials via atomistic simulations. *Accounts of chemical research* **2006,** *39* (6), 403-411.

12. Smit, B.; Maesen, T. L., Molecular simulations of zeolites: adsorption, diffusion, and shape selectivity. *Chemical reviews* **2008,** *108* (10), 4125-4184.

13. Keskin, S.; Liu, J.; Rankin, R. B.; Johnson, J. K.; Sholl, D. S., Progress, opportunities, and challenges for applying atomically detailed modeling to molecular adsorption and transport in metal− organic framework materials. *Industrial & Engineering Chemistry Research* **2009,** *48* (5), 2355-2371.

14. Krishna, R., Diffusion in porous crystalline materials. *Chemical Society Reviews* **2012,** *41* (8), 3099-3118.

15. Garberoglio, G., Computer simulation of the adsorption of light gases in covalent organic frameworks. *Langmuir* **2007,** *23* (24), 12154-12158.

16. Yazaydın, A. O.; Snurr, R. Q.; Park, T.-H.; Koh, K.; Liu, J.; LeVan, M. D.; Benin, A. I.; Jakubczak, P.; Lanuza, M.; Galloway, D. B., Screening of metal− organic frameworks for carbon dioxide capture from flue gas using a combined experimental and modeling approach. *Journal of the American Chemical Society* **2009,** *131* (51), 18198-18199.

17. Pérez-Pellitero, J.; Amrouche, H.; Siperstein, F. R.; Pirngruber, G.; Nieto-Draghi, C.; Chaplais, G.; Simon-Masseron, A.; Bazer-Bachi, D.; Peralta, D.; Bats, N., Adsorption of CO_2, CH_4, and N_2 on zeolitic imidazolate frameworks: experiments and simulations. *Chemistry–A European Journal* **2010,** *16* (5), 1560-1571.

18. Sun, L.; Deng, W. Q., Recent developments of first-principles force fields. *Wiley Interdisciplinary Reviews: Computational Molecular Science* **2017,** *7* (1), e1282.

19. Zang, J.; Nair, S.; Sholl, D. S., Prediction of water adsorption in copper-based metal–organic frameworks using force fields derived from dispersion-corrected DFT calculations. *The Journal of Physical Chemistry C* **2013,** *117* (15), 7519-7525.

20. Dzubak, A. L.; Lin, L.-C.; Kim, J.; Swisher, J. A.; Poloni, R.; Maximoff, S. N.; Smit, B.; Gagliardi, L., Ab initio carbon capture in open-site metal–organic frameworks. *Nature chemistry* **2012,** *4* (10), 810.

21. Han, S. S.; Choi, S.-H.; Goddard III, W. A., Zeolitic imidazolate frameworks as H_2 adsorbents: Ab initio based grand canonical monte carlo simulation. *The Journal of Physical Chemistry C* **2010,** *114* (27), 12039-12047.

22. Lin, L.-C.; Lee, K.; Gagliardi, L.; Neaton, J. B.; Smit, B., Force-field development from electronic structure calculations with periodic boundary conditions: applications to gaseous adsorption and transport in metal–organic frameworks. *Journal of chemical theory and computation* **2014,** *10* (4), 1477-1488.

23. Jee, S. E.; Sholl, D. S., Carbon dioxide and methane transport in DDR zeolite: insights from molecular simulations into carbon dioxide separations in small pore zeolites. *Journal of the American Chemical Society* **2009,** *131* (22), 7896-7904.

24. Potoff, J. J.; Siepmann, J. I., Vapor–liquid equilibria of mixtures containing alkanes, carbon dioxide, and nitrogen. *AIChE journal* **2001,** *47* (7), 1676-1682.

25. Harris, J. G.; Yung, K. H., Carbon dioxide's liquid-vapor coexistence curve and critical properties as predicted by a simple molecular model. *The Journal of Physical Chemistry* **1995,** *99* (31), 12021-12024.

26. Makrodimitris, K.; Papadopoulos, G. K.; Theodorou, D. N., Prediction of permeation properties of CO_2 and N_2 through silicalite via molecular simulations. *The Journal of Physical Chemistry B* **2001,** *105* (4), 777-788.

27. Murthy, C.; Singer, K.; Klein, M.; McDonald, I., Pairwise additive effective potentials for nitrogen. *Molecular Physics* **1980,** *41* (6), 1387-1399.

28. Berendsen, H.; Grigera, J.; Straatsma, T., The missing term in effective pair potentials. *Journal of Physical Chemistry* **1987,** *91* (24), 6269-6271.

29. Camblor, M. A.; Corma, A.; Lightfoot, P.; Villaescusa, L. A.; Wright, P. A., Synthesis and Structure of ITQ-3, the First Pure Silica Polymorph with a Two-Dimensional System of Straight Eight-Ring Channels. *Angewandte Chemie International Edition in English* **1997,** *36* (23), 2659-2661.

30. Yang, X.; Toby, B. H.; Camblor, M. A.; Lee, Y.; Olson, D. H., Propene adsorption sites in zeolite ITQ-12: a combined synchrotron X-ray and neutron diffraction study. *The Journal of Physical Chemistry B* **2005,** *109* (16), 7894-7899.

31. Corma, A.; Rey, F.; Rius, J.; Sabater, M. J.; Valencia, S., Supramolecular self-assembled molecules as organic directing agent for synthesis of zeolites. *Nature* **2004,** *431* (7006), 287-290.

32. Bereciartua, P. J.; Cantín, Á.; Corma, A.; Jordá, J. L.; Palomino, M.; Rey, F.; Valencia, S.; Corcoran, E. W.; Kortunov, P.; Ravikovitch, P. I., Control of zeolite framework flexibility and pore topology for separation of ethane and ethylene. *Science* **2017,** *358* (6366), 1068-1071.

33. Diaz-Cabanas, M. J.; Barrett, P. A.; Camblor, M. A., Synthesis and structure of pure SiO_2 chabazite: the SiO_2 polymorph with the lowest framework density. *Chem Commun* **1998,** (17), 1881-1882.

34. Gies, H., Studies on Clathrasils .9. Crystal-Structure of Deca-Dodecasil 3r, the Missing Link between Zeolites and Clathrasils. *Z Kristallogr* **1986,** *175* (1-2), 93-104.

35. Vankoningsveld, H.; Vanbekkum, H.; Jansen, J. C., On the Location and Disorder of the Tetrapropylammonium (TPA) Ion in Zeolite ZSM-5 with Improved Framework Accuracy. *Acta Crystallogr B* **1987,** *43*, 127-132.

36. Marler, B., Silica-ZSM-22: synthesis and single crystal structure refinement. *Zeolites* **1987,** *7* (5), 393-397.

37. Boulfelfel, S. E.; Ravikovitch, P. I.; Koziol, L.; Sholl, D. S., Improved Hill-Sauer Force Field for Accurate Description of Pores in 8-Ring Zeolites. *J Phys Chem C* **2016,** *120* (26), 14140-14148.

38. Kresse, G.; Hafner, J., Ab-Initio Molecular-Dynamics Simulation of the Liquid-Metal Amorphous-Semiconductor Transition in Germanium. *Phys Rev B* **1994,** *49* (20), 14251-14269.

39. Kresse, G.; Furthmuller, J., Efficient iterative schemes for ab initio total-energy calculations using a plane-wave basis set. *Phys Rev B* **1996,** *54* (16), 11169-11186.

40. Kresse, G.; Joubert, D., From ultrasoft pseudopotentials to the projector augmented-wave method. *Phys Rev B* **1999,** *59* (3), 1758-1775.

41. Blochl, P. E., Projector Augmented-Wave Method. *Phys Rev B* **1994,** *50* (24), 17953-17979.

42. Grimme, S., Semiempirical GGA-type density functional constructed with a long-range dispersion correction. *J Comput Chem* **2006,** *27* (15), 1787-1799.

43. Limas, N. G.; Manz, T. A., Introducing DDEC6 atomic population analysis: part 2. Computed results for a wide range of periodic and nonperiodic materials. *RSC Adv* **2016,** *6* (51), 45727-45747.

44. Manz, T. A.; Limas, N. G., Introducing DDEC6 atomic population analysis: part 1. Charge partitioning theory and methodology. *RSC Adv* **2016,** *6* (53), 47771-47801.

45. Plimpton, S., Fast Parallel Algorithms for Short-Range Molecular-Dynamics. *J Comput Phys* **1995,** *117* (1), 1-19.

46. Frenkel, D.; Smit, B., Chapter 6 - Molecular Dynamics in Various Ensembles. In *Understanding Molecular Simulation (Second Edition)*, Academic Press: San Diego, 2002; pp 139-163.

47. Appendix E - Integration Schemes. In *Understanding Molecular Simulation (Second Edition)*, Academic Press: San Diego, 2002; pp 533-544.

48. Frenkel, D.; Smit, B., Chapter 12 - Long-Range Interactions. In *Understanding Molecular Simulation (Second Edition)*, Academic Press: San Diego, 2002; pp 291-320.

49. Fiorin, G.; Klein, M. L.; Henin, J., Using collective variables to drive molecular dynamics simulations. *Molecular Physics* **2013,** *111* (22-23), 3345-3362.

50. Kumar, S.; Rosenberg, J. M.; Bouzida, D.; Swendsen, R. H.; Kollman, P. A., Multidimensional Free-Energy Calculations Using the Weighted Histogram Analysis Method. *J Comput Chem* **1995,** *16* (11), 1339-1350.

51. Grossfield, A. "WHAM: the weighted histogram analysis method", version 2.0.9. http://membrane.urmc.rochester.edu/?page_id=126.

52. Dubbeldam, D.; Calero, S.; Ellis, D. E.; Snurr, R. Q., RASPA: molecular simulation software for adsorption and diffusion in flexible nanoporous materials. *Molecular Simulation* **2016,** *42* (2), 81-101.

53. Agrawal, M.; Sholl, D. S., Effects of Intrinsic Flexibility on Adsorption Properties of Metal–Organic Frameworks at Dilute and Nondilute Loadings. *ACS applied materials & interfaces* **2019,** *11* (34), 31060-31068.

54. Witman, M.; Ling, S.; Jawahery, S.; Boyd, P. G.; Haranczyk, M.; Slater, B.; Smit, B., The influence of intrinsic framework flexibility on adsorption in nanoporous materials. *Journal of the American Chemical Society* **2017,** *139* (15), 5547-5557.

55. Vlugt, T. J.; Schenk, M., Influence of framework flexibility on the adsorption properties of hydrocarbons in the zeolite silicalite. *The Journal of Physical Chemistry B* **2002,** *106* (49), 12757-12763.

56. García-Sánchez, A.; Dubbeldam, D.; Calero, S., Modeling adsorption and self-diffusion of methane in LTA zeolites: the influence of framework flexibility. *The Journal of Physical Chemistry C* **2010,** *114* (35), 15068-15074.

57. Fang, H.; Findley, J.; Muraro, G.; Ravikovitch, P. I.; Sholl, D. S., A Strong Test of Atomically-detailed Models of Molecular Adsorption in Zeolites Using Multi-laboratory Experimental Data for CO_2 Adsorption in Ammonium ZSM-5. *The Journal of Physical Chemistry Letters* **2019**.

58. Bates, S. P.; van Well, W. J.; van Santen, R. A.; Smit, B., Energetics of n-alkanes in zeolites: a configurational-bias Monte Carlo investigation into pore size dependence. *Journal of the American Chemical Society* **1996,** *118* (28), 6753-6759.

59. Keffer, D.; Gupta, V.; Kim, D.; Lenz, E.; Davis, H. T.; McCormick, A. V., A compendium of potential energy maps of zeolites and molecular sieves. *Journal of molecular graphics* **1996,** *14* (2), 108-116.

60. Hyla, A. S.; Fang, H.; Boulfelfel, S. E.; Muraro, G.; Paur, C.; Strohmaier, K.; Ravikovitch, P. I.; Sholl, D. S., Significant temperature dependence of the isosteric heats

of adsorption of gases in zeolites demonstrated by experiments and molecular simulations. *The Journal of Physical Chemistry C* **2019,** *123* (33), 20405-20412.

61. Bludský, O.; Rubeš, M.; Soldán, P.; Nachtigall, P., Investigation of the benzene-dimer potential energy surface: DFT/CCSD (T) correction scheme. *The Journal of chemical physics* **2008,** *128* (11), 114102.

62. Cygan, R. T.; Liang, J.-J.; Kalinichev, A. G., Molecular models of hydroxide, oxyhydroxide, and clay phases and the development of a general force field. *The Journal of Physical Chemistry B* **2004,** *108* (4), 1255-1266.

63. Grimme, S., Semiempirical GGA-type density functional constructed with a long-range dispersion correction. *J Comput Chem* **2006,** *27* (15), 1787-1799.

64. Hedin, N.; DeMartin, G. J.; Roth, W. J.; Strohmaier, K. G.; Reyes, S. C., PFG NMR self-diffusion of small hydrocarbons in high silica DDR, CHA and LTA structures. *Microporous and Mesoporous Materials* **2008,** *109* (1-3), 327-334.

65. Olson, D. H.; Camblor, M. A.; Villaescusa, L. A.; Kuehl, G. H., Light hydrocarbon sorption properties of pure silica Si-CHA and ITQ-3 and high silica ZSM-58. *Microporous and mesoporous materials* **2004,** *67* (1), 27-33.

66. Jen, H.; Otto, K., Chemisorption of alkenes on copper-exchanged ZSM-5 zeolite. *Catalysis letters* **1994,** *26* (1-2), 217-225.

67. Liu, B.; Smit, B.; Rey, F.; Valencia, S.; Calero, S., A new united atom force field for adsorption of alkenes in zeolites. *The Journal of Physical Chemistry C* **2008,** *112* (7), 2492-2498.

68. Palomino, M.; Corma, A.; Rey, F.; Valencia, S., New Insights on CO_2− Methane separation using LTA zeolites with different Si/Al ratios and a first comparison with MOFs. *Langmuir* **2010,** *26* (3), 1910-1917.

69. Yang, J.; Li, J.; Wang, W.; Li, L.; Li, J., Adsorption of CO_2, CH_4, and N_2 on 8-, 10-, and 12-membered ring hydrophobic microporous high-silica zeolites: DDR, silicalite-1, and beta. *Industrial & Engineering Chemistry Research* **2013,** *52* (50), 17856-17864.

70. Choudhary, V. R.; Mayadevi, S., Adsorption of methane, ethane, ethylene, and carbon dioxide on silicalite-l. *Zeolites* **1996,** *17* (5-6), 501-507.

71. Hampson, J.; Rees, L., Fundamentals of Adsorption. Kodansha/Elsevier: Tokoy/Amserdam: 1993; pp 259-266.

72. Sun, M. S.; Shah, D.; Xu, H. H.; Talu, O., Adsorption Equilibria of C1 to C4 Alkanes, CO_2, and SF_6 on Silicalite. *The Journal of Physical Chemistry B* **1998,** *102* (8), 1466-1473.

73. Bai, P.; Tsapatsis, M.; Siepmann, J. I., TraPPE-zeo: Transferable Potentials for Phase Equilibria Force Field for All-Silica Zeolites. *J Phys Chem C* **2013,** *117* (46), 24375-24387.

74. Demontis, P.; Suffritti, G. B.; Fois, E. S.; Quartieri, S., Molecular-Dynamics Studies on Zeolites .6. Temperature-Dependence of Diffusion of Methane in Silicalite. *Journal of Physical Chemistry* **1992,** *96* (3), 1482-1490.

75. Dubbeldam, D.; Calero, S.; Vlugt, T. J. H.; Krishna, R.; Maesen, T. L. M.; Beerdsen, E.; Smit, B., Force field parametrization through fitting on inflection points in isotherms. *Phys Rev Lett* **2004,** *93* (8).

76. Dubbeldam, D.; Calero, S.; Vlugt, T. J. H.; Krishna, R.; Maesen, T. L. M.; Smit, B., United atom force field for alkanes in nanoporous materials. *J Phys Chem B* **2004,** *108* (33), 12301-12313.

77. Fritzsche, S.; Haberlandt, R.; Karger, J.; Pfeifer, H.; Heinzinger, K., On the diffusion mechanism of methane in a cation-free zeolite of type ZK4. *Chem Phys* **1993,** *174* (2), 229-236.

78. Fritzsche, S.; Haberlandt, R.; Wolfsberg, M., Equilibration of the kinetic energy in small zeolite cavities - The thermalization effect of lattice vibrations and of mutual interaction in the diffusion of methane in a cation-free LTA zeolite. *Chem Phys* **2000,** *253* (2-3), 283-294.

79. Fritzsche, S.; Karger, J., Tracing memory effects in correlated diffusion anisotropy in MFI-type zeolites by MD simulation. *J Phys Chem B* **2003,** *107* (15), 3515-3521.

80. Goodbody, S. J.; Watanabe, K.; Macgowan, D.; Walton, J. P. R. B.; Quirke, N., Molecular Simulation of Methane and Butane in Silicalite. *J Chem Soc Faraday T* **1991,** *87* (13), 1951-1958.

81. Haberlandt, R., Transport processes in porous media: diffusion in zeolites. *Thin Solid Films* **1998,** *330* (1), 34-45.

82. Hussain, I.; Titiloye, J. O., Molecular dynamics simulations of the adsorption and diffusion behavior of pure and mixed alkanes in silicalite. *Microporous and Mesoporous Materials* **2005,** *85* (1-2), 143-156.

83. Jost, S.; Fritzsche, S.; Haberlandt, R., An MD study on the diffusion of a mixture of methane and xenon in silicalite. *Chem Phys Lett* **1997,** *279* (5-6), 385-388.

84. Kamat, M.; Dang, W. J.; Keffer, D., Agreement between analytical theory and molecular dynamics simulation for adsorption and diffusion in crystalline nanoporous materials. *J Phys Chem B* **2004,** *108* (1), 376-386.

85. Leroy, F.; Rousseau, B.; Fuchs, A. H., Self-diffusion of n-alkanes in silicalite using molecular dynamics simulation: A comparison between rigid and flexible frameworks. *Physical Chemistry Chemical Physics* **2004,** *6* (4), 775-783.

86. Martin, M. G.; Thompson, A. P.; Nenoff, T. M., Effect of pressure, membrane thickness, and placement of control volumes on the flux of methane through thin silicalite

membranes: A dual control volume grand canonical molecular dynamics study. *J Chem Phys* **2001,** *114* (16), 7174-7181.

87. Pascual, P.; Ungerer, P.; Tavitian, B.; Boutin, A., Development of a transferable guest-host force field for adsorption of hydrocarbons in zeolites. II. Prediction of alkenes adsorption and alkane/alkene selectivity in silicalite. *J Phys Chem B* **2004,** *108* (1), 393-398.

88. Ruthven, D. M.; Derrah, R. I., Transition-state theory of zeolitic diffusion. Diffusion of CH_4 and CF_4 in 5A zeolite. *J Chem Soc Farad T 1* **1972,** *68* (12), 2332-&.

89. Yashonath, S.; Bandyopadhyay, S., Surprising Diffusion Behavior in the Restricted Regions of Silicalite. *Chem Phys Lett* **1994,** *228* (1-3), 284-288.

90. Bezus, A. G.; Kiselev, A. V.; Lopatkin, A. A.; Du, P. Q., Molecular statistical calculation of the thermodynamic adsorption characteristics of zeolites using the atom–atom approximation. Part 1.—Adsorption of methane by zeolite NaX. *Journal of the Chemical Society, Faraday Transactions 2: Molecular and Chemical Physics* **1978,** *74*, 367-379.

91. Garcia-Sanchez, A.; Ania, C. O.; Parra, J. B.; Dubbeldam, D.; Vlugt, T. J.; Krishna, R.; Calero, S., Transferable force field for carbon dioxide adsorption in zeolites. *The Journal of Physical Chemistry C* **2009,** *113* (20), 8814-8820.

92. Himeno, S.; Takenaka, M.; Shimura, S., Light gas adsorption of all-silica DDR-and MFI-type zeolite: computational and experimental investigation. *Molecular Simulation* **2008,** *34* (10-15), 1329-1336.

93. Himeno, S.; Tomita, T.; Suzuki, K.; Yoshida, S., Characterization and selectivity for methane and carbon dioxide adsorption on the all-silica DD3R zeolite. *Microporous and Mesoporous Materials* **2007,** *98* (1-3), 62-69.

94. Hirotani, A.; Mizukami, K.; Miura, R.; Takaba, H.; Miya, T.; Fahmi, A.; Stirling, A.; Kubo, M.; Miyamoto, A., Grand canonical Monte Carlo simulation of the adsorption of CO_2 on silicalite and NaZSM-5. *Applied surface science* **1997,** *120* (1-2), 81-84.

95. Dunne, J.; Mariwala, R.; Rao, M.; Sircar, S.; Gorte, R.; Myers, A., Calorimetric heats of adsorption and adsorption isotherms. 1. O_2, N_2, Ar, CO_2, CH_4, C_2H_6, and SF_6 on silicalite. *Langmuir* **1996,** *12* (24), 5888-5895.

96. Awati, R. V. Development of accurate computational methods for simulations of adsorption and diffusion in zeolites. Doctoral Dissertation, Georgia Institute of Technology, Atlanta, GA, 30332, 2016.

97. Golden, T.; Sircar, S., Gas adsorption on silicalite. *Journal of Colloid and Interface Science* **1994,** *162* (1), 182-188.

98. Dunne, J.; Rao, M.; Sircar, S.; Gorte, R.; Myers, A., Calorimetric heats of adsorption and adsorption isotherms. 2. O_2, N_2, Ar, CO_2, CH_4, C_2H_6, and SF_6 on NaX, H-ZSM-5, and Na-ZSM-5 zeolites. *Langmuir* **1996,** *12* (24), 5896-5904.

99. Trzpit, M.; Soulard, M.; Patarin, J.; Desbiens, N.; Cailliez, F.; Boutin, A.; Demachy, I.; Fuchs, A., The effect of local defects on water adsorption in silicalite-1 zeolite: A joint experimental and molecular simulation study. *Langmuir* **2007,** *23* (20), 10131-10139.

100. Shen, V. K., Siderius, D.W., Krekelberg, W.P., and Hatch, H.W., *NIST standard reference simulation website*. National Institute of Standards and Technology: Gaithersburg, MD, 20899, 2012.

101. Bridgeman, O. C.; Aldrich, E. W., Vapor Pressure Tables for Water. *Journal of Heat Transfer* **1964,** *86* (2), 279-286.

102. Martin, M. G.; Siepmann, J. I., Transferable potentials for phase equilibria. 1. United-atom description of n-alkanes. *The Journal of Physical Chemistry B* **1998,** *102* (14), 2569-2577.

103. June, R. L.; Bell, A. T.; Theodorou, D. N., Molecular dynamics studies of butane and hexane in silicalite. *The Journal of Physical Chemistry* **1992,** *96* (3), 1051-1060.

104. Smit, B., Simulating the adsorption isotherms of methane, ethane, and propane in the zeolite silicalite. *The Journal of Physical Chemistry* **1995,** *99* (15), 5597-5603.

105. Jorgensen, W. L.; Madura, J. D.; Swenson, C. J., Optimized intermolecular potential functions for liquid hydrocarbons. *Journal of the American Chemical Society* **1984,** *106* (22), 6638-6646.

106. Wang, Y.; Hill, K.; Harris, J. G., Confined thin films of a linear and branched octane. A comparison of the structure and solvation forces using molecular dynamics simulations. *The Journal of chemical physics* **1994,** *100* (4), 3276-3285.

107. Schüring, A.; Auerbach, S. M.; Fritzsche, S.; Haberlandt, R., On entropic barriers for diffusion in zeolites: A molecular dynamics study. *The Journal of chemical physics* **2002,** *116* (24), 10890-10894.

108. Macedonia, M. D.; Maginn, E. J., A biased grand canonical Monte Carlo method for simulating adsorption using all-atom and branched united atom models. *Molecular Physics* **1999,** *96* (9), 1375-1390.

109. Talu, O.; Myers, A. L., Reference potentials for adsorption of helium, argon, methane, and krypton in high-silica zeolites. *Colloids and Surfaces A: Physicochemical and Engineering Aspects* **2001,** *187*, 83-93.

110. Vlugt, T.; Krishna, R.; Smit, B., Molecular simulations of adsorption isotherms for linear and branched alkanes and their mixtures in silicalite. *The Journal of Physical Chemistry B* **1999,** *103* (7), 1102-1118.

CHAPTER 4. A FORCE FIELD FOR PREDICTING ADSORPTION AND DIFFUSION OF SMALL MOLECULES IN CATIONIC ZEOLITES WITH COUPLED CLUSTER ACCURACY

4.1 Introduction and Literature Review

Zeolites are a class of nanoporous tetrahedral aluminosilicates that are widely used as catalysts and gas adsorbents because of their low cost and high thermal stability. More than 200 distinct zeolite topologies have been synthesized[1]. Cationic zeolites, which have a finite Si/Al ratio, also have extra-framework cations present to maintain charge neutrality in the zeolite. These extra-framework cations, such as Li, Na, and K, can have strong Coulombic interactions with polar and quadrupolar adsorbates such as H_2O and CO_2, which can be taken advantage of in separations processes, such as CO_2/CH_4 and CO_2/N_2 separations[2-6]. The performance of these materials as adsorbents depends on the adsorption and diffusion of adsorbates in their pores. These properties have a strong dependence on zeolite topology, Si/Al ratio, type of extra-framework cations present, and aluminum distribution[7, 8]. Considering the variability in zeolite properties, molecular simulations are often used to complement experiments in determining the viability of zeolites for separations.

Simulations involving cationic zeolites more complex than simulations in pure-silica zeolites because of the strong Coulombic interactions between adsorbates and extra-

framework cations as well the mobility of these cations during adsorption and diffusion processes. For example, "trapdoor" zeolites, such as Cs-CHA, K-CHA and Cs-RHO have shown promise for separating CO_2 from N_2 and CH_4[2, 5, 6, 9, 10] because the CO_2 interactions with extra-framework cations are strong enough to displace cations that would normally block diffusion channels in these materials. Because N_2 and CH_4 cannot displace these cations, they are not readily admitted into the zeolite, making these materials strongly kinetically selective for CO_2 uptake. This example indicates that an accurate description of cation-adsorbate and cation-framework interactions are required.

First-principles quantum mechanical (QM) methods can accurately predict both the geometry and binding energies of adsorbates in zeolites[11-14], as well as the energetics of cation motion in the presence of adsorbates[5, 15]. However, using QM methods to compute macroscopic properties such as adsorption isotherms, isosteric heats of adsorption and self-diffusivities is inefficient due to the large amount of computational power required. In these cases, classical force fields (FFs) can be used in Grand Canonical Monte Carlo (GCMC) and Molecular Dynamics (MD) simulations to efficiently compute adsorption isotherms and self-diffusivities respectively[16-21].

The accuracy of classical simulations depends on the accuracy of the force field model. Experimentally-derived FFs can be fit to accurately reproduce and predict adsorption isotherms in zeolites, but they have limited transferability across zeolite topologies and Si/Al ratio. Additionally, these experimentally-derived FFs cannot be systematically extended to additional adsorbates or types of extra-framework cations[16]. Force fields fit to reproduce energies from QM calculations, such as DFT/CC[11, 16, 22, 23], provide a promising solution, especially in situations where experimental data is less

abundant[10, 19] because they offer predictions that require no experimental inputs. In Chapter 3 we developed transferable first-principles-derived FFs that could accurately predict adsorption and diffusion for CO_2, N_2, H_2O, C1-C3 alkanes and C1-C3 alkenes in pure-silica zeolites. Our group has also previously developed first-principles-derived FFs to predict CO_2 and CH_4 adsorption isotherms in pure-silica, Na-exchanged and K-exchanged zeolites[7, 11, 12, 23] by fitting a FF to reproduce the energies from QM calculations. Similar strategies for deriving FFs, based on fitting to QM calculations in nanoporous materials such as MOFs, have been explored by multiple groups[24-27].

Another limitation of experimental FFs when studying cationic zeolites is the reliance on experimentally determined cation positions. When screening cationic zeolites for separations applications, there will often be cases where the distribution of extra-framework cations has not been determined experimentally[7]. In these cases, it is necessary to predict the cation distribution before simulating adsorption or diffusion. Jaramillo and Auerbach derived a force field for cation-framework interactions to replicate cation distributions in Na-FAU[28]. However, it is not clear whether these parameters will accurately predict cation positions or cation mobility for different species of extra-framework cations. To the best of our knowledge, there are no experimental or QM-derived force fields available in the literature to describe interactions between Li, Rb and Cs and a zeolite framework.

In this chapter, we used the methodology from Chapter 3 to develop a new DFT/CC-derived FF (CCFF) that can be used to predict adsorption and diffusion for CO_2, N_2, O_2 and CH_4 in zeolites exchanged with five monovalent cations, Li^+, Na^+, K^+, Rb^+, and Cs^+. Our FF is applicable to any Si/Al ratio and any cation composition for cations from

this selection of monovalent species, which has not demonstrated previously for adsorption or diffusion predictions. In Section 4.3, we discuss the fitting methodology and validation for our cation-framework component of our new CCFF. In Section 4.4, we demonstrate our approach to fitting adsorbate-cation and adsorbate-framework interactions in cationic zeolites. In Subsections 4.4.2-4., we show the results of our FF when predicting experimental adsorption isotherms for CO_2, N_2, and O_2 in cationic zeolites. In Section 4.5, we demonstrate the ability of our new CCFF to predict diffusion in cationic zeolites, even when the diffusion channels are blocked in zeolite 4A.

4.2 Materials and Simulation Details

4.2.1 Adsorbate Models

Adsorbate-adsorbate interactions were described by the EPM-2[29] model for CO_2. The 2LJ3CB.MSKM[30, 31] potential used by Makrodimitris et al. was used for N_2 interactions, and TraPPE was used for O_2[32]. We used the OPLS-AA[33] model for CH_4 because the orientation of CH_4 can influence the energetics of CH_4 – Na interactions. The parameters for this model were refit by Dr. Hanjun Fang to provide better agreement with bulk CH_4 properties. Additionally, Dr. Fang refit the force field for OPLS-AA CH_4 in silica zeolites using the same methods described in Chapter 3. The resulting FF parameters and information about the vapor-liquid coexistence curves and validation in silica zeolites are shown in Appendix E.

CCFF parameters were determined using the iterative approach described previously in Chapter 3. The FF parameters we used to generate the initial training sets for adsorbate-cation fitting were obtained from the work of Fang et al.[7] for CO_2 with Si, O, Al,

Na and K. When fitting the first iteration CCFF for CO_2 with Li, the Na-CO_2 Lennard-Jones (LJ) parameters from Fang et al.[7] were used as the initial parameter set. When fitting the first iteration CCFF for CO_2 with Rb and Cs, the K-CO_2 LJ parameters from Fang et al.[7] were used to generate the initial training sets. For N_2 and O_2, the initial training set generated using the LJ parameters for O_co2 – M^+ (M = Li, Na, K, Rb, Cs) and O_co2 – Al for the initial set of N_n2 (and O_o2) – M^+ and N_n2 (and O_o2) – Al parameters. O_co2 and C_co2 were used for the initial H_ch4 and C_ch4 parameters respectively for CH_4.

4.2.2 Zeolite Framework Models

To ensure accurate distributions of cations the atomic coordinates from zeolite framework atoms (Si, Al, O) used in our simulations were taken from experimental data for Li-CHA[34], Li-FAU[35], Na-LTA[36], Na-FAU[37], Na-KFI[38], K-LTA[39], K-FAU[40], K-CHA[2], K-KFI[38], Rb-FAU[41], Cs-LTA[42], Cs-RHO[2], and Cs-CHA[5]. When the lattice parameter was less than 24 Å, frameworks were expanded until the minimum image convention would be obeyed for a 12 Å vdW cutoff.

Many of the GCMC and parallel tempering simulations used in validating the CCFF involved frameworks with Si/Al > 1. For these frameworks, it is reasonable to expect that the distribution of framework aluminum may affect the cation distribution and subsequently the adsorption isotherms. The sensitivity of CO_2 adsorption isotherms to aluminum siting can be especially strong[8]. To account for this, we generated sparse, random and clustered Al distributions as described in Chapter 2. In the validation section, only the isotherms corresponding to the random aluminum distribution are shown unless

specific experimental information showing evidence for a nonrandom aluminum distribution is available. However, the results for the dependence of adsorption on aluminum distribution are shown in Appendix E.

4.2.3 Dispersion-Corrected Density Functional Theory Calculations

Periodic DFT calculations were performed using the VASP code[43, 44] based on the projector augmented wave formalism and pseudopotentials.[45, 46] A kinetic energy cutoff of 520 eV was used for plane-wave basis set to represent valence electrons (Si:$3s^2 3p^2$, Al:$3s^2 3p^1$, O:$2s^2 2p^4$, C:$2s^2 2p^2$, N:$2s^2 2p^3$, H:$1s^1$, Li:$1s^2 2s^1$, Na:$2p^6 3s^1$, K:$3p^6 4s^1$, Rb:$4s^2 4p^6 5s^1$, and Cs: $5s^2 5p^6 6s^1$). Because of the large unit cells of the zeolites used in the calculations, only one single *k*-point centered at the Γ-point of the Brillouin zone was used. The Perdew-Burke-Ernzerhof (PBE) exchange and correlation functional with the D2 dispersion correction from Grimme[47] was used for all DFT calculations. The density derived electrostatic and chemical method (DDEC6)[48, 49] was used to assign atomic charges based on DFT electronic densities. In order to account for the magnetic ground state of oxygen molecule, spin-polarized calculations were used to determine the energy of O_2 in silica zeolites.

For interaction energies between molecules and zeolites, the coupled-cluster corrected density functional theory (DFT/CC) method was used.[50] This method assumes that the interaction can be decomposed as a sum of pairwise interactions between atoms and uses corrections accounting for the difference between coupled cluster results with large basis sets and DFT results for sets of judiciously chosen interacting molecules and clusters representing the zeolite[13, 14].

4.2.4 Molecular Dynamics Simulations

Classical molecular dynamics were carried out using the LAMMPS code[51]. Simulations were performed at 300, 400, 500, 600, and 700 K in the NVT ensemble using a Nosé-Hoover thermostat[52, 53] with a chain length of 6 and a relaxation time of 0.1 ps. The velocity-Verlet algorithm was used to integrate the equations of motion with a time-step of 1 fs. The Ewald method[54] was used to compute long-range electrostatic interactions with a precision equal to 10^{-6}. A cutoff of 11 Å was set for both electrostatics and van der Waals interactions.

4.2.5 Restrained Molecular Dynamics

Restrained molecular dynamics simulations were used to thoroughly sample the accessible volume in silica zeolites. As shown in Figure 3.1, the LTA zeolite framework was divided into slabs or bins parallel to a reference plane defined by atoms of the 8-ring window (dark pink plane in Figure 3.1). A single probe molecule was propagated in time using NVT MD for each window while restrained to the bin plane along the reaction coordinate direction. The bins were spaced by 1 Å covering a distance of 5 Å between LTA cage center and 8-ring window. The restraint was a harmonic spring bias with a force constant equal to 15 kcal/mol/$Å^2$ applied along [001] direction using the collective variable module COLVRS[55] implemented in LAMMPS package. Each restrained NVT MD simulation was propagated for 200 ps after a 100 ps equilibration period. Configurations were recorded every 0.5 ps resulting into 500 configurations per bin (2525 in total). A rigid zeolite framework was used in all restrained NVT MD simulations.

4.2.6 Parallel Tempering Simulations

It has been shown that adsorption isotherms in cationic zeolites are sensitive to the positions of extra-framework cations[7, 23, 56, 57]. Therefore, it is important that the initial cation positions are properly equilibrated. Following the work of Fang et al.[7], extra-framework cation positions were equilibrated using parallel tempering. These simulations were carried out using RASPA[58]. As in Fang et al.[7], 9 structural replicas were used at T = 300 K, 390 K, 507 K, 659 K, 857 K, 1114 K, 1448 K, 1882 K and 2447 K, which is the temperature spacing suggested by Beauvais et al.[59] Electrostatic energies were calculated using the Ewald summation with a relative error of 10^{-6} and dispersion potentials had a cutoff of 12.0 Å. The positions of all framework atoms (Si, Al and O) were assumed to be rigid in all simulations. This same procedure was followed for mixed cation systems, such as Li/Na-LSX and Li/K-CHA.

4.2.7 GCMC Simulations

Single component adsorption isotherms were simulated using RASPA[58]. GCMC simulations were performed in a rigid framework. Although including framework vibrations can be important in making accurate adsorption predictions in some MOFs[60, 61], these effects are small for zeolites[22, 62, 63]. Sodalite cages in LTA (zeolite A) and FAU (zeolites X and Y), which are known to be inaccessible to adsorbates, were blocked in GCMC simulations[64, 65]. Electrostatic energies were calculated using the Ewald summation with a precision of 10^{-6}. Dispersion interactions were computed using a 12 Å cutoff for a truncated potential with a tail correction. When a unit cell had a lattice parameter shorter than 24 Å in any direction, the cell was expanded enough to satisfy the minimum image

convention. Sampling was started after 5×10^4 initialization cycles and thermodynamic properties were sampled over 10^5 cycles. This has been shown to give well-converged results[8]. More details involving the GCMC simulations and computation of isosteric heats of adsorption can be found in Appendix A.

4.3 Force Field for Cation-Framework Interactions

4.3.1 Cation-Framework Fitting Procedure

Determining the equilibrium positions of cations as well as the energetics of cation motion is crucial to describing both adsorption and diffusion in cationic zeolites. Previous work by Fang et al. showed that fitting cation-framework interactions to PBE-D2 energies can provide an accurate description of cation-framework interactions in Na and K-exchanged zeolites. The procedure used to fit cation-framework interactions in this work is similar to the work by Fang et al. [7, 23]. We used a Buckingham potential plus a Coulomb potential to describe interactions between the extra-framework cations and zeolite framework:

$$E_{FF}(R_{ij}) = A_{ij}e^{-B*R_{ij}} - \frac{C_{ij}}{R_{ij}^6} + \frac{q_i q_j}{R_{ij}} \quad (1)$$

Here A_{ij}, B_{ij} and C_{ij} are the Buckingham parameters for vdW interactions between species i and species j and q_i and q_j are the DDEC6 point charges on species i and j.

When fitting cation-framework interactions, we used experimental atomic coordinates for T-atoms and O atoms for Li-CHA[34], Na-KFI[38], K-KFI[38], Rb-LTA[66] and Cs-KFI[4]. Next, one cation was placed in each distinct type of experimentally-observed

cation site. For example, K-KFI was generated with Si/Al=23, which corresponds to 4 Al and 4 K^+ per unit cell. One cation was placed in each of the observed sites[38]: SI (center of hexagonal prism), SI´ (6MR), SII (nonplanar 8MR), and SIII (planar 8MR). These sites are illustrated in Figure 4.1. For each cation in the zeolite, we performed 500 random translation moves with a maximum displacement of 1 Å, while holding all other cations fixed in their equilibrium positions and computed energies using PBE-D2.

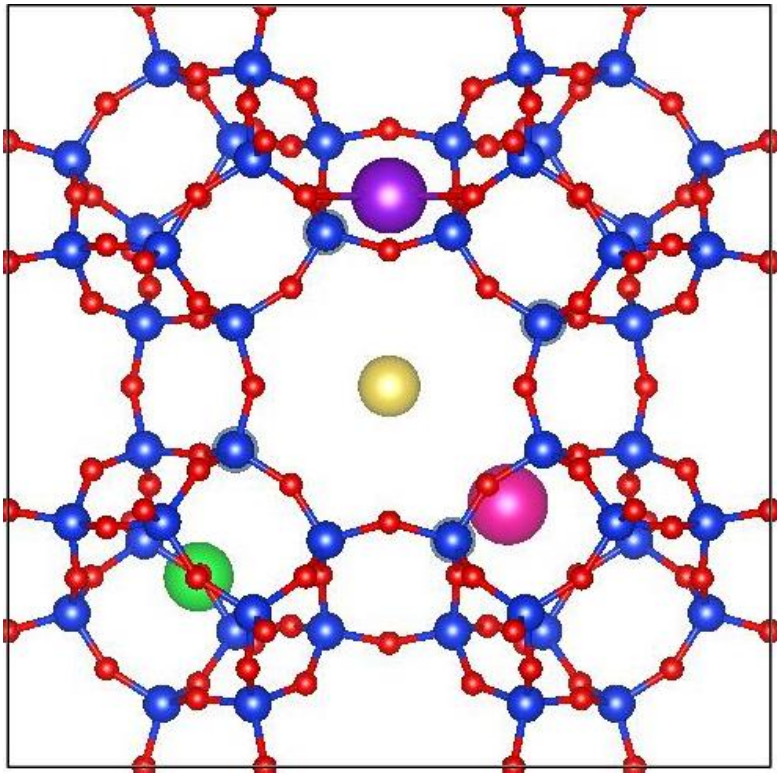

Figure 4.1 - The distinct cation positions in K-exchanged KFI from Pham et al.[38] are SI (green, center of hexagonal prism), SI´ (pink, 6MR), SII (purple, nonplanar 8MR), and SIII (yellow, planar 8MR). Si atoms are shown in blue, Al atoms are gray-blue and O atoms are red.

To avoid net framework charges in fitting, we fit the cation-framework interactions to relative energies using the framework with all cations at their experimental positions as the reference state. The relative Coulomb energies were computed using DDEC6 charges

and the same reference configuration. Subtracting the relative Coulomb energy from the relative PBE-D2 energy gave the relative vdW energy. Relative vdW energies were fit to the Buckingham potential. Parity plots for fitted energies vs PBE-D2 energies for Li, Na, K, Rb and Cs are shown in Figure D.1-D.5 respectively. Table 4.1 shows the fitted FF parameters**.**

Table 4.1 - The force field parameters obtained for cation-framework interactions are shown below. The vdW interactions are described by a Buckingham potential with parameters A, B and C. Coulombic interactions use DDEC6 point charges. Oxygen atoms connected to aluminum are considered to be Oa when the zeolite is fully exchanged with Na, K, Rb, or Cs, and OLi when the zeolite is fully exchanged with Li.

Cross-Species	**A (10^7 K)**	**B (Å^{-1})**	**C (10^6 K*Å^6)**	**Species**	**Charge (e)**
Li - O_z	3.516	4.723	0.1353	**Si**	1.8708
Na - O_z	5.581	3.985	0.9167	**Al**	1.7906
K - O_z	6.967	3.475	2.617	**O**	-0.9354
Rb - O_z	4.150	3.228	2.221	**Oa**	-1.1427
Cs - O_z	4.420	2.844	6.499	**OLi**	-1.1288
				Li	0.8538
				Na, K, Rb, Cs	0.9094

4.3.2 Validation of Cation-Framework Interactions

Accurate predictions for cation positions are important for predicting adsorption isotherms in cationic zeolites[7, 8, 23]. The cation distributions for many common zeolites such as Li-LSX[35], NaY[67] and zeolite 4A[36] (Na-LTA) have been observed experimentally. However, in many cases, especially for efforts aiming at comprehensive materials screening[7], the cation distribution is not always known. For these applications, it is

important to have an accurate description of cation-framework interactions. In this section, we demonstrate the accuracy for our cation-framework parameters in predicting the equilibrium cation distribution in Li-LSX[35] and Cs-LTA[42]. Additional cation-framework validation for zeolite 4A[36], NaY[67], KY[40, 68], and K-LTA (ZK-4)[39] can be found in Appendix D.

Li-LSX is an important material for N_2/O_2 separations because of its high affinity for N_2[57, 69]. The heats of adsorption and adsorption isotherms for N_2 in Li-LSX have been shown to be heavily influenced by the cation distribution. In Li-LSX, Li is typically located in SI´ (6MR inside the sodalite cages), SII (6MR in the supercage) and SIII (near 4MR inside the supercage). SI´ does not play a large role in adsorption because the sodalite cages are not accessible to adsorbates such as CO_2 and N_2. SII and SIII play a larger role in adsorption because of their locations inside the supercage. In particular, SIII is believed to be the strongest adsorption site for N_2 in Li-LSX because SII cations sit in the plane of a 6MR, while SIII cations are more exposed to adsorbates. SIII is also the crystallographic site that is least preferred by Li cations, which is the cause for the strong increase in N_2 heats of adsorption at Si/Al=1 and high levels of Li-exchange[35, 57]. Correct predictions for the cation distribution in Li-exchanged zeolites are crucial for predicting their usefulness in N_2/O_2 separations. Table 4.2 shows a comparison between the experimental[35] and simulated cation distributions in Li-LSX. In our simulations, we used the positions for Si, Al and O from experimental data[35] and computed the cation distribution using Parallel Tempering. Our results show excellent agreement with the experimental data from Feuerstein et al. [35] for both Li-LSX and Li/Na-LSX.

Table 4.2 - A comparison of experimental and simulated Li positions in Li-LSX. The experimental cation positions are described by Feuerstein et al.[35]

Composition	SI´	SII	SIII	Total
Expt. (96 Li, 0 Na)[35]	33	34	29	96
Simulated (96 Li, 0 Na)	32	32	32	96
Expt. (81 Li, 15 Na)[35]	32	32	17	81
Simulated (81 Li, 15 Na)	32	31	18	81

Predicting the cation distribution in Cs-LTA also presents an interesting challenge. In Cs-LTA, the Cs cation was observed by Heo and Seff[42] to be too large to fit in the plane of the 6 MR. Instead, Cs near the 6 MR face either the sodalite cage or the LTA cage. To test the accuracy of our Cs-O_z interactions, we performed parallel tempering to predict the cation distribution in Cs-LTA with Si/Al=1. The comparison of our simulated cation distribution with the results of Heo and Seff[42] is shown in Table 4.3. Our simulations were not only able to predict the number of each cation near the 8MR, 6MR and 4MR, but were also able to correctly predict the number of Cs on each side of the 6MR.

Table 4.3 - A comparison of experimental and simulated Cs positions in Cs-LTA. The experimental cation positions are described by Heo and Seff[42]. Sites Cs2 and Cs3 (6 MR α and 6 MR β) indicate whether the Cs located near the 6 MR is facing the LTA cage (α) or the SOD cage (β).

Cation Distribution	Cs1 (8 MR)	Cs2 (6 MR, α)	Cs3 (6 MR, β)	Cs4 (4 MR)
Expt.[42]	24	48	16	8
Simulated	24	48	16	8

4.4 Force Field for Adsorbate-Cation Interactions

4.4.1 Adsorbate-Cation Fitting Procedure

Accurate predictions for adsorption isotherms and self-diffusivities in cationic zeolites require an accurate description of adsorbate-cation interactions. Force fields fit to DFT/CC energies have shown good agreement with experiments for both CO_2 and N_2 in Na and K-exchanged zeolites[7, 23]. In this work, we also fit our FF to reproduce DFT/CC energies. We describe the interaction energies between species i and j using the sum of a Lennard-Jones potential and Coulomb potential,

$$E_{FF}(R_{ij}) = 4\varepsilon_{ij}\left[\left(\frac{\sigma_{ij}}{R_{ij}}\right)^{12} - \left(\frac{\sigma_{ij}}{R_{ij}}\right)^{6}\right] + \frac{q_i q_j}{R_{ij}} \tag{4.2}$$

where ε_{ij} and σ_{ij} are Lennard-Jones interaction parameters between species i and j and q_i and q_j are the DDEC6 charges of species i and species j respectively.

The methods used for fitting vdW parameters were the same as the constrained molecular dynamics-based methods used in Chapter 3. All parameters were fit to a training set generated by performing constrained molecular dynamics along the [001] direction in cation-exchanged LTA. When fitting cation-framework interactions, the coordinates for T-atoms and O-atoms were fixed at their experimental positions. The heats of adsorption for quadrupolar molecules such as CO_2 and, to a lesser extent, N_2 have a strong dependence on the number and type of cationic sites present. In order to ensure sampling of a variety of cationic sites, the LTA framework was given Si/Al = 3, with two cations placed in the 8 MR that did not face the [001] direction and four cations placed in 6 MR sites. The cation

positions were initialized using the corresponding experimental cation positions and then optimized at the PBE-D2 level, while fixing the locations of all other framework atoms.

Adsorbate configurations were generated using restrained molecular dynamics through the open 8 MR and energies were computed using the DFT/CC method, as in Chapter 3. The Coulombic energy was subtracted from the DFT/CC energy, and the Lennard-Jones potential terms were expressed in the same manner as in the work of Fang et al.[12],

$$E_{DFT/CC} - E_{Coul} = E_{vdW} = s_{12} \sum \frac{C_{12}^{ij}}{R_{ij}^{12}} - s_6 \sum \frac{C_6^{ij}}{R_{ij}^{6}} \quad (4.3)$$

where C_6^{ij} and C_{12}^{ij} are based on Grimme's empirical dispersion expression[70] in the DFT-D2 method. s_{12} and s_6 are scaling factors for the repulsive and attractive vdW terms respectively. Linear least-squares regression was used to fit s_{12} and s_6. Next, we algebraically solved for the values of ε_{ij} and σ_{ij} based on the values of s_{12} and s_6, C_{12}^{ij} and C_6^{ij}. In order to ensure that our parameters were independent of the initial training set, we used the new values of σ_{ij} and ε_{ij} to generate a new training set of configurations. This procedure was repeated until the values of ε_{ij} and σ_{ij} were converged to within 5% of the previous iteration. The final vdW parameters and charges for our new CCFF are shown for CO_2, N_2, O_2 and CH_4 in Table 4.4, Table 4.5, Table 4.6, and Table 4.7 respectively.

4.4.2 Predictions for CO_2 Adsorption

Cationic zeolites are often used in separations involving CO_2. The quadrupolar nature of CO_2 causes strong electrostatic interactions with extra-framework cations. This

leads to high selectivities for CO_2 over other adsorbates such as CH_4 and N_2[3, 5]. Accurate predictions for CO_2 adsorption are required in order to determine the viability of cationic zeolites in these separations. In this section, we demonstrate the transferability of our new CCFF for CO_2 across topology and composition in Li, Na, K, Rb and Cs-exchanged zeolites. The CCFF parameters for CO_2 in cationic zeolites are shown in Table 4.4. When validating CO_2 adsorption isotherms for Si/Al > 1, the adsorption isotherm corresponding to the framework with a random Al distribution was plotted unless the Al distribution has been determined experimentally. The effect of Al ordering for frameworks with Si/Al > 1 is described in Appendix E.

Table 4.4 - The fitted Lennard-Jones parameters for CO_2 – Al and CO_2 – M^+ (M = Li, Na, K, Rb, Cs) interactions are shown.

Cross-Species	**ε (K)**	**σ (Å)**	**Species**	**Charge (e)**
O_co2 – Al	39.117	3.054	**O_co2**	-0.3256
O_co2 – Li	239.899	2.139	**C_co2**	0.6512
O_co2 – Na	84.593	2.547		
O_co2 – K	138.48	2.881		
O_co2 – Rb	79.226	3.188		
O_co2 – Cs	54.177	3.457		
C_co2 – Al	49.763	3.167		
C_co2 – Li	281.822	2.247		
C_co2 – Na	103.153	2.659		
C_co2 – K	174.136	2.993		
C_co2 – Rb	100.71	3.306		
C_co2 – Cs	69.691	3.578		

Figure 4.2 shows a comparison between simulated and experimental CO_2 adsorption isotherms and isosteric heats of adsorption for Li-exchanged zeolites. All pressures in Figure 4.2(a) show reasonable agreement between experiments and simulations. Simulated isotherms at low pressures slightly overpredict adsorption isotherms for Li-KFI and Li/K-CHA. This same trend is observed for Li-KFI in Figure 4.2(b), when comparing the simulated isosteric heats of adsorption with the experimental results from Pham et al.[38]. The heats of adsorption are slightly overpredicted at low loadings, but the values agree well at higher loadings. When we computed DDEC6 charges on Li and CO_2 at short distances, the charge on Li decreased from 0.8538 to ~0.81. Our force field assumes constant charges on Li and CO_2, so we could not capture this charge transfer with our force field.

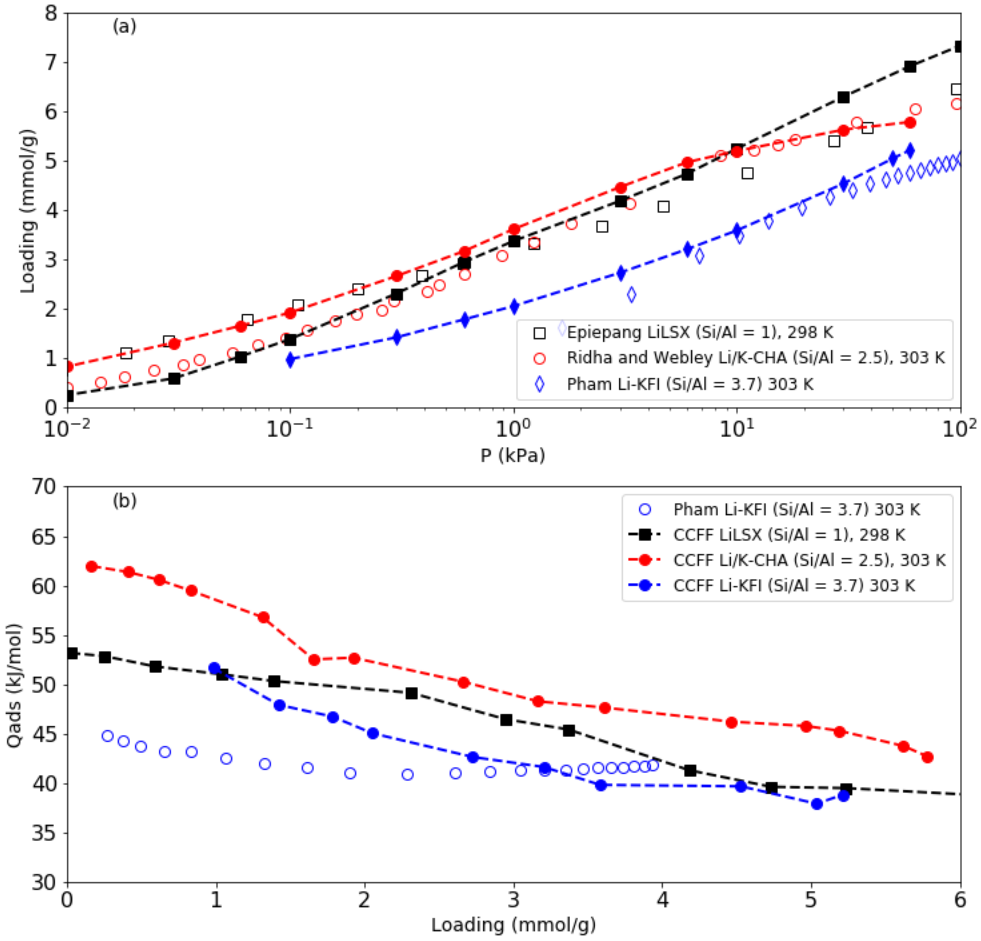

Figure 4.2 - A comparison of simulated (closed symbols) and experimental (open symbols) (a) adsorption isotherms and (b) heats of adsorption for Li-LSX (black), Li/K -CHA (red), and Li-KFI (blue). The experimental data for Li-LSX was taken from Epiepang et al[71]. The experimental data for Li/K – CHA was taken from Ridha and Webley[72]. The experimental data for Li-KFI was taken from Pham et al.[38]

CO_2 adsorption has been extensively studied in Na-exchanged zeolites. Figure 4.3 shows a comparison of simulated and experimental adsorption isotherms and heats of adsorption for NaX, NaY, LTA (Si/Al=1) and Na-KFI. Overall, there is good agreement between experiments and simulations. The agreement between experiments and

simulations is best at low pressures (P < 10 kPa). This indicates that the CCFF accurately describes adsorbate-cation interactions for the strongest adsorption sites. At pressures in the 10 -100 kPa range, the CCFF slightly overpredicts CO_2 loadings. This is reflected in the heats of adsorption, where the simulated heats of adsorption exceed experimental heats of adsorption by 3-5 kJ/mol at loadings above 3 mmol/g for NaX and LTA (Si/Al=1). Additional comparisons between experiments and simulations can be found in Appendix E.

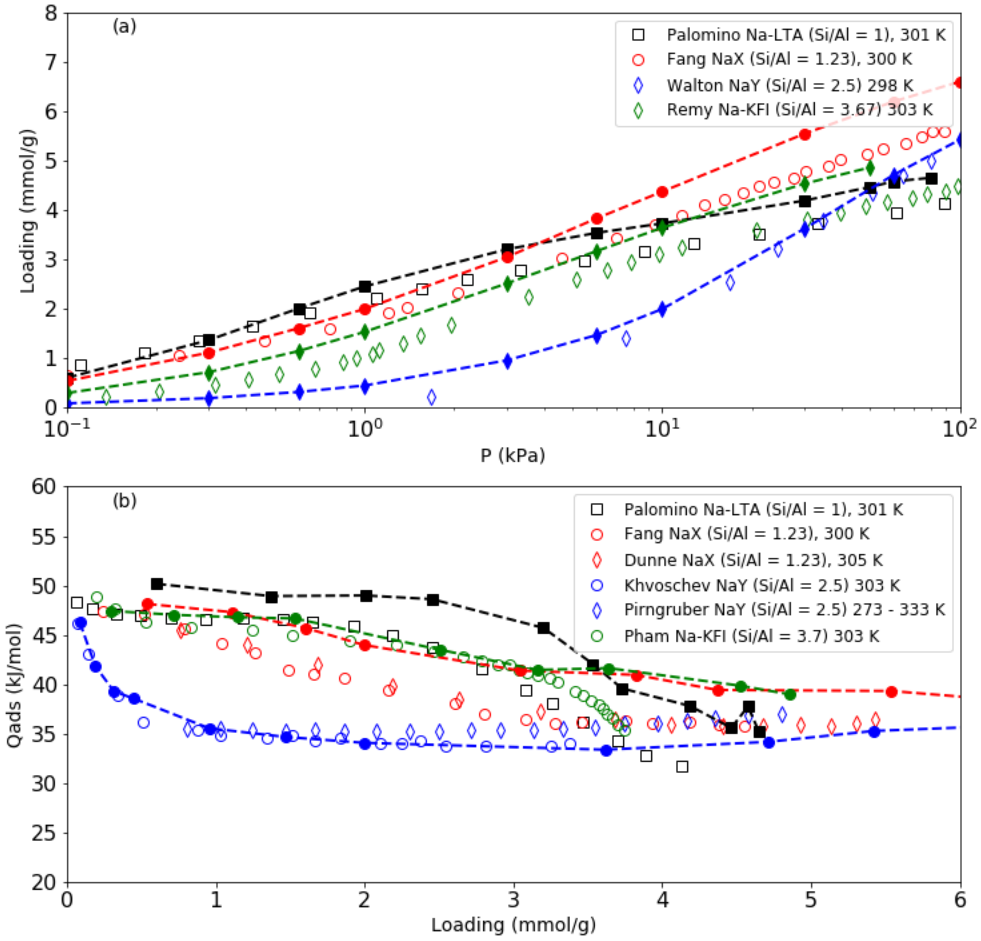

Figure 4.3 - A comparison of simulated (closed symbols) and experimental (open symbols) (a) adsorption isotherms and (b) heats of adsorption for Na-LTA (black), NaX (red), NaY (blue) and Na-KFI (green) are shown. The experimental data for Na-LTA was taken from Palomino et al.[3] NaX experimental data was taken from Fang et al.[23] and Dunne et al.[73] NaY experimental data was taken from Walton et al.[74], Khvoschev et al.[75] and Pirngruber at al.[56], KFI experimental data is taken from Remy et al.[76] and Pham et al.[38]

Figure 4.4 shows a comparison of experimental and simulated CO_2 adsorption isotherms and isosteric heats of adsorption in K-KFI, KY and K-CHA. Simulated and experimental CO_2 adsorption isotherms were typically within 0.5 mmol/g of one another and heats of adsorption were within 2-3 kJ/mol at loadings below 2 mmol/g. In K-KFI, the simulated adsorption isotherm agreed with the experimental adsorption isotherms from Remy et al.[76] however the experimental heats of adsorption from Pham et al.[38] were higher than the simulated heats of adsorption by about 4 kJ/mol at higher loadings. The cause of this difference was likely the Si/Al ratio used in the simulations. The K-KFI structure used in our GCMC simulations had Si/Al = 3.67 in order to compare to the adsorption isotherms. The Si/Al for the Pham experiments was slightly lower, resulting in a higher heat of adsorption for the experimental data because more cations were present in the experimental structure.

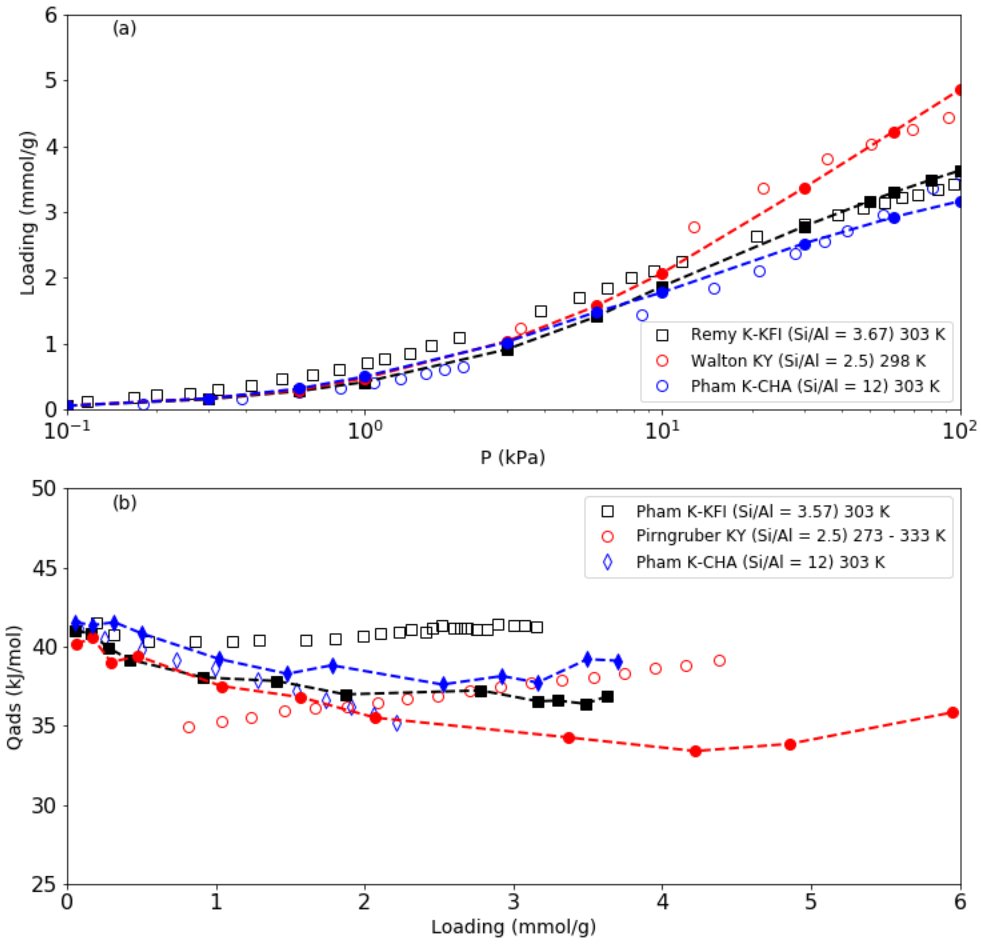

Figure 4.4 - A comparison of simulated (closed symbols) and experimental (open symbols) (a) adsorption isotherms and (b) heats of adsorption for K-KFI (black), KY (red), and K-CHA (Si/Al = 12) (blue) are shown. The experimental data for K-KFI was taken from Remy et al.[76] and Pham et al.[77]. KY experimental data was taken from Walton et al.[74] and Pirngruber et al.[56]

Some K, Rb and Cs-exchanged zeolites with 8-membered rings, such as CHA, LTA and RHO, have exhibited high selectivity for CO_2 over CH_4 and N_2 because of the "trapdoor" effect, in which CO_2 interactions are strong enough to displace the cation sitting at the 8 MR site, while other adsorbates cannot move the 8 MR cation[2, 5, 6, 15]. The

selectivity of these "trapdoor" zeolites has been shown to vary with zeolite composition and topology. However, to the best of our knowledge, no prior force fields have demonstrated the ability to describe adsorption and diffusion across all of zeolite compositions. Figure 4.4 demonstrated the ability of our CCFF to predict the strength of cation-CO_2 interactions in K-exchanged zeolites. Figure 4.5 shows a comparison of experimental and simulated adsorption isotherms for Na/Rb-Y and Cs-CHA. The CCFF accurately predicts CO_2 adsorption isotherms in both zeolites. Therefore, we can say with confidence that CCFF can describe both cation-framework interactions based on Table 4.3 and cation-CO_2 interactions based on Figure 4.4 and Figure 4.5. Therefore, the CCFF should, in principle, be useful to examine the selectivity of an array of "trapdoor" zeolites.

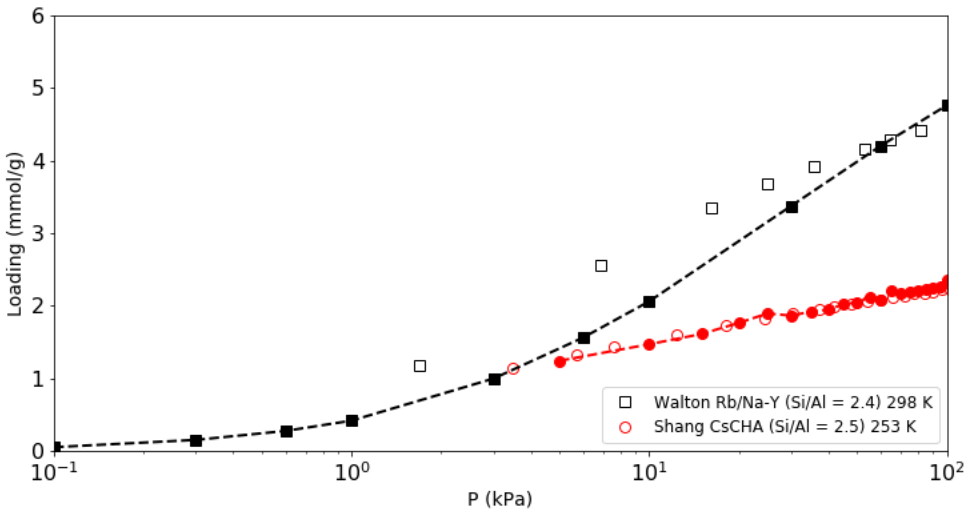

Figure 4.5 - A comparison of simulated (closed symbols) and experimental (open symbols) adsorption isotherms Rb/Na-Y (Si/Al = 2.4) and Cs-CHA (Si/Al = 2,5) are shown. The experimental data for Rb/Na-Y was taken from Walton et al.[74]. The experimental data for Cs-CHA was taken from Shang et al.[5]

4.4.3 Predictions for N_2 Adsorption

Li-LSX is a Li-exchanged Faujasite zeolite that is used for N_2/O_2 separations. The cation composition of Li/Na-LSX has been shown to strongly influence N_2 adsorption isotherms. Yang et al. showed for Li-LSX that when Li/Na-LSX is near 100% Li-exchanged, the N_2 heat of adsorption increased significantly because Li began to occupy the SIII sites in the FAU topology[57]. These sites are very exposed to adsorbate molecules, as opposed to SI´ sites which are located in the inaccessible sodalite cages.

The CCFF parameters for N_2 in cationic zeolites are shown in Table 4.5. Based on the results shown in Figure 4.6, our FF is able to accurately predict N_2 adsorption isotherms and the loading dependence of heats of adsorption in Li-LSX and Na-LSX. To the best of our knowledge, this has not been done before FF that was not fit to experimental data in Li-LSX. Therefore, the CCFF could be used to screen Li-exchanged zeolites for N_2 adsorption.

Table 4.5 - The fitted Lennard-Jones parameters for N_2 – Al and N_2 – M^+ (M = Li, Na, K, Rb, Cs) interactions are shown. The interaction parameters with Si and O_z can be found in **Chapter 3.**

Cross-Species	**ε (K)**	**σ (Å)**	**Species**	**Charge (e)**
N_n2 – Al	55.397	3.067	**N_n2**	-0.40484
N_n2 – Li	601.943	2.093	**N_com**	0.80968
N_n2 – Na	117.239	2.567		
N_n2 – K	153.183	3.068		
N_n2 – Rb	157.660	3.221		
N_n2 – Cs	137.420	3.410		
N_n2 – Al	55.397	3.067		

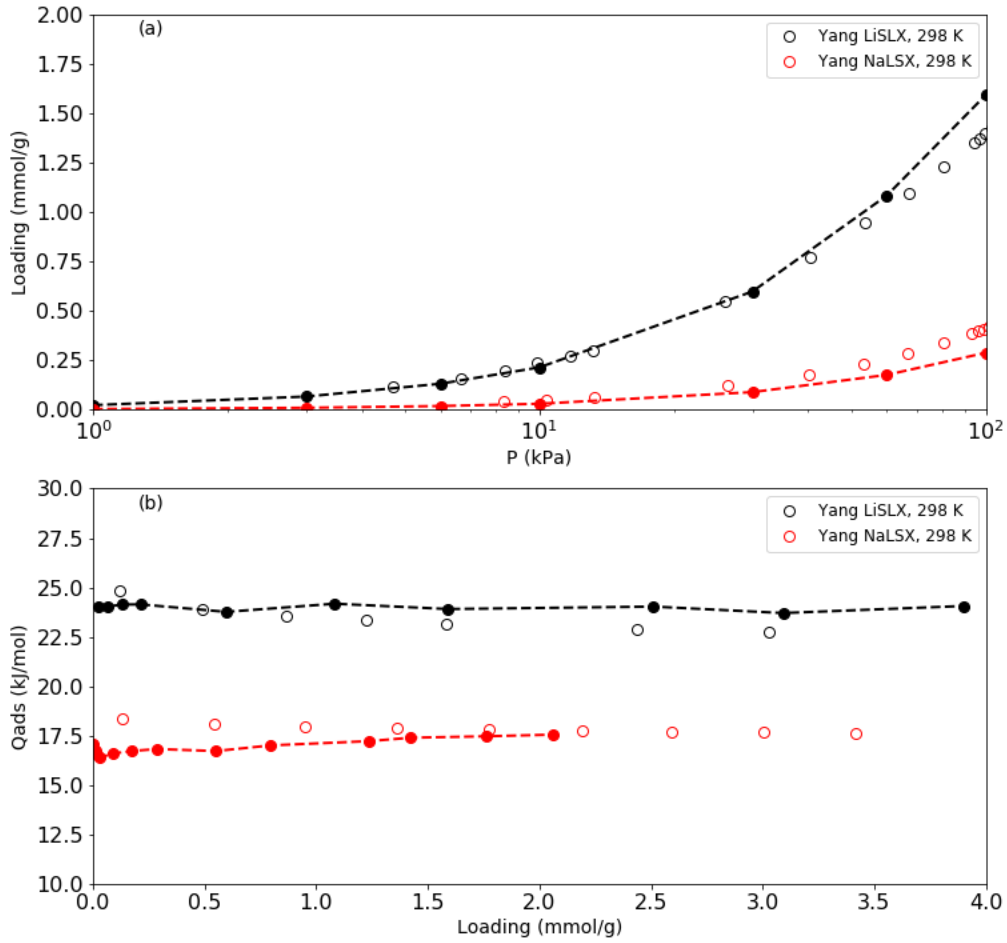

Figure 4.6 - A comparison of simulated and experimental N_2 (a) adsorption isotherms and (b) heats of adsorption in Li-LSX (black) and Na-LSX (red). The experimental data was taken from Yang et al.[57]

4.4.4 Prediction for O_2 Adsorption

Cation-O_2 interactions were also fit. The CCFF parameters for O_2 in cationic zeolites are shown in Table 4.6. However, there is not much experimental data available for O_2 adsorption isotherms. O_2 adsorption isotherms were studied in Li-LSX because of

the material's application to N_2/O_2 separations. Figure 4.7 shows a comparison of our simulated O_2 adsorption isotherms and two experimental adsorption isotherms in Li-LSX[69, 78]. The pressures and loadings were both plotted on a log scale because of the very low loadings of O_2 at low pressures. The experimental and simulated data even agree at loadings on the order of 10^{-2} mmol/g, which indicates the accuracy of our CCFF for weakly interacting adsorbates such as O_2. Based on the agreement between simulations and experiments for both N_2 and O_2 shown in Figure 4.6 and Figure 4.7, our CCFF could be used to screen for zeolites to use in N_2/O_2 separations.

Table 4.6 - The fitted Lennard-Jones parameters for O_2 – Al and O_2 – M^+ (M = Li, Na, K, Rb, Cs) interactions are shown. The interaction parameters with Si and O_z can be found in Table 3.1.

Cross-Species	**ε (K)**	**σ (Å)**	**Species**	**Charge (e)**
O_o2 – Al	59.174	3.330	**O_o2**	-0.112
O_o2 – Li	711.346	1.906	**O_com**	0.224
O_o2 – Na	317.234	2.308		
O_o2 – K	215.788	2.789		
O_o2 – Rb	31.690	3.263		
O_o2 – Cs	167.056	3.175		
O_o2 – Al	59.174	3.330		

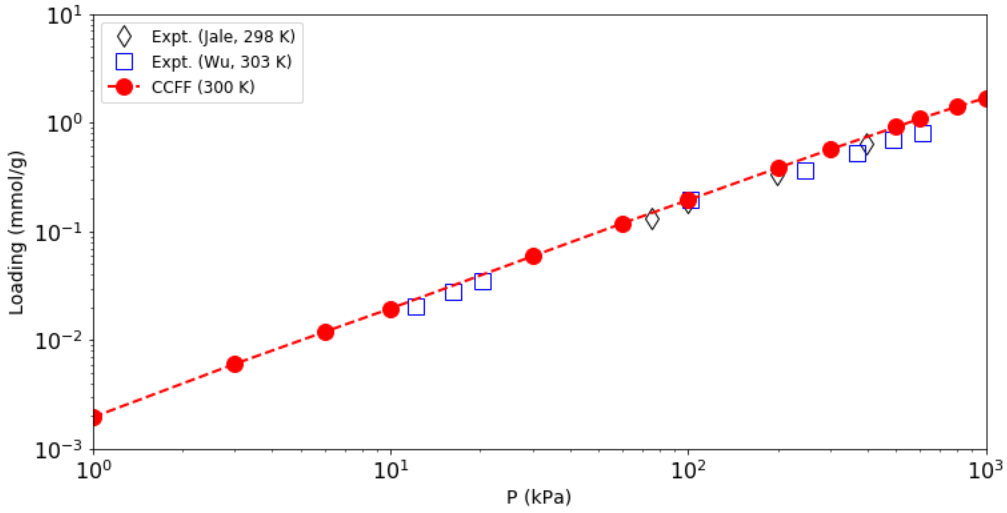

Figure 4.7 - Experimental O_2 adsorption isotherms in Li-LSX from the work of Jale et al[69]. and Wu et al[78]. compared to results for O_2 adsorption simulated with the CCFF.

4.4.5 Predictions for CH_4 Adsorption

Adsorption of CH_4 in cationic zeolites is significantly weaker than that of CO_2, which makes cationic zeolites an useful choice for CO_2/CH_4 separations. Table 4.7 shows the CCFF parameters for CH_4 in cationic zeolites. A comparison of experimental and simulated adsorption isotherms for CH_4 is shown in Figure 4.8. The agreement between experiments and simulations is especially good for NaX and Na-LTA(Si/Al=2). The agreement is typically best at low pressures.

Table 4.7 - The fitted Lennard-Jones parameters for CH_4 – Al and CH_4 – M^+ (M = Li, Na, K, Rb, Cs) interactions are shown. The interaction parameters with Si and O_z can be found in **Appendix E.**

Cross-Species	ε (K)	σ (Å)
C_ch4 – Al	76.369	3.252
C_ch4 – Li	433.72	2.168
C_ch4 – Na	158.30	2.731
C_ch4 – K	72.432	3.277
C_ch4 – Rb	124.19	3.386
C_ch4 – Cs	119.00	3.530
H_ch4 – Al	55.646	2.777
H_ch4 – Li	461.23	1.739
H_ch4 – Na	140.70	2.256
H_ch4 – K	55.705	2.774
H_ch4 – Rb	90.824	2.890
H_ch4 – Cs	82.385	3.040

Species	Charge (e)
C_ch4	-0.240
H_ch4	0.060

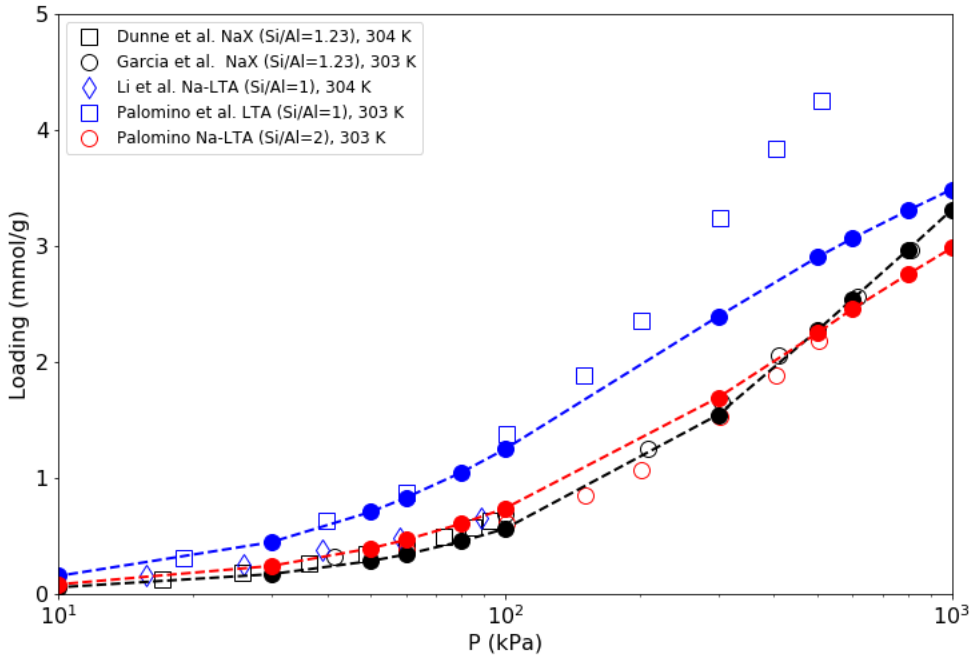

Figure 4.8 – A comparison between simulated (filled symbols) and experimental (open symbols) CH_4 adsorption isotherms is shown for NaX(Si/Al=1.23)[73, 79](black), Na-LTA(Si/Al=1)[3, 80](blue), and Na-LTA(Si/Al=2)[3](red).

In the case of Na-LTA(Si/Al=1), we see good agreement with the data from Palomino et al.[3] at lower pressures, but the FF results underpredict this set of experimental data at pressures above 100 kPa. Additionally, our simulations overpredict the experimental data from Li et al. at low pressures. Overall, the adsorption isotherm predictions are within the range of experimental variability for Na-LTA(Si/Al=1). This indicates that our methods for force field fitting can be applied to CH_4.

4.5 Force Field Predictions for Diffusion

In order to test our force field's performance for diffusion, we performed molecular dynamics simulations on CO_2 in Na-LTA (Si/Al=1), also known as zeolite 4A. This zeolite was selected because of the extra-framework Na that sit in the 8MR and block the diffusion path. Like the "trapdoor" zeolites mentioned earlier, adsorbates must first displace the 8MR Na in order to diffuse within the material. To determine if the cation motion away from the 8MR in Na-LTA(Si/Al=1) is induced by CO_2, we ran MD simulations at 4 different loadings of CO_2. A comparison between experimental and simulated self-diffusivities and activation energies is shown in Figure 4.9 for 4 different loadings of CO_2. We note that the three different experiments reported diffusivities that varied by orders of magnitude although they each showed similar activation energies. Although the values for the CO_2 diffusivity are not in agreement with experiments or even between experiments, all diffusivities have the similar dependence on 1/T, resulting in similar values of activation energies in Figure 4.9(b). This indicates that we our force field is likely predicting the correct diffusion mechanism.

When viewing snapshots from the molecular dynamics simulations, we observed the motion of Na from some of the 8MR sites to unoccupied adjacent 4MR sites, which allowed CO_2 to move between cages. However, cations did not always return to the 8MR afterwards. Also, the percentage of open 8MR varied with temperature but not loading. This is reflected in Figure 4.9(a), where the diffusivity has a strong dependence on 1/T but almost no dependence on loading. Additionally, the activation energy's dependence on loading was weak. These two observations indicate that Na-LTA(Si/Al=1) does not follow the "trapdoor" diffusion mechanism proposed for Cs-CHA, K-CHA and Cs-RHO[2, 5, 9], in

which CO_2 facilitates the motion of cations away from the 8MR. This is consistent with the experimental data for Na-LTA(Si/Al=1) in Figure 4.8, which shows that CH_4 can enter the structure, unlike in the "trapdoor" zeolites studied by Shang et al.[25]

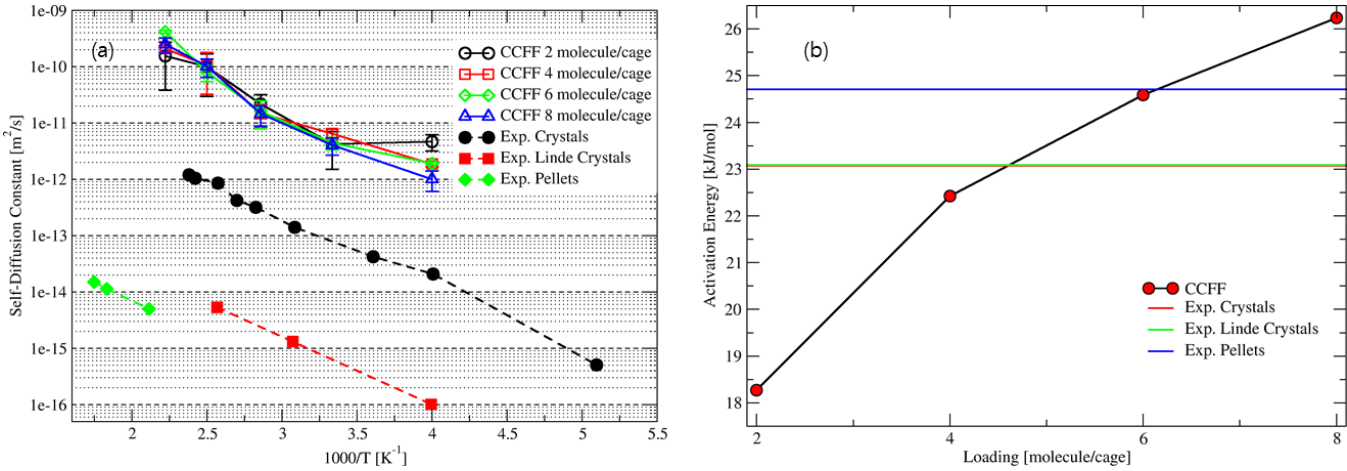

Figure 4.9 – A comparison between experimental (filled symbols) and simulated (open symbols) values for CO_2 self-diffusivity are shown in (a). The experimental data was taken from Yucel and Ruthven[81, 82]. The activation energy, shown in (b), of CO_2 diffusivity in Na-LTA(Si/Al=1) as a function of loading. The horizontal lines are the activation energies based on three sets of experimental data[82].

4.6 Conclusions

It is difficult to fit a transferrable force field for cationic zeolites because of the high degree of variability in zeolite topology, Si/Al ratio, aluminum distribution and cation composition. Force fields fit to experimental data in cationic zeolites are often not transferrable to systems that differ in topology and composition from their training set of experimental data. Additionally, the distribution of cations is not always known for a given zeolite topology and Si/Al ratio and cation composition. These factors can cause experimentally-derived FFs to perform poorly when screening adsorbents for separations applications.

In this work, we fit a force field to highly accurate DFT/CC energies for CO_2, N_2, O_2 and CH_4 in cationic zeolites that are exchanged with Li, Na, K, Rb and Cs. In order to describe the motion of cations in the presence of adsorbates, we also fit a FF to describe cation-framework interactions. In the training sets for both FFs, we forced the adsorbate or cation to explore both energetically favorable and unfavorable states. Adsorption isotherms predicted by this CCFF were shown to agree with almost 20 sets of experimental adsorption isotherms spanning 4 distinct zeolite topologies, 5 different cation types, and 4 different adsorbates. The adsorbate-adsorbent interactions ranged from CO_2, which exhibited strong interactions with cations to O_2, which had very weak interactions with cations. This indicates that our CCFF fitting methodology is transferable across adsorbates, as well as zeolite composition and topology. To the best of our knowledge, many of these adsorbate-adsorbent pairs, especially for Li, Rb and Cs-exchanged zeolites, have not been previously described by first-principles based FFs or experimentally-derived FFs.

Self-diffusivities for CO_2 in Na-LTA(Si/Al=1) were also computed and shown to have the same temperature dependence as experimentally-measured CO_2 self-diffusivities in that same system. This indicates that our CCFF could be used to examine diffusion processes even when cations block the diffusion path.

Our results indicate that our CCFF method can be used to accurately predict adsorption properties over a variety of zeolite topologies and compositions for use in separations applications. These methods have yielded new sets of FF parameters for systems that have not been extensively studied by FF methods, such as Li-exchanged zeolites, which are relevant to N_2/O_2 separations and Cs-exchanged zeolites which show

promising selectivity for CO_2 over N_2 and CH_4. This opens up the space to screen more adsorbates and compositions of cationic zeolites for separations applications.

4.7 Chapter 4 References

1. Baerlocher, C.; McCusker, L. B.; Olson, D. H., *Atlas of zeolite framework types*. Elsevier: 2007.

2. Lozinska, M. M.; Mowat, J. P.; Wright, P. A.; Thompson, S. P.; Jorda, J. L.; Palomino, M.; Valencia, S.; Rey, F., Cation gating and relocation during the highly selective "trapdoor" adsorption of CO_2 on univalent cation forms of zeolite RHO. *Chemistry of Materials* **2014,** *26* (6), 2052-2061.

3. Palomino, M.; Corma, A.; Rey, F.; Valencia, S., New Insights on CO_2− Methane separation using LTA zeolites with different Si/Al ratios and a first comparison with MOFs. *Langmuir* **2010,** *26* (3), 1910-1917.

4. Remy, T.; Gobechiya, E.; Danaci, D.; Peter, S.; Xiao, P.; Van Tendeloo, L.; Couck, S.; Shang, J.; Kirschhock, C.; Singh, R., Biogas upgrading through kinetic separation of carbon dioxide and methane over Rb-and Cs-ZK-5 zeolites. *RSC Adv* **2014,** *4* (107), 62511-62524.

5. Shang, J.; Li, G.; Singh, R.; Gu, Q.; Nairn, K. M.; Bastow, T. J.; Medhekar, N.; Doherty, C. M.; Hill, A. J.; Liu, J. Z., Discriminative separation of gases by a "molecular trapdoor" mechanism in chabazite zeolites. *Journal of the American Chemical Society* **2012,** *134* (46), 19246-19253.

6. Shang, J.; Li, G.; Singh, R.; Xiao, P.; Liu, J. Z.; Webley, P. A., Determination of composition range for "molecular trapdoor" effect in chabazite zeolite. *The Journal of Physical Chemistry C* **2013,** *117* (24), 12841-12847.

7. Fang, H.; Kulkarni, A.; Kamakoti, P.; Awati, R.; Ravikovitch, P. I.; Sholl, D. S., Identification of high-CO_2-capacity cationic zeolites by accurate computational screening. *Chemistry of Materials* **2016,** *28* (11), 3887-3896.

8. Findley, J. M.; Ravikovitch, P. I.; Sholl, D. S., The effect of aluminum short-range ordering on carbon dioxide adsorption in zeolites. *The Journal of Physical Chemistry C* **2018,** *122* (23), 12332-12340.

9. Shang, J.; Li, G.; Gu, Q.; Singh, R.; Xiao, P.; Liu, J. Z.; Webley, P. A., Temperature controlled invertible selectivity for adsorption of N_2 and CH_4 by molecular trapdoor chabazites. *Chem Commun* **2014,** *50* (35), 4544-4546.

10. Coudert, F.-X.; Kohen, D., Molecular insight into CO_2 "trapdoor" adsorption in zeolite Na-RHO. *Chemistry of Materials* **2017,** *29* (7), 2724-2730.

11. Fang, H.; Awati, R.; Boulfelfel, S. E.; Ravikovitch, P. I.; Sholl, D. S., First-principles-derived force fields for CH_4 adsorption and diffusion in siliceous zeolites. *The Journal of Physical Chemistry C* **2018,** *122* (24), 12880-12891.

12. Fang, H.; Kamakoti, P.; Zang, J.; Cundy, S.; Paur, C.; Ravikovitch, P. I.; Sholl, D. S., Prediction of CO_2 adsorption properties in zeolites using force fields derived from periodic dispersion-corrected DFT calculations. *The Journal of Physical Chemistry C* **2012,** *116* (19), 10692-10701.

13. Nachtigall, P.; Delgado, M. R.; Nachtigallova, D.; Areán, C. O., The nature of cationic adsorption sites in alkaline zeolites—single, dual and multiple cation sites. *Physical Chemistry Chemical Physics* **2012,** *14* (5), 1552-1569.

14. Pulido, A.; Delgado, M.; Bludský, O.; Rubeš, M.; Nachtigall, P.; Areán, C. O., Combined DFT/CC and IR spectroscopic studies on carbon dioxide adsorption on the zeolite H-FER. *Energy & Environmental Science* **2009,** *2* (11), 1187-1195.

15. Shang, J.; Li, G.; Webley, P. A.; Liu, J. Z., A density functional theory study for the adsorption of various gases on a caesium-exchanged trapdoor chabazite. *Computational Materials Science* **2016,** *122*, 307-313.

16. Fang, H.; Demir, H.; Kamakoti, P.; Sholl, D. S., Recent developments in first-principles force fields for molecules in nanoporous materials. *Journal of Materials Chemistry A* **2014,** *2* (2), 274-291.

17. Fuchs, A. H.; Cheetham, A. K., Adsorption of guest molecules in zeolitic materials: computational aspects. ACS Publications: 2001.

18. Sholl, D. S., Understanding macroscopic diffusion of adsorbed molecules in crystalline nanoporous materials via atomistic simulations. *Accounts of chemical research* **2006,** *39* (6), 403-411.

19. Smit, B.; Maesen, T. L., Molecular simulations of zeolites: adsorption, diffusion, and shape selectivity. *Chemical reviews* **2008,** *108* (10), 4125-4184.

20. Keskin, S.; Liu, J.; Rankin, R. B.; Johnson, J. K.; Sholl, D. S., Progress, opportunities, and challenges for applying atomically detailed modeling to molecular adsorption and

transport in metal− organic framework materials. *Industrial & Engineering Chemistry Research* **2009,** *48* (5), 2355-2371.

21. Krishna, R., Diffusion in porous crystalline materials. *Chemical Society Reviews* **2012,** *41* (8), 3099-3118.

22. Fang, H.; Findley, J.; Muraro, G.; Ravikovitch, P. I.; Sholl, D. S., A Strong Test of Atomically-detailed Models of Molecular Adsorption in Zeolites Using Multi-laboratory Experimental Data for CO_2 Adsorption in Ammonium ZSM-5. *The Journal of Physical Chemistry Letters* **2019**.

23. Fang, H.; Kamakoti, P.; Ravikovitch, P. I.; Aronson, M.; Paur, C.; Sholl, D. S., First principles derived, transferable force fields for CO_2 adsorption in Na-exchanged cationic zeolites. *Physical Chemistry Chemical Physics* **2013,** *15* (31), 12882-12894.

24. Zang, J.; Nair, S.; Sholl, D. S., Prediction of water adsorption in copper-based metal–organic frameworks using force fields derived from dispersion-corrected DFT calculations. *The Journal of Physical Chemistry C* **2013,** *117* (15), 7519-7525.

25. Dzubak, A. L.; Lin, L.-C.; Kim, J.; Swisher, J. A.; Poloni, R.; Maximoff, S. N.; Smit, B.; Gagliardi, L., Ab initio carbon capture in open-site metal–organic frameworks. *Nature chemistry* **2012,** *4* (10), 810.

26. Han, S. S.; Choi, S.-H.; Goddard III, W. A., Zeolitic imidazolate frameworks as H_2 adsorbents: Ab initio based grand canonical monte carlo simulation. *The Journal of Physical Chemistry C* **2010,** *114* (27), 12039-12047.

27. Lin, L.-C.; Lee, K.; Gagliardi, L.; Neaton, J. B.; Smit, B., Force-field development from electronic structure calculations with periodic boundary conditions: applications to gaseous adsorption and transport in metal–organic frameworks. *Journal of chemical theory and computation* **2014,** *10* (4), 1477-1488.

28. Jaramillo, E.; Auerbach, S. M., New force field for Na cations in faujasite-type zeolites. *The Journal of Physical Chemistry B* **1999,** *103* (44), 9589-9594.

29. Harris, J. G.; Yung, K. H., Carbon dioxide's liquid-vapor coexistence curve and critical properties as predicted by a simple molecular model. *The Journal of Physical Chemistry* **1995,** *99* (31), 12021-12024.

30. Makrodimitris, K.; Papadopoulos, G. K.; Theodorou, D. N., Prediction of permeation properties of CO_2 and N_2 through silicalite via molecular simulations. *The Journal of Physical Chemistry B* **2001,** *105* (4), 777-788.

31. Murthy, C.; Singer, K.; Klein, M.; McDonald, I., Pairwise additive effective potentials for nitrogen. *Molecular Physics* **1980,** *41* (6), 1387-1399.

32. Zhang, L.; Siepmann, J. I., Direct calculation of Henry's law constants from Gibbs ensemble Monte Carlo simulations: nitrogen, oxygen, carbon dioxide and methane in ethanol. *Theoretical Chemistry Accounts* **2006,** *115* (5), 391-397.

33. Jorgensen, W. L.; Maxwell, D. S.; Tirado-Rives, J., Development and testing of the OPLS all-atom force field on conformational energetics and properties of organic liquids. *Journal of the American Chemical Society* **1996,** *118* (45), 11225-11236.

34. Smith, L. J.; Eckert, H.; Cheetham, A. K., Site preferences in the mixed cation zeolite, Li, Na-chabazite: a combined solid-state NMR and neutron diffraction study. *Journal of the American Chemical Society* **2000,** *122* (8), 1700-1708.

35. Feuerstein, M.; Engelhardt, G.; McDaniel, P.; MacDougall, J.; Gaffney, T., Solid-state nuclear magnetic resonance investigation of cation siting in LiNaLSX zeolites. *Microporous and mesoporous materials* **1998,** *26* (1-3), 27-35.

36. Pluth, J. J.; Smith, J. V., Accurate redetermination of crystal structure of dehydrated zeolite A. Absence of near zero coordination of sodium. Refinement of silicon, aluminum-ordered superstructure. *Journal of the American Chemical Society* **1980,** *102* (14), 4704-4708.

37. Olson, D. H., The crystal structure of dehydrated NaX. *Zeolites* **1995,** *15* (5), 439-443.

38. Pham, T. D.; Hudson, M. R.; Brown, C. M.; Lobo, R. F., On the Structure–Property Relationships of Cation-Exchanged ZK-5 Zeolites for CO_2 Adsorption. *ChemSusChem* **2017,** *10* (5), 946-957.

39. Ikeda, T.; Kodaira, T.; Oh, T.; Nisawa, A., K+ ion distribution in zeolite ZK-4's with various Si/Al ratios and the contribution of K+ ions to K cluster formation. *Microporous and mesoporous materials* **2003,** *57* (3), 249-261.

40. Mortier, W.; Bosmans, H.; Uytterhoeven, J., Location of univalent cations in synthetic zeolites of the Y and X type with varying silicon to aluminum ratio. II. Dehydrated potassium exchanged forms. *The Journal of Physical Chemistry* **1972,** *76* (5), 650-656.

41. Lee, S. H.; Kim, Y.; Seff, K., A cationic rubidium continuum in zeolite X. *The Journal of Physical Chemistry B* **2000,** *104* (47), 11162-11167.

42. Heo, N. H.; Seff, K., The reactions of cesium with dehydrated calcium zeolite A: Crystal structures of Cs_6Ca_3-A, $Cs_{11}Ca_{0.5}$-A· 0.5 Cs, and Cs_{12}-A· 0.5 Cs. *Zeolites* **1992,** *12* (7), 819-825.

43. Kresse, G.; Hafner, J., Ab-Initio Molecular-Dynamics Simulation of the Liquid-Metal Amorphous-Semiconductor Transition in Germanium. *Phys Rev B* **1994,** *49* (20), 14251-14269.

44. Kresse, G.; Furthmuller, J., Efficient iterative schemes for ab initio total-energy calculations using a plane-wave basis set. *Phys Rev B* **1996,** *54* (16), 11169-11186.

45. Kresse, G.; Joubert, D., From ultrasoft pseudopotentials to the projector augmented-wave method. *Phys Rev B* **1999,** *59* (3), 1758-1775.

46. Blochl, P. E., Projector Augmented-Wave Method. *Phys Rev B* **1994,** *50* (24), 17953-17979.

47. Grimme, S., Semiempirical GGA-type density functional constructed with a long-range dispersion correction. *J Comput Chem* **2006,** *27* (15), 1787-1799.

48. Manz, T. A.; Limas, N. G., Introducing DDEC6 atomic population analysis: part 1. Charge partitioning theory and methodology. *RSC Adv* **2016,** *6* (53), 47771-47801.

49. Limas, N. G.; Manz, T. A., Introducing DDEC6 atomic population analysis: part 2. Computed results for a wide range of periodic and nonperiodic materials. *RSC Adv* **2016,** *6* (51), 45727-45747.

50. Bludsky, O.; Rubes, M.; Soldan, P.; Nachtigall, P., Investigation of the benzene-dimer potential energy surface: DFT/CCSD(T) correction scheme. *J Chem Phys* **2008,** *128* (11), 114102.

51. Plimpton, S., Fast Parallel Algorithms for Short-Range Molecular-Dynamics. *J Comput Phys* **1995,** *117* (1), 1-19.

52. Frenkel, D.; Smit, B., Chapter 6 - Molecular Dynamics in Various Ensembles. In *Understanding Molecular Simulation (Second Edition)*, Academic Press: San Diego, 2002; pp 139-163.

53. Appendix E - Integration Schemes. In *Understanding Molecular Simulation (Second Edition)*, Academic Press: San Diego, 2002; pp 533-544.

54. Frenkel, D.; Smit, B., Chapter 12 - Long-Range Interactions. In *Understanding Molecular Simulation (Second Edition)*, Academic Press: San Diego, 2002; pp 291-320.

55. Fiorin, G.; Klein, M. L.; Henin, J., Using collective variables to drive molecular dynamics simulations. *Molecular Physics* **2013,** *111* (22-23), 3345-3362.

56. Pirngruber, G.; Raybaud, P.; Belmabkhout, Y.; Čejka, J.; Zukal, A., The role of the extra-framework cations in the adsorption of CO_2 on faujasite Y. *Physical Chemistry Chemical Physics* **2010,** *12* (41), 13534-13546.

57. Yang, X.; Epiepang, F. E.; Liu, Y.; Yang, R. T., Heats of adsorption on mixed-cation LiNa-LSX: Estimating SIII site occupancy by Li. *Chemical Engineering Science* **2018,** *178*, 194-198.

58. Dubbeldam, D.; Calero, S.; Ellis, D. E.; Snurr, R. Q., RASPA: molecular simulation software for adsorption and diffusion in flexible nanoporous materials. *Molecular Simulation* **2016,** *42* (2), 81-101.

59. Beauvais, C.; Guerrault, X.; Coudert, F.-X.; Boutin, A.; Fuchs, A. H., Distribution of sodium cations in faujasite-type zeolite: a canonical parallel tempering simulation study. *The Journal of Physical Chemistry B* **2004,** *108* (1), 399-404.

60. Agrawal, M.; Sholl, D. S., Effects of Intrinsic Flexibility on Adsorption Properties of Metal–Organic Frameworks at Dilute and Nondilute Loadings. *ACS applied materials & interfaces* **2019,** *11* (34), 31060-31068.

61. Witman, M.; Ling, S.; Jawahery, S.; Boyd, P. G.; Haranczyk, M.; Slater, B.; Smit, B., The influence of intrinsic framework flexibility on adsorption in nanoporous materials. *Journal of the American Chemical Society* **2017,** *139* (15), 5547-5557.

62. Vlugt, T. J.; Schenk, M., Influence of framework flexibility on the adsorption properties of hydrocarbons in the zeolite silicalite. *The Journal of Physical Chemistry B* **2002,** *106* (49), 12757-12763.

63. García-Sánchez, A.; Dubbeldam, D.; Calero, S., Modeling adsorption and self-diffusion of methane in LTA zeolites: the influence of framework flexibility. *The Journal of Physical Chemistry C* **2010,** *114* (35), 15068-15074.

64. Bates, S. P.; van Well, W. J.; van Santen, R. A.; Smit, B., Energetics of n-alkanes in zeolites: a configurational-bias Monte Carlo investigation into pore size dependence. *Journal of the American Chemical Society* **1996,** *118* (28), 6753-6759.

65. Keffer, D.; Gupta, V.; Kim, D.; Lenz, E.; Davis, H. T.; McCormick, A. V., A compendium of potential energy maps of zeolites and molecular sieves. *Journal of molecular graphics* **1996,** *14* (2), 108-116.

66. Song, S. H.; Kim, U. S.; Kim, Y.; Seff, K., Reaction of Na_{12}-A with rubidium vapor. Synthesis and crystal structure of fully dehydrated fully Rb^{+}-exchanged zeolite A containing $(Rb_6)^{4+}$ clusters. *The Journal of Physical Chemistry* **1992,** *96* (26), 10937-10941.

67. Jirak, Z.; Vratislav, S.; Bosáček, V., A neutron diffraction study of H, Na-Y zeolites. *Journal of Physics and Chemistry of Solids* **1980,** *41* (10), 1089-1095.

68. Van Dun, J.; Mortier, W.; Uytterhoeven, J., Influence of the temperature and the adsorption of benzene on the location of K, Ca and Sr in Y-type zeolites. *Zeolites* **1985,** *5* (4), 257-260.

69. Jale, S. R.; Bülow, M.; Fitch, F. R.; Perelman, N.; Shen, D., Monte Carlo simulation of sorption equilibria for nitrogen and oxygen on LiLSX zeolite. *The Journal of Physical Chemistry B* **2000,** *104* (22), 5272-5280.

70. Grimme, S., Semiempirical GGA-type density functional constructed with a long-range dispersion correction. *J Comput Chem* **2006,** *27* (15), 1787-1799.

71. Epiepang, F. E.; Li, J.; Liu, Y.; Yang, R. T., Low-pressure performance evaluation of CO_2, H_2O and CH_4 on Li-LSX as a superior adsorbent for air prepurification. *Chemical Engineering Science* **2016,** *147*, 100-108.

72. Ridha, F. N.; Webley, P. A., Anomalous Henry's law behavior of nitrogen and carbon dioxide adsorption on alkali-exchanged chabazite zeolites. *Separation and purification technology* **2009,** *67* (3), 336-343.

73. Dunne, J.; Rao, M.; Sircar, S.; Gorte, R.; Myers, A., Calorimetric heats of adsorption and adsorption isotherms. 2. O_2, N_2, Ar, CO_2, CH_4, C_2H_6, and SF_6 on NaX, H-ZSM-5, and Na-ZSM-5 zeolites. *Langmuir* **1996,** *12* (24), 5896-5904.

74. Walton, K. S.; Abney, M. B.; LeVan, M. D., CO_2 adsorption in Y and X zeolites modified by alkali metal cation exchange. *Microporous and Mesoporous Materials* **2006,** *91* (1-3), 78-84.

75. Khvoshchev, S. S.; Zverev, A. V., Calorimetric study of NH_3 and CO_2 adsorption on synthetic faujasites with Ca^{2+}, Mg^{2+}, and La^{3+} cations. *Journal of colloid and interface science* **1991,** *144* (2), 571-578.

76. Remy, T.; Peter, S. A.; Van Tendeloo, L.; Van der Perre, S.; Lorgouilloux, Y.; Kirschhock, C. E.; Baron, G. V.; Denayer, J. F., Adsorption and separation of CO_2 on KFI zeolites: effect of cation type and Si/Al ratio on equilibrium and kinetic properties. *Langmuir* **2013,** *29* (16), 4998-5012.

77. Pham, T. D.; Liu, Q.; Lobo, R. F., Carbon dioxide and nitrogen adsorption on cation-exchanged SSZ-13 zeolites. *Langmuir* **2013,** *29* (2), 832-839.

78. Wu, C.-W.; Kothare, M. V.; Sircar, S., Equilibrium adsorption isotherms of pure N_2 and O_2 and their binary mixtures on LiLSX zeolite: experimental data and thermodynamic analysis. *Industrial & Engineering Chemistry Research* **2014,** *53* (17), 7195-7201.

79. Garcia, E. J.; Pérez-Pellitero, J.; Pirngruber, G. D.; Jallut, C.; Palomino, M.; Rey, F.; Valencia, S., Tuning the adsorption properties of zeolites as adsorbents for CO_2 separation: best compromise between the working capacity and selectivity. *Industrial & Engineering Chemistry Research* **2014,** *53* (23), 9860-9874.

80. Li, Y.; Yi, H.; Tang, X.; Li, F.; Yuan, Q., Adsorption separation of CO_2/CH_4 gas mixture on the commercial zeolites at atmospheric pressure. *Chemical Engineering Journal* **2013,** *229*, 50-56.

81. Yucel, H.; Ruthven, D. M., Diffusion of CO2 in 4A and 5A zeolite crystals. *Journal of Colloid and Interface Science* **1980,** *74* (1), 186-195.

82. Ruthven, D. M., *Principles of adsorption and adsorption processes*. John Wiley & Sons: 1984.

83. Lemmon, E. W.; McLinden, M. O.; Friend, D. G., Thermophysical properties of fluid systems. In *NIST Chemistry WebBook, NIST Standard Reference Database Number 69*, Linstrom, P. J.; Mallard, W. G., Eds. National Institute of Standards and Technology: Gaithersburg, MD, 20899, 1998.

84. Hedin, N.; DeMartin, G. J.; Roth, W. J.; Strohmaier, K. G.; Reyes, S. C., PFG NMR self-diffusion of small hydrocarbons in high silica DDR, CHA and LTA structures. *Microporous and Mesoporous Materials* **2008,** *109* (1-3), 327-334.

85. Maghsoudi, H.; Soltanieh, M.; Bozorgzadeh, H.; Mohamadalizadeh, A., Adsorption isotherms and ideal selectivities of hydrogen sulfide and carbon dioxide over methane for the Si-CHA zeolite: comparison of carbon dioxide and methane adsorption with the all-silica DD3R zeolite. *Adsorption* **2013,** *19* (5), 1045-1053.

86. Pham, T. D.; Lobo, R. F., Adsorption equilibria of CO_2 and small hydrocarbons in AEI-, CHA-, STT-, and RRO-type siliceous zeolites. *Microporous and Mesoporous Materials* **2016,** *236*, 100-108.

CHAPTER 5. CONCLUSIONS AND SUGGESTIONS FOR FUTURE WORK

5.1 Thesis Summary

The objective of this thesis is to develop more transferable, accurate models and methods to predict adsorption and diffusion of small molecules in pure-silica and cationic zeolites. In Chapter 2, we focused on the description of aluminum distribution in cationic zeolites. We were able to quantify aluminum distribution using a short-range order parameter and systematically examine the effect of aluminum ordering on cation distribution and CO_2 adsorption isotherms. The significant dependence of cation distributions and CO_2 adsorption properties on aluminum distribution indicates that aluminum ordering should be considered when screening cationic zeolites for CO_2 adsorption and that CO_2 adsorption isotherms can be used to probe aluminum distribution.

Chapter 3 and Chapter 4 focus on improving the accuracy and transferability of force field methods that are used to examine adsorption and diffusion in pure-silica and cationic zeolites respectively. In Chapter 3, we demonstrated that fitting a first-principles-based FF to DFT/CC energies of both transition state configurations and energy minimum configurations can accurately predict both adsorption and diffusion data for a wide array of adsorbates in pure-silica zeolites.

Chapter 4 extends the CCFF methodology to zeolites exchanged with monovalent cations. This force field was able to accurately predict cation distributions and CO_2, N_2, O_2, and CH_4 adsorption isotherms for zeolites exchanged with Li, Na, K, Rb and Cs. We were also able to predict these quantities in mixed-cation zeolites. This transferability across zeolite topology and composition will allow for the accurate computational screening of zeolites exchanged with monovalent cations.

Overall, this work provides better, more transferable tools for studying both adsorption and diffusion in both pure-silica and cationic zeolites, which previous FF-based methods were limited to predicting adsorption for pure-silica, Na-exchanged and K-exchanged zeolites.

5.2 Suggestions for Future Work

5.2.1 Force Field for Cationic Zeolite Framework

When screening zeolites for separations applications, accurate predictions of the distribution of extra-framework cations are required because cation positions are important for predicting adsorption isotherms, heats of adsorption and diffusivities[1-4]. In order to predict the cation distribution, a detailed model of the framework is required[3]. Experimentally, the cation distribution and pore volume can change based on Si/Al ratio and the species of cations present[5-7]. When screening zeolites for separations applications, not every zeolite has experimentally-determined structural information available for every Si/Al ratio and cation species[2]. This adds a potential source of uncertainty in the screening process. Therefore, an efficient, transferable method for optimizing zeolite frameworks is

required. Structure optimization using DFT is too time-consuming for screening, so FF-based methods should be employed.

Boulfelfel et al.[8] fit a FF which can correctly predict the window size distribution in pure-silica 8 MR zeolites. However, there is no equivalent FF for cationic zeolites that are exchanged with Li, Rb or Cs. Employing a similar strategy to the work from Boulfelfel et al. [8] could result in a FF for predicting intraframework energetics. A better framework model could help improve predictions for cation distributions, adsorption and diffusion in cationic zeolites when a detailed description of the framework is unavailable.

5.2.2 CCFF for Divalent Cations and H_2O

Zeolites exchanged with divalent cations such as Ca, such as zeolite 5A[9] and Ca-CHA[10], have shown a strong affinity for CO_2, which allows them to be used for CO_2/CH_4 and CO_2/N_2 separations. However, Mg, Sr and Ba-exchanged zeolites have not been investigated in as much depth. In Chapter 4, we demonstrated that DFT/CC can accurately predict adsorbate-zeolite interaction energies for CO_2, CH_4, N_2, and O_2 in zeolites exchanged with monovalent cations. The natural next step would be to extend this procedure to divalent cations so that zeolites with divalent cations can be screened for separations as well.

Additionally, the effect of H_2O in Li-exchanged[11, 12] and Ca-exchanged[13, 14] zeolites cannot always be neglected. An accurate FF describing water-cation interactions could assist the study of the effect of H_2O on CO_2 and N_2 adsorption in these materials. Because we calculated CC-correction curves and CCFF parameters for H_2O in pure-silica zeolites

already, fitting a FF to DFT/CC energies for H_2O in cationic zeolites would be a natural extension of this work.

5.2.3 Trapdoor Zeolites for CO_2/CH_4 and CO_2/N_2 Separations

In cationic zeolites with 8 MR pores and large monovalent cations, it is possible to limit the diffusion of weakly-interacting adsorbates such as CH_4 and N_2 while allowing molecules like CO_2, which have stronger adsorbate-cation interactions, to enter the framework[15-20]. This results in high selectivities for CO_2 over N_2 and CH_4[12]. Some experimental work has been done in determining the maximum Si/Al ratio at which this "trapdoor" phenomena is observed[19]. A mechanism for cation motion upon CO_2 diffusion has been proposed based on DFT calculations[18, 20]. However, this mechanism only describes the energetics of the process and not the kinetics. Although diffusion is likely slow because of the presence of large cations blocking diffusion channels, one could gain a better understanding of diffusion in these materials using high temperature molecular dynamics or Transition-State Theory (TST). Using these methods, it would be possible better understand the diffusion for CO_2/N_2 and CO_2/CH_4 mixtures, the effect of Si/Al ratio, and the effect of aluminum distribution on these zeolites. However, neither of these simulations have been performed in "trapdoor" zeolites previously because of the lack of a reliable FF. In Chapter 4, we derived CCFF parameters for CO_2, N_2, O_2 and CH_4 in Li, Na, K, Rb, and Cs-exchanged zeolites and fit a FF to describe cation-framework interactions. The CCFF could be used to study these effects or discover new "trapdoor" zeolites using high temperature molecular dynamics simulations or TST-based methods.

5.2.4 Screening Zeolites for N_2/O_2 Separations

Li-LSX is a zeolite that is industrially used for N_2/O_2 separations because Li-N_2 interactions are much stronger than Li-O_2 interactions[4, 21, 22]. Ca-exchanged zeolites[23, 24] have also been investigated for N_2/O_2 separations. However, it is possible that different zeolite topologies, cation compositions and Si/Al ratios could result in improved performance in these separations.

Starting with Li-exchanged zeolites, the CCFF from Chapter 4 could be used to screen across all zeolite topologies, and several Si/Al ratios, with each Si/Al having 3 distinct aluminum distributions for N_2/O_2 selectivities and N_2 adsorption capacity. The same procedure could be applied to Ca-exchanged zeolites once a CCFF for N_2 and O_2 in Ca-exchanged zeolites is available.

5.2.5 Pure Silica Zeolites for Olefin/Paraffin Separations

Zeolites have been examined for industrial use in olefin/paraffin separations because of their small pore sizes[25-29]. Zeolites with 8 MR have been of specific interest because their small pore size can slow the diffusion of alkanes, while allowing alkenes to pass though. Recently, the zeolite ITQ-55 has shown a high selectivity for ethylene over ethane because its small, elliptical pores permit flat molecules like ethylene to enter while blocking ethane[25]. The CCFF for pure-silica zeolites derived in Chapter 3 demonstrates excellent agreement between experimental and simulated adsorption isotherms for ethylene in ITQ-55. This CCFF also accurately predicts adsorption and diffusion of ethane and methane in several pure-silica zeolites. Therefore, the CCFF should be able to

systematically screen the International Zeolite Association (IZA) database[30] for silica zeolites for olefin/paraffin separation.

5.2.6 Screening of Hypothetical Zeolites

In addition to the 245 experimentally synthesized zeolite topologies[30], millions of hypothetical zeolites have been constructed based on geometric and energetic criteria. For example, the database generated by Earl and Deem[31] contains approximately 4 million hypothetical zeolite structures. If one wanted to screen this database and allow each hypothetical topology to have 10 Si/Al ratios, each with 100 possible cation compositions, there would be more than 10^9 structures to consider, a library that is not feasible to directly screen even using FF-based methods. Machine learning models have recently been used to predict simulated adsorption properties in large libraries of MOFs[32-34]. One way to solve this problem without sacrificing the accuracy provided by our CCFF methods would involve parametrizing a similar machine-learning model to predict adsorption isotherms simulated using CCFF based on appropriate descriptors of the zeolite structures.

5.2.7 Zeolites with Alternative Compositions

This work focused on developing models to predict adsorption and diffusion in pure-silica and aluminosilicate zeolites. However, some zeolite structures have been synthesized with some T-sites occupied by Ge and P atoms[35]. One class of these materials, aluminophosphates (AlPOs), are composed of alternating aluminum and phosphorous-centered tetrahedral units[36, 37]. AlPOs have a charge-neutral framework, meaning that they don't need to be exchanged with extra-framework cations. This makes the frameworks hydrophobic[37]. Very few classical simulations in these materials have been published[38, 39].

Developing a CCFF for AlPOs and other non-aluminosilicate zeolites would allow for the screening of more zeolites for separations applications.

5.3 Chapter 5 References

1. Fang, H.; Kamakoti, P.; Ravikovitch, P. I.; Aronson, M.; Paur, C.; Sholl, D. S., First principles derived, transferable force fields for CO_2 adsorption in Na-exchanged cationic zeolites. *Physical Chemistry Chemical Physics* **2013,** *15* (31), 12882-12894.

2. Fang, H.; Kulkarni, A.; Kamakoti, P.; Awati, R.; Ravikovitch, P. I.; Sholl, D. S., Identification of high-CO_2-capacity cationic zeolites by accurate computational screening. *Chemistry of Materials* **2016,** *28* (11), 3887-3896.

3. Findley, J. M.; Ravikovitch, P. I.; Sholl, D. S., The effect of aluminum short-range ordering on carbon dioxide adsorption in zeolites. *The Journal of Physical Chemistry C* **2018,** *122* (23), 12332-12340.

4. Yang, X.; Epiepang, F. E.; Liu, Y.; Yang, R. T., Heats of adsorption on mixed-cation LiNa-LSX: Estimating SIII site occupancy by Li. *Chemical Engineering Science* **2018,** *178*, 194-198.

5. Dempsey, E.; Kuehl, G. H.; Olson, D. H., Variation of the lattice parameter with aluminum content in synthetic sodium faujasites. Evidence for ordering of the framework ions. *The Journal of Physical Chemistry* **1969,** *73* (2), 387-390.

6. Feuerstein, M.; Engelhardt, G.; McDaniel, P.; MacDougall, J.; Gaffney, T., Solid-state nuclear magnetic resonance investigation of cation siting in LiNaLSX zeolites. *Microporous and mesoporous materials* **1998,** *26* (1-3), 27-35.

7. Ikeda, T.; Kodaira, T.; Oh, T.; Nisawa, A., K+ ion distribution in zeolite ZK-4's with various Si/Al ratios and the contribution of K+ ions to K cluster formation. *Microporous and mesoporous materials* **2003,** *57* (3), 249-261.

8. Boulfelfel, S. E.; Ravikovitch, P. I.; Koziol, L.; Sholl, D. S., Improved Hill-Sauer Force Field for Accurate Description of Pores in 8-Ring Zeolites. *J Phys Chem C* **2016,** *120* (26), 14140-14148.

9. Mofarahi, M.; Gholipour, F., Gas adsorption separation of CO_2/CH_4 system using zeolite 5A. *Microporous and Mesoporous Materials* **2014,** *200*, 1-10.

10. Yang, J.; Zhao, Q.; Xu, H.; Li, L.; Dong, J.; Li, J., Adsorption of CO_2, CH_4, and N_2 on gas diameter grade ion-exchange small pore zeolites. *Journal of Chemical & Engineering Data* **2012,** *57* (12), 3701-3709.

11. Hutson, N. D.; Zajic, S. C.; Yang, R. T., Influence of Residual Water on the Adsorption of Atmospheric Gases in Li− X Zeolite: Experiment and Simulation. *Industrial & Engineering Chemistry Research* **2000,** *39* (6), 1775-1780.

12. Fan, M.; Panezai, H.; Sun, J.; Bai, S.; Wu, X., Thermal and kinetic performance of water desorption for N_2 adsorption in Li-LSX zeolite. *The Journal of Physical Chemistry C* **2014,** *118* (41), 23761-23767.

13. Higgins, F. M.; de Leeuw, N. H.; Parker, S. C., Modelling the effect of water on cation exchange in zeolite A. *Journal of Materials Chemistry* **2002,** *12* (1), 124-131.

14. Choudary, V. N.; Jasra, R. V.; Bhat, T. S., Adsorption of nitrogen-oxygen mixture in NaCaA zeolites by elution chromatography. *Industrial & engineering chemistry research* **1993,** *32* (3), 548-552.

15. Lozinska, M. M.; Mangano, E.; Mowat, J. P. S.; Shepherd, A. M.; Howe, R. F.; Thompson, S. P.; Parker, J. E.; Brandani, S.; Wright, P. A., Understanding Carbon Dioxide Adsorption on Univalent Cation Forms of the Flexible Zeolite RHO at Conditions Relevant to Carbon Capture from Flue Gases. *Journal of the American Chemical Society* **2012,** *134* (42), 17628-17642.

16. Lozinska, M. M.; Mowat, J. P.; Wright, P. A.; Thompson, S. P.; Jorda, J. L.; Palomino, M.; Valencia, S.; Rey, F., Cation gating and relocation during the highly selective "trapdoor" adsorption of CO_2 on univalent cation forms of zeolite RHO. *Chemistry of Materials* **2014,** *26* (6), 2052-2061.

17. Shang, J.; Li, G.; Gu, Q.; Singh, R.; Xiao, P.; Liu, J. Z.; Webley, P. A., Temperature controlled invertible selectivity for adsorption of N_2 and CH_4 by molecular trapdoor chabazites. *Chem Commun* **2014,** *50* (35), 4544-4546.

18. Shang, J.; Li, G.; Singh, R.; Gu, Q.; Nairn, K. M.; Bastow, T. J.; Medhekar, N.; Doherty, C. M.; Hill, A. J.; Liu, J. Z., Discriminative separation of gases by a "molecular trapdoor" mechanism in chabazite zeolites. *Journal of the American Chemical Society* **2012,** *134* (46), 19246-19253.

19. Shang, J.; Li, G.; Singh, R.; Xiao, P.; Liu, J. Z.; Webley, P. A., Determination of composition range for "molecular trapdoor" effect in chabazite zeolite. *The Journal of Physical Chemistry C* **2013,** *117* (24), 12841-12847.

20. Shang, J.; Li, G.; Webley, P. A.; Liu, J. Z., A density functional theory study for the adsorption of various gases on a caesium-exchanged trapdoor chabazite. *Computational Materials Science* **2016,** *122*, 307-313.

21. Jale, S. R.; Bülow, M.; Fitch, F. R.; Perelman, N.; Shen, D., Monte Carlo simulation of sorption equilibria for nitrogen and oxygen on LiLSX zeolite. *The Journal of Physical Chemistry B* **2000,** *104* (22), 5272-5280.

22. Wu, C.-W.; Kothare, M. V.; Sircar, S., Equilibrium adsorption isotherms of pure N_2 and O_2 and their binary mixtures on LiLSX zeolite: experimental data and thermodynamic analysis. *Industrial & Engineering Chemistry Research* **2014,** *53* (17), 7195-7201.

23. Bajusz, I.-G.; Goodwin, J. G.; Galloway, D.; Greenlay, N., Effect of Ca^{2+} Exchange on Adsorption of N_2-O_2 Mixtures by NaCaX Zeolite. *Langmuir* **1998,** *14* (10), 2876-2883.

24. Mellot, C.; Lignieres, J., Monte Carlo simulations of N_2 and O_2 adsorption in silicalite and CaLSX zeolites. *Molecular Simulation* **1997,** *18* (6), 349-365.

25. Bereciartua, P. J.; Cantín, Á.; Corma, A.; Jordá, J. L.; Palomino, M.; Rey, F.; Valencia, S.; Corcoran, E. W.; Kortunov, P.; Ravikovitch, P. I., Control of zeolite framework flexibility and pore topology for separation of ethane and ethylene. *Science* **2017,** *358* (6366), 1068-1071.

26. Hedin, N.; DeMartin, G. J.; Roth, W. J.; Strohmaier, K. G.; Reyes, S. C., PFG NMR self-diffusion of small hydrocarbons in high silica DDR, CHA and LTA structures. *Microporous and Mesoporous Materials* **2008,** *109* (1-3), 327-334.

27. Vidoni, A.; Ruthven, D. M., Diffusion of C_2H_6 and C_2H_4 in DDR Zeolite. *Industrial & engineering chemistry research* **2012,** *51* (3), 1383-1390.

28. Zhu, W.; Kapteijn, F.; Moulijn, J., Shape selectivity in the adsorption of propane/propene on the all-silica DD3R. *Chem Commun* **1999,** (24), 2453-2454.

29. Olson, D. H.; Yang, X.; Camblor, M. A., ITQ-12: a zeolite having temperature dependent adsorption selectivity and potential for propene separation. *The Journal of Physical Chemistry B* **2004,** *108* (30), 11044-11048.

30. Baerlocher, C.; McCusker, L. B.; Olson, D. H., *Atlas of zeolite framework types*. Elsevier: 2007.

31. Earl, D. J.; Deem, M. W., Toward a database of hypothetical zeolite structures. *Industrial & engineering chemistry research* **2006,** *45* (16), 5449-5454.

32. Gharagheizi, F.; Tang, D.; Sholl, D. S., Selecting Adsorbents to Separate Diverse Near-Azeotropic Chemicals. *The Journal of Physical Chemistry C* **2020,** *124* (6), 3664-3670.

33. Anderson, R.; Biong, A.; Gómez-Gualdrón, D. A., Adsorption Isotherm Predictions for Multiple Molecules in MOFs Using the Same Deep Learning Model. *Journal of Chemical Theory and Computation* **2020,** *16* (2), 1271-1283.

34. Liang, H.; Yang, W.; Peng, F.; Liu, Z.; Liu, J.; Qiao, Z., Combining large-scale screening and machine learning to predict the metal-organic frameworks for organosulfurs removal from high-sour natural gas. *APL Materials* **2019,** *7* (9), 091101.

35. Christensen, A. N.; Jensen, T. R.; Norby, P.; Hanson, J. C., In situ synchrotron X-ray powder diffraction studies of crystallization of microporous aluminophosphates and Me2+-substituted aluminophosphates. *Chemistry of materials* **1998,** *10* (6), 1688-1693.

36. Predescu, L.; Tezel, F.; Chopra, S., Adsorption of nitrogen, methane, carbon monoxide, and their binary mixtures on aluminophosphate molecular sieves. *Adsorption* **1997,** *3* (1), 7-25.

37. Liu, Q.; Cheung, N. C. O.; Garcia-Bennett, A. E.; Hedin, N., Aluminophosphates for CO_2 separation. *ChemSusChem* **2011,** *4* (1), 91-97.

38. Awati, R. V. Development of accurate computational methods for simulations of adsorption and diffusion in zeolites. Doctoral Dissertation, Georgia Institute of Technology, Atlanta, GA, 30332, 2016.

39. Maris, T.; Vlugt, T. J.; Smit, B., Simulation of Alkane Adsorption in the Aluminophosphate Molecular Sieve AlPO4− 5. *The Journal of Physical Chemistry B* **1998,** *102* (37), 7183-7189.

APPENDIX A. SUPPORTING INFORMATION FOR THE EFFECT OF ALUMINUM SHORT-RANGE ORDERING ON CARBON DIOXIDE ADSORPTION IN ZEOLITES

A.1 Warren-Cowley Parameters of Screened Topologies

The short-range order of framework Al was quantified using the Warren-Cowley parameter

$$\alpha_j = 1 - \frac{P_j^{Al(Si)}}{x_{Si}} \tag{A.1}$$

here $P_j^{Al(Si)}$ is the probability of finding Si as the j-th nearest neighbor of Al and x_{Si} is the mole fraction of Si in the framework. Table A.1 lists the Warren-Cowley parameters for the sparse, random and clustered distributions for each topology in Figure 2.3 for Si/Al=11, Si/Al=5 and Si/Al=2.

Table A.1 - The Warren-Cowley parameters for the zeolites studied in Figure 2.3. They are listed by topology and Si/Al ratio. Differences are a result of different connectivity between structures.

Topology	**α-Sparse (Si/Al=11)**	**α-Random (Si/Al=11)**	**α-Clustered (Si/Al=11)**
LTA	-0.09	0	0.39
KFI	-0.09	0	0.39
RHO	-0.09	0	0.39
CHA	-0.09	0	0.31
FAU	-0.09	0	0.42
FER	-0.09	0	0.28
MOR	-0.09	0	0.28
Topology	**α-Sparse (Si/Al=5)**	**α-Random (Si/Al=5)**	**α-Clustered (Si/Al=5)**
LTA	-0.16	0	0.58
KFI	-0.18	0	0.56
RHO	-0.15	0	0.55
CHA	-0.13	0	0.47
FAU	-0.13	0	0.56
FER	-0.11	0	0.31
MOR	-0.11	0	0.31
Topology	**α-Sparse (Si/Al=2)**	**α-Random (Si/Al=2)**	**α-Clustered (Si/Al=2)**
LTA	0.17	0.26	0.78
KFI	0.18	0.25	0.7
RHO	0.17	0.25	0.7
CHA	0.2	0.25	0.65
FAU	0.19	0.28	0.7
FER	0.15	0.21	0.38
MOR	0.15	0.21	0.38

A.2 GCMC Calculation Details

Grand Canonical Monte Carlo simulations were performed using the RASPA package[1]. The CO_2, Na and K interaction potentials were taken from the CCFF force field from Fang et al.[2, 3]. Electrostatic energies were calculated using the Ewald summation with a precision of 10^{-6}. And dispersion interactions were calculated with a cutoff of 12.0 Å

using periodic boundary conditions. CO_2-CO_2 interactions were described by the TrAPPE force field.

Adsorption isotherms for CO_2 were computed using Grand Canonical (constant μVT) Monte Carlo methods. The chemical potential is determined from the fugacity, and the Peng-Robinson equation of state was used to compute fugacity coefficients. Isosteric heats of adsorption, Q_{st} , which is defined as the difference in the partial molar enthalpy of adsorption between the gas phase and adsorbed phase were obtained from GCMC simulations using[4]

$$Q_{st} = RT - \frac{< NV > - < N >< V >}{< N^2 > - < N >^2} \tag{A.2}$$

where R is the gas constant, T is the temperature, N is the number of molecules, V is the sum of interactions of all adsorbed molecules with both the zeolite and one another and < > denotes the ensemble average[5].

GCMC simulations were run with 5×10^4 initialization cycles and thermodynamic properties were sampled after 10^5 cycles. The standard deviations in calculated loadings, computed using block averages, were typically less than 1% of the loadings and always less than 5%.

Table A.2 - CCFF parameters for CO_2 in K-exchanged and Na-exchanged cationic zeolites. O_z refers to framework oxygen, whereas O simply refers to the oxygen in CO_2. O_z has different charges depending on whether it is connected to Al.

Cross Species	ε/k_B (K)	σ (Å)	Charge (e)
Si-C	49.75	3.620	Si (2.21)
Si-O	38.90	3.494	O_z^{Si} (-1.105)
Al-C	32.21	3.366	O_z^{Al} (-1.32)
Al-O	25.32	3.246	Al (2.08)
O_z-C	29.12	3.193	Na (0.99)
O_z-O	23.43	3.067	K (0.99)
Na-C	66.78	2.827	C (0.6512)
Na-O	54.76	2.707	O (-0.3256)
K-C	60.60	3.232	
K-O	48.19	3.111	

A.3 Cation-Framework Interactions

The parameters for extra-framework cations were taken from the Supporting Information section in Fang et al.[3] The interactions between Na^+ and K^+ and framework oxygen were described using the Buckingham potential.

$$E_{Buck}(R_{ij}) = A_{ij}e^{-\frac{R_{ij}}{B_{ij}}} - \frac{C_{ij}}{R_{ij}^6} \tag{A.3}$$

where A_{ij}, B_{ij} and C_{ij} are the cross-species Buckingham parameters for species i and j. The parameters are listed in Table A.3.

Table A.3 - Buckingham for K- and Na- framework interactions

Cross Species	A (eV)	B (Å)	C (eV)
K-O_Z	5258.3	0.2916	193.7
Na-O_Z	3261.6	0.2597	45.4

A.4 The Effect of Framework Choice on Sensitivity

The atomic coordinates from pure silica frameworks in the IZA database were chosen as a method to compare adsorption isotherm sensitivity across topologies. This method neglects differences in atomic coordinates at different Si/Al ratios. To examine the effects of different framework models on the CO_2 adsorption sensitivity, CO_2 adsorption isotherms in Na-LTA were simulated using the LTA-4A XRD framework from Pluth and Smith[6] with the IZA pure Si framework[7], which are compared in Figure A.1. The adsorption sensitivity is generally higher for the 4A framework, which is likely to be more accurate and lower Si/Al ratio, whereas the Si framework is likely to be more accurate at high Si/Al.

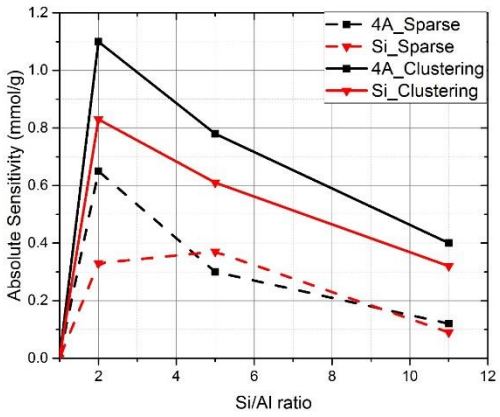

Figure A.1 - Adsorption sensitivity to a clustered Al distribution (solid) and a sparse (dashed) Al distribution for Na-LTA using the experimental 4A coordinates (black) and the IZA silica framework (red).

A.5 Additional Comparisons with Experiments

To validate the adsorption isotherms, more simulated adsorption isotherms were compared with experimental data for Na-FAU (Si/Al=5.1) in Figure A.2(a) and Na-LTA (Si/Al=2) in Figure A.2(b). Both materials have unknown distributions of framework Al.

When obtaining adsorption isotherms for faujisites, aluminum distributions are also approximated as random[8]. When the simulated CO_2 adsorption isotherms for Na-FAU with Si/Al = 5.1 were compared to the experimental results by Harlick and Tezel[9], the random distribution of was in adequate agreement with the experimental results.

The CO_2 adsorption isotherms for Na-LTA with Si/Al = 2 was shown in Figure 2.1. However, more orderings were tested to determine whether α=0.26 indeed provided the best fit for the experimental data. When compared to experimental results, Na-LTA (Si/Al=2) the CO_2 adsorption isotherm corresponding to α=0.26 (displayed in red squares) still provides the best prediction of the experimental results from Palomino et al.[10].

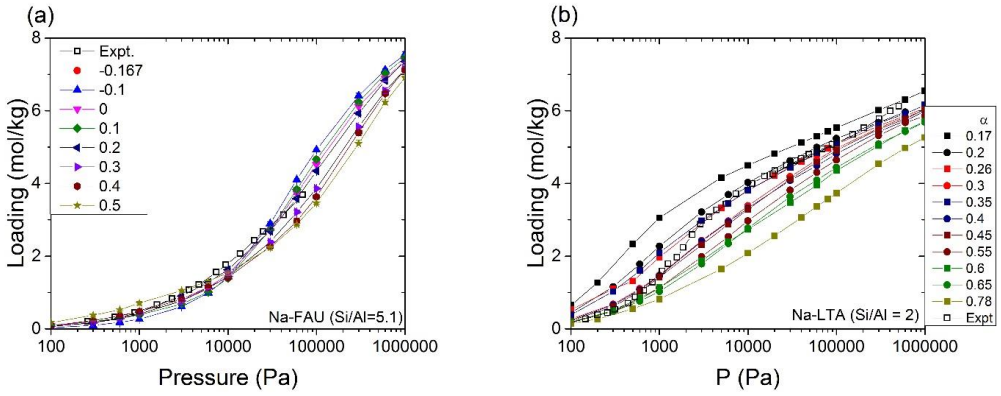

Figure A.2 - CO_2 adsorption isotherms (T=300K) for Na-FAU (Si/Al=5.1) (a) Na-LTA (Si/Al=2) (b). The sparse distribution of Al is shown in red, random in green and clustered in blue. Experimental data is taken from Harlick et al.[9] for FAU and Palomino et al. for LTA[10].

A.6 Appendix A References

1. Dubbeldam, D.; Calero, S.; Ellis, D. E.; Snurr, R. Q., RASPA: molecular simulation software for adsorption and diffusion in flexible nanoporous materials. *Molecular Simulation* **2016,** *42* (2), 81-101.

2. Fang, H.; Kamakoti, P.; Ravikovitch, P. I.; Aronson, M.; Paur, C.; Sholl, D. S., First principles derived, transferable force fields for CO_2 adsorption in Na-exchanged cationic zeolites. *Phys Chem Chem Phys* **2013,** *15* (31), 12882-94.

3. Fang, H.; Kulkarni, A.; Kamakoti, P.; Awati, R.; Ravikovitch, P. I.; Sholl, D. S., Identification of High-CO_2-Capacity Cationic Zeolites by Accurate Computational Screening. *Chemistry of Materials* **2016,** *28* (11), 3887-3896.

4. Snurr, R. Q.; Bell, A. T.; Theodorou, D. N., Prediction of adsorption of aromatic hydrocarbons in silicalite from grand canonical Monte Carlo simulations with biased insertions. *The Journal of Physical Chemistry* **1993,** *97* (51), 13742-13752.

5. Burtch, N. C.; Jasuja, H.; Dubbeldam, D.; Walton, K. S., Molecular-level insight into unusual low pressure CO_2 affinity in pillared metal–organic frameworks. *Journal of the American Chemical Society* **2013,** *135* (19), 7172-7180.

6. Pluth, J. J.; Smith, J. V., Accurate redetermination of crystal structure of dehydrated zeolite A. Absence of near zero coordination of sodium. Refinement of silicon, aluminum-ordered superstructure. *Journal of the American Chemical Society* **1980,** *102* (14), 4704-4708.

7. Baerlocher, C.; McCusker, L. B., Database of Zeolite Structures.

8. Liu, B.; García-Pérez, E.; Dubbeldam, D.; Smit, B.; Calero, S., Understanding Aluminum Location and Non-framework Ions Effects on Alkane Adsorption in Aluminosilicates: A Molecular Simulation Study. *The Journal of Physical Chemistry C* **2007,** *111* (28), 10419-10426.

9. Harlick, P. J.; Tezel, F. H., An experimental adsorbent screening study for CO 2 removal from N 2. *Microporous and Mesoporous Materials* **2004,** *76* (1), 71-79.

10. Palomino, M.; Corma, A.; Rey, F.; Valencia, S., New insights on CO_2-methane separation using LTA zeolites with different Si/Al ratios and a first comparison with MOFs. *Langmuir* **2010,** *26* (3), 1910-7.

APPENDIX B. COUPLED-CLUSTER CORRECTIONS

B.1 Coupled-Cluster Corrections

Table B.1 - DFT/CC correction functions (in kJ/mol), ε, as a function of atom-atom distances (in Å) for C(CH_4_sp^3)–H and H(CH_4_sp^3)–H. The values are from Fang et al.[1]

C–H		H-H	
R	ε	R	ε
1.028500	4.421613	0.940275	20.303111
1.228500	-1.649292	1.140275	12.948228
1.428500	-4.692597	1.340275	7.846363
1.628500	-5.510554	1.540275	4.597372
1.828500	-5.175237	1.740275	2.661091
2.028501	-4.370377	1.940275	1.543186
2.228500	-3.493669	2.140275	0.918592
2.428500	-2.695524	2.340275	0.576983
2.628500	-2.003624	2.540275	0.381514
2.828500	-1.448442	2.740275	0.265680
3.028500	-1.009542	2.940274	0.187621
3.228500	-0.681713	3.140275	0.130930
3.428500	-0.448102	3.340275	0.088681
3.628500	-0.284233	3.540275	0.055541
3.828500	-0.174799	3.740275	0.031686
4.028500	-0.104261	3.940275	0.014796
4.228500	-0.060126	4.140275	0.003572
4.428500	-0.033094	4.340275	-0.003283
4.628500	-0.016863	4.540275	-0.007276
4.828500	-0.007317	5.040275	-0.010032
5.028500	-0.001763	5.540275	-0.008553
5.228500	0.001426	6.040275	-0.006271
5.428500	0.003175	6.540275	-0.004369
5.628500	0.004045	7.540275	-0.002104
6.128500	0.004343	8.540274	-0.001063
6.628500	0.003675	10.540274	-0.000329
7.128500	0.002877	13.540275	-0.000083
7.628500	0.002188	18.540275	-0.000014
8.628500	0.001242		
9.628500	0.000715		
11.628500	0.000259		
14.628500	0.000070		

Table B.2 - DFT/CC correction functions (in kJ/mol), ε, as a function of atom-atom distances (in Å) for C(CH_4_sp^3)–O and H(CH_4_sp^3)–O. The values are from Fang et al.[1]

C–O		H-O	
R	ε	R	ε
1.000000	39.435749	0.511770	19.319205
1.200000	41.889689	0.711770	43.390705
1.400000	30.152171	0.911770	36.468093
1.600000	9.226481	1.111770	22.516467
1.800000	-2.078451	1.311770	12.493685
2.000000	-5.047152	1.511770	6.257085
2.200000	-4.782019	1.711770	2.708901
2.400000	-3.725322	1.911770	0.829642
2.600000	-2.588161	2.111770	-0.073535
2.800000	-1.622315	2.311770	-0.430982
3.000000	-0.881114	2.511770	-0.519351
3.200000	-0.310735	2.711770	-0.489938
3.400000	0.076396	2.911770	-0.424704
3.600000	0.317434	3.111770	-0.360187
3.800000	0.453218	3.311770	-0.311596
4.000000	0.514985	3.511770	-0.272611
4.200000	0.526438	3.711770	-0.243692
4.400000	0.505876	3.911770	-0.219435
4.600000	0.467164	4.111770	-0.197887
4.800000	0.420307	4.311770	-0.178270
5.000000	0.371692	4.511770	-0.159306
5.200000	0.324969	4.711770	-0.140834
5.400000	0.281984	4.911770	-0.123537
5.600000	0.243478	5.411770	-0.087244
5.800000	0.209576	5.911770	-0.060210
6.000000	0.180083	6.411770	-0.041348
6.500000	0.123154	6.911770	-0.028841
7.000000	0.084789	7.911770	-0.015250
7.500000	0.059044	8.911770	-0.008967
8.000000	0.041649	10.911770	-0.003741
9.000000	0.021553	13.911770	-0.001213
10.000000	0.011733	18.911770	-0.000246
12.000000	0.003986		
15.000000	0.001039		
20.000000	0.000182		

Table B.3 - DFT/CC correction functions (in kJ/mol), ε, as a function of atom-atom distances (in Å) for C(CH_4_sp^3)–Si and H(CH_4_sp^3)–Si. The values are from Fang et al.[1]

C–Si		H-Si	
R	ε	R	ε
2.000000	-0.318700	0.511775	79.290411
2.200000	11.780354	0.711775	37.081318
2.400000	7.572454	0.911775	5.976599
2.600000	1.812180	1.111775	-7.226787
2.800000	-1.258563	1.311775	-1.707918
3.000000	-2.594931	1.511775	3.295968
3.200000	-3.142670	1.711775	4.014323
3.400000	-3.336754	1.911775	2.867216
3.600000	-3.339375	2.111775	1.633583
3.800000	-3.213222	2.311775	0.786968
4.000000	-2.994786	2.511775	0.402683
4.200000	-2.713014	2.711775	0.295461
4.400000	-2.401370	2.911775	0.311403
4.600000	-2.088665	3.111775	0.366559
4.800000	-1.793807	3.311775	0.422699
5.000000	-1.527348	3.511775	0.480176
5.200000	-1.293423	3.711775	0.499360
5.400000	-1.091984	3.911775	0.490854
5.600000	-0.920779	4.111775	0.465823
5.800000	-0.776589	4.311775	0.429392
6.000000	-0.655865	4.511775	0.387947
6.500000	-0.434273	4.711775	0.344740
7.000000	-0.292704	4.911775	0.301515
7.500000	-0.200962	5.411775	0.207404
8.000000	-0.140430	5.911775	0.141384
9.000000	-0.072020	6.411775	0.097295
10.000000	-0.039208	6.911775	0.068198
12.000000	-0.013506	7.911775	0.035959
15.000000	-0.003619	8.911775	0.020491
20.000000	-0.000656	10.911775	0.007560
		13.911775	0.002068
		18.911775	0.000362

Table B.4 - DFT/CC correction functions (in kJ/mol), ε, as a function of atom-atom distances (in Å) for C(CH_3_sp^3)–H, O, and Si. These DFT/CC correction functions were derived by Dr. Hanjun Fang.

C–H		C–O		C-Si	
R	ε	R	ε	R	ε
1.637231	-4.321009	1.594644	13.073242	2.328710	-3.275971
1.811222	-4.824518	1.772820	2.074104	2.518509	-3.552549
1.990107	-4.428149	1.955221	-2.356348	2.709777	-3.600420
2.172677	-3.710639	2.140768	-3.378366	2.902221	-3.572742
2.358077	-2.952966	2.328710	-3.104735	3.095624	-3.448293
2.545688	-2.275071	2.518509	-2.442194	3.289816	-3.254207
2.735055	-1.710712	2.709777	-1.751392	3.484665	-3.024285
2.925838	-1.260736	2.902221	-1.158595	3.680067	-2.769442
3.117776	-0.911930	3.095624	-0.685853	3.875937	-2.502179
3.310669	-0.646315	3.289816	-0.323980	4.072209	-2.237779
3.504358	-0.448503	3.484665	-0.060888	4.268828	-1.985332
3.698720	-0.304364	3.680067	0.117327	4.465746	-1.747526
3.893652	-0.201541	3.875937	0.228122	4.662927	-1.525588
4.089074	-0.129975	4.072209	0.288318	4.860338	-1.321363
4.284919	-0.081469	4.268828	0.312519	5.057953	-1.136769
4.481130	-0.049457	4.465746	0.312679	5.255748	-0.972939
4.677663	-0.028880	4.662927	0.297945	5.453704	-0.829892
4.874477	-0.015950	4.860338	0.274952	5.651804	-0.706645
5.071541	-0.007988	5.057953	0.248319	5.850033	-0.601511
5.268826	-0.003187	5.552737	0.182962	6.048379	-0.512428
5.466308	-0.000361	6.048379	0.131094	6.544684	-0.346000
5.663967	0.001246	6.544684	0.093677	7.041512	-0.237278
5.861785	0.002109	7.041512	0.067422	7.538759	-0.165502
6.059746	0.002521	8.036348	0.036128	8.036348	-0.117354
6.555191	0.002596	9.032325	0.020271	9.032325	-0.061766
7.051278	0.002193	10.029102	0.011838	10.029102	-0.034336
7.547882	0.001737	12.024263	0.004477	12.024263	-0.012163
8.044907	0.001343	15.019417	0.001293	15.019417	-0.003331
9.039941	0.000791	20.014567	0.000247	20.014567	-0.000613
10.035962	0.000472				
12.029984	0.000181				
15.023998	0.000053				
20.018005	0.000010				

Table B.5 - DFT/CC correction functions (in kJ/mol), ε, as a function of atom-atom distances (in Å) for C(CH_2_sp^3)–H, O, and Si. These DFT/CC correction functions were derived by Dr. Hanjun Fang.

C–H		C–O		C-Si	
R	ε	R	ε	R	ε
1.635898	-4.336771	1.593275	12.635018	2.327773	-0.599131
1.810018	-4.694191	1.771589	1.582387	2.517643	-1.388391
1.989011	-4.286843	1.954105	-2.779305	2.708972	-1.860185
2.171673	-3.609657	2.139749	-3.719612	2.901470	-2.137181
2.357152	-2.897443	2.327773	-3.426501	3.094920	-2.255679
2.544831	-2.256356	2.517643	-2.753391	3.289153	-2.249167
2.734258	-1.719278	2.708972	-2.070213	3.484039	-2.170778
2.925092	-1.285232	2.901470	-1.471807	3.679474	-2.051888
3.117076	-0.944823	3.094919	-0.980594	3.875375	-1.906835
3.310010	-0.680908	3.289153	-0.597752	4.071674	-1.745955
3.503735	-0.481215	3.484038	-0.309902	4.268317	-1.577552
3.698130	-0.333513	3.679474	-0.103001	4.465258	-1.407784
3.893092	-0.226228	3.875375	0.036821	4.662459	-1.241909
4.088540	-0.150068	4.071674	0.124275	4.859890	-1.084632
4.284409	-0.097461	4.268317	0.173128	5.057522	-0.939626
4.480643	-0.062119	4.465257	0.195027	5.255333	-0.809143
4.677196	-0.038968	4.662460	0.199128	5.453304	-0.694020
4.874030	-0.024096	4.859890	0.192251	5.651418	-0.593977
5.071110	-0.014674	5.057522	0.179271	5.849660	-0.507983
5.268412	-0.008760	5.552344	0.139107	6.048018	-0.434605
5.465909	-0.005070	6.048018	0.103053	6.544351	-0.296096
5.663582	-0.002776	6.544350	0.075452	7.041202	-0.204433
5.861413	-0.001355	7.041202	0.055305	7.538470	-0.143301
6.059386	-0.000479	8.036076	0.030367	8.036077	-0.101980
6.554858	0.000462	9.032083	0.017288	9.032083	-0.053927
7.050969	0.000651	10.028885	0.010187	10.028885	-0.030064
7.547593	0.000611	12.024081	0.003890	12.024081	-0.010686
8.044635	0.000514	15.019272	0.001131	15.019272	-0.002934
9.039699	0.000329	20.014458	0.000217	20.014458	-0.000541
10.035744	0.000204			2.327773	-0.599131
12.029803	0.000082			2.517643	-1.388391
15.023853	0.000025			2.708972	-1.860185
20.017896	0.000005			2.901470	-2.137181

Table B.6 - DFT/CC correction functions (in kJ/mol), ε, as a function of atom-atom distances (in Å) for C(CH_2_sp^2)–H and H(CH_2_sp^2)–H. These DFT/CC correction functions were derived by Dr. Hanjun Fang.

C–H		H-H	
R	ε	R	ε
1.594857	2.650164	1.181297	8.282367
1.773011	1.387160	1.299899	3.544842
1.955395	0.557350	1.436666	1.267825
2.140927	0.089000	1.586910	0.285735
2.328856	-0.142414	1.747157	-0.158319
2.518644	-0.229077	1.914897	-0.323162
2.709902	-0.231467	2.088326	-0.344348
2.902338	-0.190655	2.266138	-0.299418
3.095734	-0.133056	2.447377	-0.234000
3.289919	-0.075518	2.631336	-0.172283
3.484762	-0.027777	2.817482	-0.123118
3.680159	0.006115	3.005408	-0.089109
3.876025	0.026611	3.194801	-0.067225
4.072293	0.036020	3.385413	-0.054419
4.268907	0.037608	3.577052	-0.046908
4.465822	0.034515	3.769559	-0.041975
4.663000	0.029191	3.962808	-0.038035
4.860408	0.023291	4.156696	-0.034354
5.058020	0.017766	4.351137	-0.030666
5.255813	0.013049	4.546061	-0.026913
5.453766	0.009267	4.741407	-0.023222
5.651864	0.006376	4.937126	-0.019757
5.850091	0.004252	5.133175	-0.016635
6.048435	0.002738	5.329518	-0.013916
6.544736	0.000684	5.526123	-0.011609
7.041560	-0.000069	6.018615	-0.007370
7.538804	-0.000296	6.512251	-0.004707
8.036390	-0.000326	7.006789	-0.003034
9.032362	-0.000242	7.502052	-0.001977
10.029136	-0.000156	8.494242	-0.000872
12.024291	-0.000063	9.488072	-0.000411
15.019440	-0.000019	11.478948	-0.000112
20.014584	-0.000004	14.469982	-0.000024

Table B.7 - DFT/CC correction functions (in kJ/mol), ε, as a function of atom-atom distances (in Å) for C(CH_2_sp^2)–O and H(CH_2_sp^2)–O. These DFT/CC correction functions were derived by Dr. Hanjun Fang.

C–O		H-O	
R	ε	R	ε
1.202313	23.729176	1.021360	44.787599
1.373156	34.591510	1.121361	34.052742
1.550986	35.401670	1.245682	17.522263
1.733654	24.265856	1.387803	0.270187
1.919780	12.949444	1.542813	-4.569326
2.108449	6.379069	1.707204	-4.359831
2.299034	3.020313	1.878515	-3.660161
2.491095	1.366122	2.055017	-2.959595
2.684317	0.607358	2.235479	-2.331320
2.878464	0.303369	2.419017	-1.794330
3.073362	0.220939	2.604979	-1.360317
3.268877	0.236865	2.792882	-1.028849
3.464904	0.280811	2.982359	-0.789166
3.661360	0.319760	3.173128	-0.618202
3.858180	0.341379	3.364968	-0.497857
4.055312	0.344489	3.557708	-0.412320
4.252712	0.332664	3.751208	-0.349945
4.450343	0.310801	3.945356	-0.302217
4.648178	0.283403	4.140061	-0.263786
4.846190	0.253917	4.335249	-0.231450
5.044359	0.224672	4.530856	-0.203411
5.242667	0.197075	4.726831	-0.178620
5.441099	0.171851	4.923130	-0.156466
5.639642	0.149282	5.119715	-0.136601
5.838284	0.129374	5.316555	-0.118819
6.037016	0.111989	5.513622	-0.102995
6.534184	0.078094	6.007138	-0.071378
7.031753	0.054817	6.501646	-0.049292
7.529645	0.038875	6.996934	-0.034203
8.027799	0.027896	7.492848	-0.023972
9.024719	0.014910	8.486114	-0.012251
10.022253	0.008367	9.480797	-0.006617
12.018551	0.002996	11.472935	-0.002237
15.014845	0.000827	14.465212	-0.000583
20.011136	0.000153	19.457626	-0.000102

Table B.8 - DFT/CC correction functions (in kJ/mol), ε, as a function of atom-atom distances (in Å) for C(CH_2_sp^2)–Si and H(CH_2_sp^2)–Si. These DFT/CC correction functions were derived by Dr. Hanjun Fang.

C–Si		H-Si	
R	ε	R	ε
1.919777	-23.872846	1.201603	49.818555
2.108449	-19.179455	1.338290	38.224156
2.299034	-13.913565	1.489359	29.727466
2.491095	-9.723688	1.650866	21.517897
2.684316	-7.325674	1.820035	14.324078
2.878464	-5.819861	1.994918	8.898335
3.073362	-4.705512	2.174136	5.561876
3.268877	-3.828545	2.356700	3.481488
3.464904	-3.116580	2.541890	2.172340
3.661359	-2.534511	2.729171	1.380002
3.858180	-2.063261	2.918141	0.904341
4.055312	-1.680758	3.108491	0.625291
4.252712	-1.367675	3.299983	0.469157
4.450344	-1.110381	3.492428	0.379007
4.648178	-0.899510	3.685678	0.320372
4.846190	-0.727843	3.879613	0.278568
5.044359	-0.589211	4.074134	0.244833
5.242667	-0.477999	4.269161	0.215847
5.441099	-0.389135	4.464628	0.190273
5.639641	-0.318209	4.660479	0.167215
5.838283	-0.261521	4.856670	0.146189
6.037016	-0.216059	5.348380	0.102191
6.534184	-0.137066	5.841497	0.069483
7.031753	-0.089542	6.335693	0.046444
7.529645	-0.060043	6.830734	0.031024
8.027799	-0.041213	7.822709	0.014412
9.024719	-0.020642	8.816498	0.007207
10.022253	-0.011081	10.807513	0.002191
12.018550	-0.003759	13.798908	0.000518
15.014844	-0.000996	18.790665	0.000083
20.011136	-0.000179		

Table B.9 - DFT/CC correction functions (in kJ/mol), ε, as a function of atom-atom distances (in Å) for C(CH_sp^2)–H, O, and Si. These DFT/CC correction functions were derived by Dr. Hanjun Fang.

C–H		C–O		C-Si	
R	ε	R	ε	R	ε
1.594217	5.040973	1.201619	25.363925	1.919346	-22.211248
1.772435	2.736859	1.372548	33.301627	2.108053	-18.460250
1.954872	1.366945	1.550448	32.466028	2.298671	-13.314268
2.140450	0.568010	1.733173	19.215946	2.490761	-8.974438
2.328417	0.128577	1.919346	8.262308	2.684006	-6.047341
2.518239	-0.091776	2.108053	2.892661	2.878175	-4.031398
2.709525	-0.182170	2.298671	0.520415	3.073091	-2.696458
2.901987	-0.197836	2.490761	-0.460701	3.268622	-1.869542
3.095404	-0.174776	2.684006	-0.786264	3.464663	-1.366728
3.289609	-0.137180	2.878175	-0.802932	3.661132	-1.044452
3.484469	-0.099115	3.073091	-0.683940	3.857964	-0.821655
3.679881	-0.066669	3.268622	-0.519254	4.055107	-0.658713
3.875761	-0.041789	3.464663	-0.357012	4.252516	-0.534924
4.072042	-0.024439	3.661132	-0.219991	4.450156	-0.437884
4.268668	-0.013433	3.857964	-0.115412	4.647998	-0.360009
4.465594	-0.007146	4.055107	-0.041770	4.846018	-0.296712
4.662781	-0.004008	4.252516	0.006346	5.044194	-0.245113
4.860198	-0.002748	4.450156	0.035284	5.242508	-0.203117
5.057818	-0.002461	4.647998	0.050792	5.440946	-0.168996
5.255619	-0.002584	4.846018	0.057431	5.639494	-0.141261
5.453579	-0.002802	5.044194	0.058539	5.838141	-0.118655
5.651684	-0.002967	5.242508	0.056414	6.036877	-0.100145
5.849917	-0.003028	5.440946	0.052567	6.534056	-0.066795
6.048266	-0.002988	5.639494	0.047949	7.031635	-0.045579
6.544580	-0.002614	5.838141	0.043134	7.529534	-0.031679
7.041415	-0.002107	6.036877	0.038450	8.027695	-0.022369
7.538669	-0.001633	6.534056	0.028248	9.024627	-0.011647
8.036263	-0.001242	7.031635	0.020532	10.022170	-0.006401
9.032249	-0.000712	7.529534	0.014938	12.018481	-0.002226
10.029034	-0.000415	8.027695	0.010933	15.014789	-0.000599
12.024206	-0.000155	9.024627	0.006016	20.011094	-0.000109
15.019372	-0.000044	10.022170	0.003444		
20.014533	-0.000008	12.018481	0.001265		
		15.014789	0.000356		
		20.011094	0.000067		

Table B.10 - DFT/CC correction functions (in kJ/mol), ε, as a function of atom-atom distances (in Å) for O(H_2O)–H (H_2) and H(H_2O)–H (H_2).

O-H		H-H	
R	ε	R	ε
1.0	0.01108474546	1.8	0.00022484384
1.2	0.00856240421	2.0	0.00004341069
1.4	0.00422241904	2.2	-0.00000465456
1.6	0.00170656019	2.4	-0.00000303809
1.8	0.00057358488	2.6	0.00000247761
2.0	0.00007318553	2.8	0.00000430807
2.2	-0.00008508218	3.0	0.00000372247
2.4	-0.00009243158	3.2	0.00000236901
2.6	-0.00006019137	3.4	0.00000107852
2.8	-0.00003004439	3.6	0.00000011019
3.0	-0.00001040543	3.8	-0.00000052828
3.2	0.00000042852	4.0	-0.00000090507
3.4	0.00000560675	4.2	-0.00000109493
3.6	0.00000755830	4.4	-0.00000115918
3.8	0.00000782064	4.6	-0.00000114353
4.0	0.00000728391	4.8	-0.00000108053
4.2	0.00000643332	5.0	-0.00000099273
4.4	0.00000551788	5.5	-0.00000075096
4.6	0.00000465497	6.0	-0.00000054374
4.8	0.00000389163	6.5	-0.00000038798
5.	0.00000323918	7.0	-0.00000027639
5.5	0.00000204202	8.0	-0.00000014305
6.0	0.00000130265	9.0	-0.00000007721
6.5	0.00000084778	11.0	-0.00000002569
7.0	0.00000056414	14.0	-0.00000000651
8.0	0.00000026641	19.0	-0.00000000110
9.0	0.00000013578		
11.0	0.00000004234		
14.0	0.00000001025		
19.0	0.00000000168		

Table B.11 - DFT/CC correction functions (in kJ/mol), ε, as a function of atom-atom distances (in Å) for $O(H_2O)$–H (H_2O) and $O(H_2O)$–$O(H_2O)$.

O-H (H_2O-H_2O)		O-O	
R	ε	R	ε
1.0	0.00223892	1.8	0.003743158545
1.2	0.00186688	2.0	0.001518269383
1.4	0.00094841	2.4	0.000629773464
1.6	0.00020084	2.6	0.000671598180
1.8	-0.00023578	3.0	0.000734273505
2.0	-0.00044216	3.2	0.000708626928
2.2	-0.00049604	3.4	0.000655137639
2.4	-0.00047452	3.6	0.000586731180
2.6	-0.00042650	3.8	0.000513479582
2.8	-0.00036870	4.0	0.000441991536
3.0	-0.00031425	4.2	0.000376022838
3.2	-0.00027042	4.4	0.000317320460
3.4	-0.00023544	4.6	0.000266356267
3.6	-0.00020553	4.8	0.000222865041
3.8	-0.00017857	5.0	0.000186202941
4.0	-0.00015387	5.5	0.000119103680
4.2	-0.00013146	6.0	0.000077207410
4.4	-0.00011145	6.5	0.000050982831
4.6	-0.00009392	7.0	0.000034341157
4.8	-0.00007881	8.0	0.000016514220
5.0	-0.00006596	9.0	0.000008521319
5.5	-0.00004224	11.0	0.000002696887
6.0	-0.00002733	14.0	0.000000660222
6.5	-0.00001799	19.0	0.000000108702
7.0	-0.00001207		
8.0	-0.00000576		
9.0	-0.00000296		
11.0	-0.00000093		
14.0	-0.00000023		
19.0	-0.00000004		

Table B.12 - DFT/CC correction functions (in kJ/mol), ε, as a function of atom-atom distances (in Å) for $O(H_2O)$–$Si(Si_2O_7H_6)$ and $H(H_2O)$–$Si(Si_2O_7H_6)$.

Si-O		Si-H	
R	ε	R	ε
2.6	-0.016982159217	2.4	0.005167249658
3.0	-0.009441405098	2.6	0.003546235635
3.2	-0.006592827446	3.0	0.001186404729
3.4	-0.004430197788	3.2	0.000545845854
3.6	-0.002883183451	3.4	0.000166606615
3.8	-0.001834388049	3.6	-0.000036695020
4.0	-0.001157134485	3.8	-0.000130382563
4.2	-0.000737666808	4.0	-0.000161016772
4.4	-0.000485991836	4.2	-0.000159457126
4.6	-0.000337886486	4.4	-0.000144840542
4.8	-0.000251082129	4.6	-0.000127761858
5.0	-0.000199435621	4.8	-0.000112897757
5.5	-0.000138796601	5.0	-0.000101368682
6.0	-0.000110249437	5.5	-0.000082848701
6.5	-0.000088792037	6.0	-0.000070607304
7.0	-0.000070287300	6.5	-0.000059852552
8.0	-0.000042354982	7.0	-0.000049606868
9.0	-0.000025204146	8.0	-0.000032268654
11.0	-0.000009335219	9.0	-0.000020251307
14.0	-0.000002543973	11.0	-0.000007964787
19.0	-0.000000449601	14.0	-0.000002261192
		19.0	-0.000000410264

Table B.13 - DFT/CC correction functions (in kJ/mol), ε, as a function of atom-atom distances (in Å) for $O(O_2)$–H, O, and Si.

O-H		O–O		O-Si	
R	ε	R	ε	R	ε
1.20	2.8967800000	1.80	-1.4857200000	3.0023	-4.4963700000
1.40	0.8213600000	2.00	-3.0075300000	3.2023	-3.3157300000
1.60	-0.1167100000	2.20	-2.9956000000	3.4023	-2.3069800000
1.80	-0.4955600000	2.40	-2.3981300000	3.6023	-1.5237500000
2.00	-0.5210500000	2.60	-1.7050400000	3.8023	-0.9745500000
2.20	-0.4266000000	2.80	-1.1191000000	4.0023	-0.6156400000
2.40	-0.2909500000	3.00	-0.6857400000	4.2023	-0.3913300000
2.60	-0.1800200000	3.20	-0.4013100000	4.4023	-0.2560400000
2.80	-0.1011100000	3.40	-0.2283300000	4.6023	-0.1771900000
3.00	-0.0528200000	3.60	-0.1283200000	4.8023	-0.1325200000
3.20	-0.0269700000	3.80	-0.0734500000	5.0023	-0.1072600000
3.40	-0.0151600000	4.00	-0.0453000000	5.2023	-0.0920300000
3.60	-0.0114600000	4.20	-0.0319700000	5.4023	-0.0814200000
3.80	-0.0120600000	4.40	-0.0260900000	5.6023	-0.0726300000
4.00	-0.0141800000	4.60	-0.0233900000	5.8023	-0.0644500000
4.20	-0.0160500000	4.80	-0.0216700000	6.0023	-0.0566600000
4.40	-0.0168000000	5.00	-0.0199800000	6.5023	-0.0395300000
4.60	-0.0163300000	5.50	-0.0151800000	7.0023	-0.0264600000
4.80	-0.0149700000	6.00	-0.0105700000	7.5023	-0.0173600000
5.00	-0.0131400000	6.50	-0.0069900000	8.0023	-0.0113600000
5.50	-0.0085400000	7.00	-0.0045300000	9.0023	-0.0049700000
6.00	-0.0052000000	8.00	-0.0019000000	10.0023	-0.0023100000
6.50	-0.0031300000	9.00	-0.0008391440	12.0023	-0.0006016030
7.00	-0.0019000000	11.00	-0.0001993960	15.0023	-0.0001185970
8.00	-0.0007496000	14.00	-0.0000352414	20.0023	-0.0000158307
9.00	-0.0003212540			3.0023	-4.4963700000
11.00	-0.0000747414			3.2023	-3.3157300000
14.00	-0.0000131069			3.4023	-2.3069800000
19.00	-0.0000015371			3.6023	-1.5237500000
				3.8023	-0.9745500000
				4.0023	-0.6156400000

B.2 Appendix B References

1. Fang, H.; Awati, R.; Boulfelfel, S. E.; Ravikovitch, P. I.; Sholl, D. S., First-principles-derived force fields for CH_4 adsorption and diffusion in siliceous zeolites. *The Journal of Physical Chemistry C* **2018,** *122* (24), 12880-12891.

APPENDIX C. ADDITIONAL VALIDATION INFORMATION

C.1 Adsorption Isotherms

C.1.1 Methane

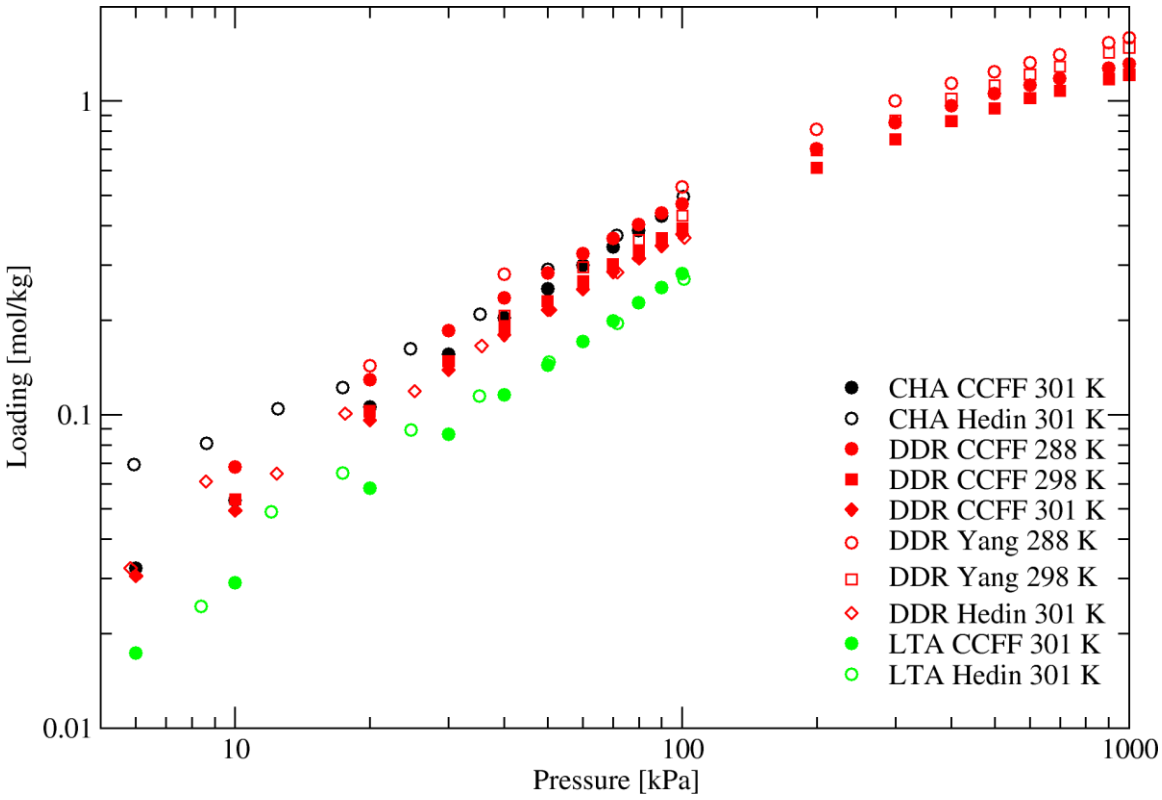

Figure C.1 - Simulated (filled) and experimental (open) methane adsorption isotherms are shown for CHA[1] (black), DDR[2] (red) and LTA[1] (green).

C.1.2 Ethane

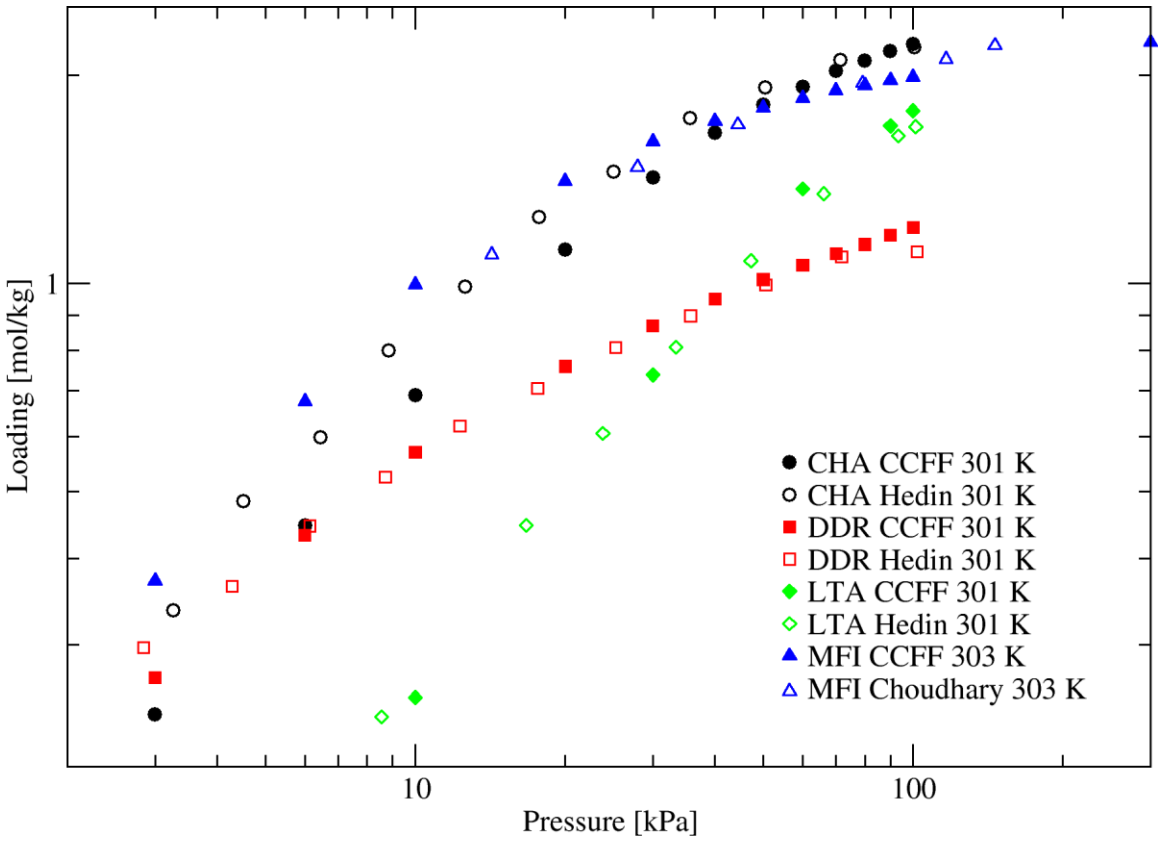

Figure C.2 - Simulated (filled) and experimental (open) ethane adsorption isotherms are shown for CHA[1] (black), DDR[1] (red), LTA[1] (green) and MFI[3] (blue).

C.1.3 Ethylene

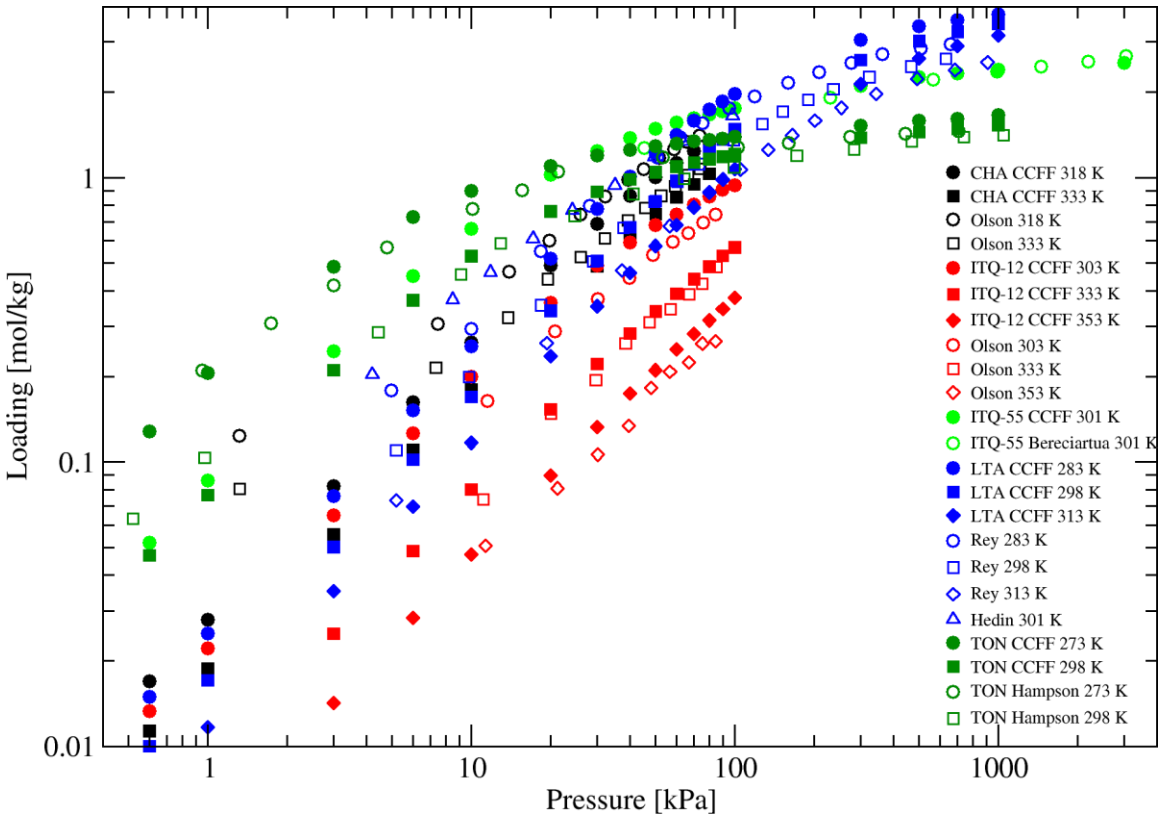

Figure C.3 - Simulated (filled) and experimental (open) ethylene adsorption isotherms are shown for CHA[4] (black), ITQ-12[4] (red), ITQ-55[5] (light green), LTA[1, 6] (blue), and TON[7] (dark green).

C.1.4 Propane

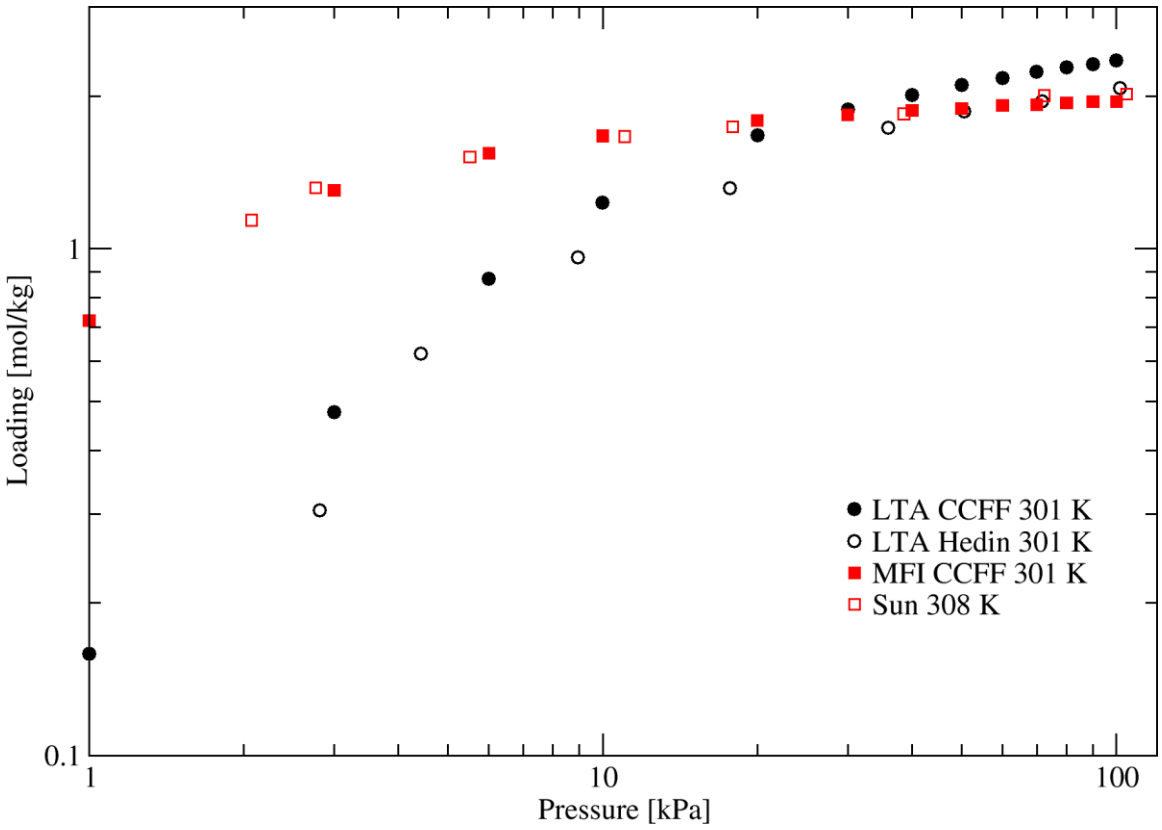

Figure C.4 - Simulated (filled) and experimental (open) propane adsorption isotherms are shown for LTA[1] (black), and MFI (red).

C.1.5 Propylene

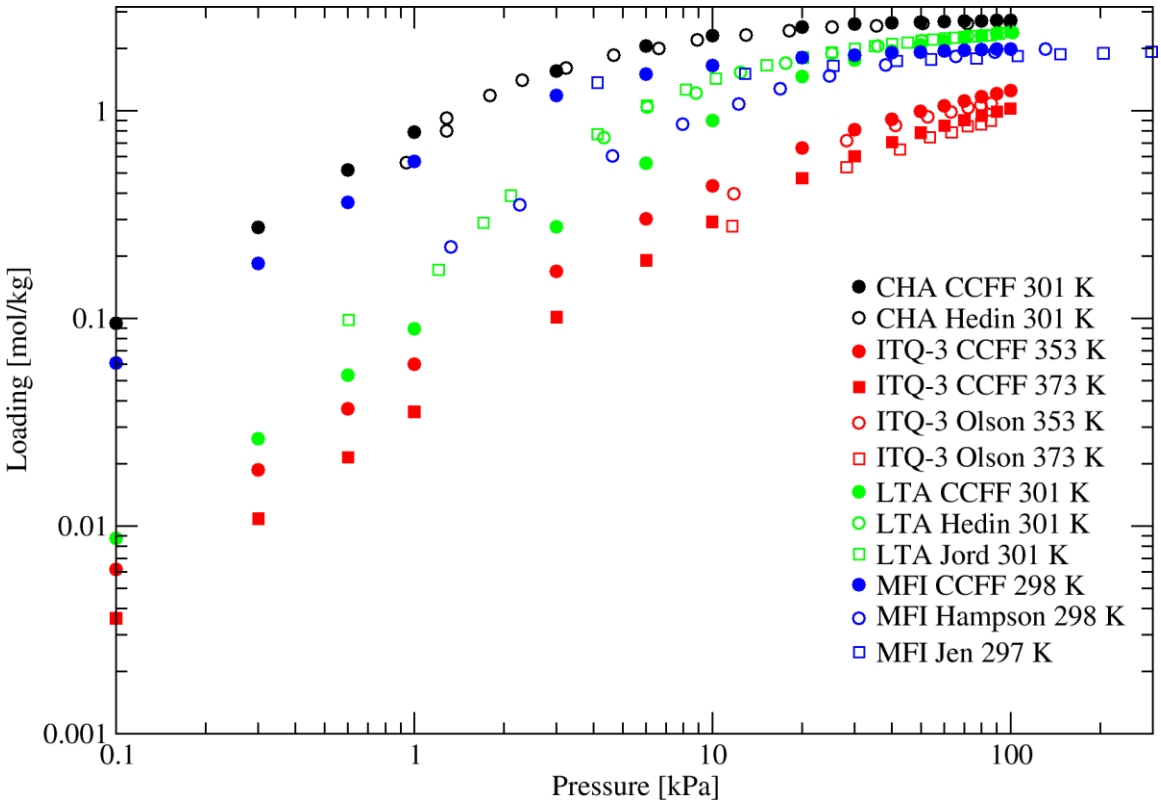

Figure C.5 - Simulated (filled) and experimental (open) propylene adsorption isotherms are shown for CHA[1] (black), ITQ-3[4] (red), LTA[1] (green) and MFI[7, 8] (blue)

C.2 Heats of Adsorption

C.2.1 Methane

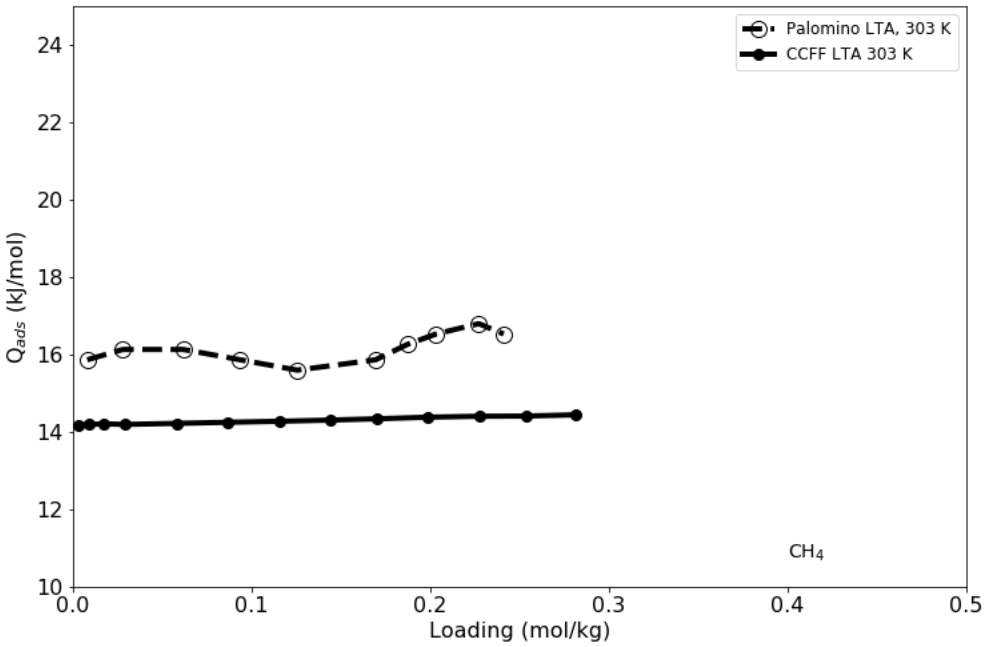

Figure C.6 - Simulated (filled) and experimental[9] (open) methane heats of adsorption are shown for LTA.

C.2.2 Ethane

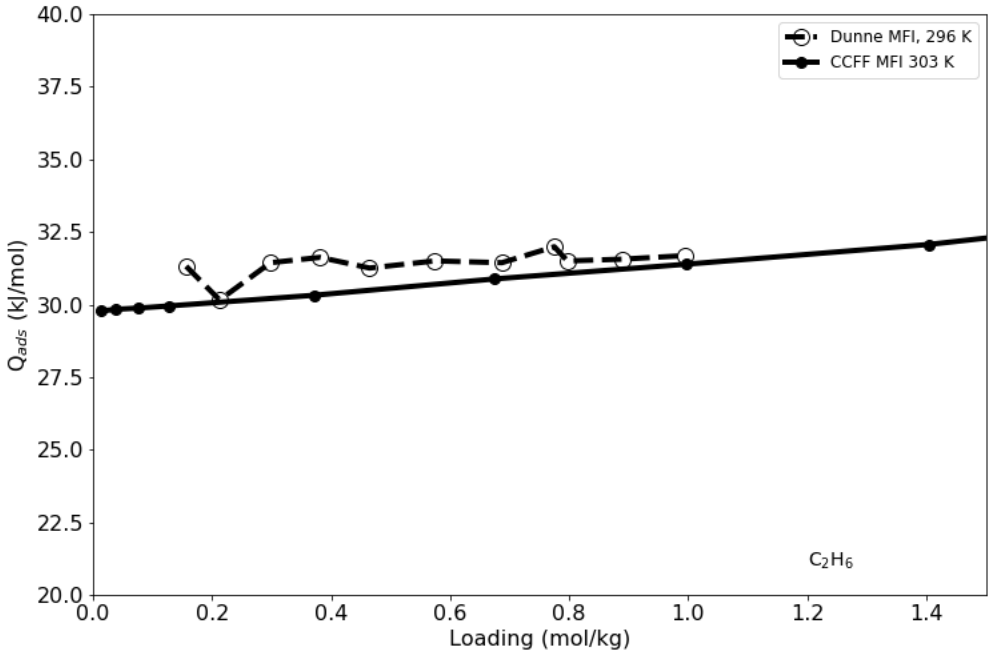

Figure C.7 - Simulated (filled) and experimental[10] (open) ethane heats of adsorption are shown for MFI.

C.3 FFs for Methane Adsorption and Diffusion Benchmarking

Table C.1 – A list of parameters taken from the literature and this work that were used to predict CH_4 adsorption isotherms and self-diffusivities in Figure 3.3 and Figure 3.8 respectively.

CH_4–O		CH_4–CH_4		CH_4–Si		Ref.	Code
σ [Å]	ϵ [K]	σ [Å]	ϵ [K]	σ [Å]	ϵ [K]		
3.510	200.334	4.482	221.000	–	–	[11]	FF1
3.140	180.410	3.817	148.176	2.140	34.879	[12-14]	FF2
3.460	97.421	3.817	148.176	2.140	34.879	[12, 13, 15]	FF3
3.140	97.421	3.817	148.176	2.140	34.879	[16]	FF4
3.214	133.263	3.730	147.936	–	–	[17, 18]	FF5
3.694	90.794	3.730	147.936	–	–	[19, 20]	FF6
3.370	118.415	3.740	149.920	–	–	[21]	FF7
3.600	96.459	3.730	148.056	–	–	[22]	FF8
3.370	75.772	3.440	221.303	3.750	135.909	[19]	FF9
3.080	141.000	3.882	137.000	–	–	[23]	FF10
3.515	88.570	3.730	148.000	3.015	57.061	[24]	FF11
3.470	115.000	3.720	158.500	–	–	[25-27]	FF12
3.885	97.625	3.880	216.900	–	–	[28]	FF13
3.501	104.5	3.737	151.400	–	–	[29]	FF14
3.417	**109.261**	**3.730**	**148.000**	**–**	**–**	**This Work**	**CCFF**

Table C.2 - A list of parameters taken from the literature and this work that were used to predict C_2H_6 adsorption isotherms and self-diffusivities in Figure 3.9.

CH_3–O		CH_3–CH_3		CH_3–Si		l_{C-C}	Ref.	Code
σ [$\AA$]	ϵ [K]	σ [$\AA$]	ϵ [K]	σ [$\AA$]	ϵ [K]	[$\AA$]		
3.775	184.740	–	–	–	–	1.54	[12]	FF1
3.364	83.800	3.923	72.000	–	–	1.53	[20, 30]	FF2
3.790	72.270	3.775	104.167	–	–	1.40	[31, 32]	FF3
3.600	79.982	3.770	98.143	–	–	1.53	[22, 33]	FF4
3.525	72.069	3.750	98.000	3.025	46.433	1.54	[24, 34]	FF5
3.480	93.000	3.760	108.000	–	–	1.54	[6, 25, 26]	FF6
3.480	94.106	3.760	108.000	–	–	1.54	[27]	FF7
3.640	87.500	3.905	88.060	–	–	1.53	[35]	FF8
3.170	141.922	3.780	104.157	2.120	82.147	1.54	[36]	FF9
3.600	79.982	3.770	98.143	–	–	1.54	[37]	FF10
3.403	**90.858**	**3.750**	**98.000**	**–**	**–**	**1.54**	**This Work**	**CCFF**

C.4 Appendix C References

1. Hedin, N.; DeMartin, G. J.; Roth, W. J.; Strohmaier, K. G.; Reyes, S. C., PFG NMR self-diffusion of small hydrocarbons in high silica DDR, CHA and LTA structures. *Microporous and Mesoporous Materials* **2008,** *109* (1-3), 327-334.

2. Yang, J.; Li, J.; Wang, W.; Li, L.; Li, J., Adsorption of CO_2, CH_4, and N_2 on 8-, 10-, and 12-membered ring hydrophobic microporous high-silica zeolites: DDR, silicalite-1, and beta. *Industrial & Engineering Chemistry Research* **2013,** *52* (50), 17856-17864.

3. Choudhary, V. R.; Mayadevi, S., Adsorption of methane, ethane, ethylene, and carbon dioxide on silicalite-l. *Zeolites* **1996,** *17* (5-6), 501-507.

4. Olson, D. H.; Camblor, M. A.; Villaescusa, L. A.; Kuehl, G. H., Light hydrocarbon sorption properties of pure silica Si-CHA and ITQ-3 and high silica ZSM-58. *Microporous and mesoporous materials* **2004,** *67* (1), 27-33.

5. Bereciartua, P. J.; Cantín, Á.; Corma, A.; Jordá, J. L.; Palomino, M.; Rey, F.; Valencia, S.; Corcoran, E. W.; Kortunov, P.; Ravikovitch, P. I., Control of zeolite framework flexibility and pore topology for separation of ethane and ethylene. *Science* **2017,** *358* (6366), 1068-1071.

6. Liu, B.; Smit, B.; Rey, F.; Valencia, S.; Calero, S., A new united atom force field for adsorption of alkenes in zeolites. *The Journal of Physical Chemistry C* **2008,** *112* (7), 2492-2498.

7. Hampson, J.; Rees, L., Fundamentals of Adsorption. Kodansha/Elsevier: Tokoy/Amserdam: 1993; pp 259-266.

8. Jen, H.; Otto, K., Chemisorption of alkenes on copper-exchanged ZSM-5 zeolite. *Catalysis letters* **1994,** *26* (1-2), 217-225.

9. Palomino, M.; Corma, A.; Rey, F.; Valencia, S., New Insights on CO_2− Methane separation using LTA zeolites with different Si/Al ratios and a first comparison with MOFs. *Langmuir* **2010,** *26* (3), 1910-1917.

10. Dunne, J.; Mariwala, R.; Rao, M.; Sircar, S.; Gorte, R.; Myers, A., Calorimetric heats of adsorption and adsorption isotherms. 1. O_2, N_2, Ar, CO_2, CH_4, C_2H_6, and SF_6 on silicalite. *Langmuir* **1996,** *12* (24), 5888-5895.

11. Yashonath, S.; Bandyopadhyay, S., Surprising Diffusion Behavior in the Restricted Regions of Silicalite. *Chem Phys Lett* **1994,** *228* (1-3), 284-288.

12. Haberlandt, R., Transport processes in porous media: diffusion in zeolites. *Thin Solid Films* **1998,** *330* (1), 34-45.

13. Fritzsche, S.; Haberlandt, R.; Karger, J.; Pfeifer, H.; Heinzinger, K., On the diffusion mechanism of methane in a cation-free zeolite of type ZK4. *Chem Phys* **1993,** *174* (2), 229-236.

14. Bezus, A. G.; Kiselev, A. V.; Lopatkin, A. A.; Du, P. Q., Molecular statistical calculation of the thermodynamic adsorption characteristics of zeolites using the atom–atom approximation. Part 1.—Adsorption of methane by zeolite NaX. *Journal of the Chemical Society, Faraday Transactions 2: Molecular and Chemical Physics* **1978,** *74*, 367-379.

15. Ruthven, D. M.; Derrah, R. I., Transition-state theory of zeolitic diffusion. Diffusion of CH_4 and CF_4 in 5A zeolite. *J Chem Soc Farad T 1* **1972,** *68* (12), 2332-&.

16. Fritzsche, S.; Haberlandt, R.; Wolfsberg, M., Equilibration of the kinetic energy in small zeolite cavities - The thermalization effect of lattice vibrations and of mutual interaction in the diffusion of methane in a cation-free LTA zeolite. *Chem Phys* **2000,** *253* (2-3), 283-294.

17. Jost, S.; Fritzsche, S.; Haberlandt, R., An MD study on the diffusion of a mixture of methane and xenon in silicalite. *Chem Phys Lett* **1997,** *279* (5-6), 385-388.

18. Goodbody, S. J.; Watanabe, K.; Macgowan, D.; Walton, J. P. R. B.; Quirke, N., Molecular Simulation of Methane and Butane in Silicalite. *J Chem Soc Faraday T* **1991,** *87* (13), 1951-1958.

19. Fritzsche, S.; Karger, J., Tracing memory effects in correlated diffusion anisotropy in MFI-type zeolites by MD simulation. *J Phys Chem B* **2003,** *107* (15), 3515-3521.

20. Hussain, I.; Titiloye, J. O., Molecular dynamics simulations of the adsorption and diffusion behavior of pure and mixed alkanes in silicalite. *Microporous and Mesoporous Materials* **2005,** *85* (1-2), 143-156.

21. Pascual, P.; Ungerer, P.; Tavitian, B.; Boutin, A., Development of a transferable guest-host force field for adsorption of hydrocarbons in zeolites. II. Prediction of alkenes adsorption and alkane/alkene selectivity in silicalite. *J Phys Chem B* **2004,** *108* (1), 393-398.

22. Leroy, F.; Rousseau, B.; Fuchs, A. H., Self-diffusion of n-alkanes in silicalite using molecular dynamics simulation: A comparison between rigid and flexible frameworks. *Physical Chemistry Chemical Physics* **2004,** *6* (4), 775-783.

23. Kamat, M.; Dang, W. J.; Keffer, D., Agreement between analytical theory and molecular dynamics simulation for adsorption and diffusion in crystalline nanoporous materials. *J Phys Chem B* **2004,** *108* (1), 376-386.

24. Bai, P.; Tsapatsis, M.; Siepmann, J. I., TraPPE-zeo: Transferable Potentials for Phase Equilibria Force Field for All-Silica Zeolites. *J Phys Chem C* **2013,** *117* (46), 24375-24387.

25. Dubbeldam, D.; Calero, S.; Vlugt, T. J. H.; Krishna, R.; Maesen, T. L. M.; Beerdsen, E.; Smit, B., Force field parametrization through fitting on inflection points in isotherms. *Phys Rev Lett* **2004,** *93* (8).

26. Dubbeldam, D.; Calero, S.; Vlugt, T. J. H.; Krishna, R.; Maesen, T. L. M.; Smit, B., United atom force field for alkanes in nanoporous materials. *J Phys Chem B* **2004,** *108* (33), 12301-12313.

27. Martin, M. G.; Thompson, A. P.; Nenoff, T. M., Effect of pressure, membrane thickness, and placement of control volumes on the flux of methane through thin silicalite membranes: A dual control volume grand canonical molecular dynamics study. *J Chem Phys* **2001,** *114* (16), 7174-7181.

28. Demontis, P.; Suffritti, G. B.; Fois, E. S.; Quartieri, S., Molecular-Dynamics Studies on Zeolites .6. Temperature-Dependence of Diffusion of Methane in Silicalite. *Journal of Physical Chemistry* **1992,** *96* (3), 1482-1490.

29. Talu, O.; Myers, A. L., Reference potentials for adsorption of helium, argon, methane, and krypton in high-silica zeolites. *Colloids and Surfaces A: Physicochemical and Engineering Aspects* **2001,** *187*, 83-93.

30. June, R. L.; Bell, A. T.; Theodorou, D. N., Molecular dynamics studies of butane and hexane in silicalite. *The Journal of Physical Chemistry* **1992,** *96* (3), 1051-1060.

31. Smit, B., Simulating the adsorption isotherms of methane, ethane, and propane in the zeolite silicalite. *The Journal of Physical Chemistry* **1995,** *99* (15), 5597-5603.

32. Jorgensen, W. L.; Madura, J. D.; Swenson, C. J., Optimized intermolecular potential functions for liquid hydrocarbons. *Journal of the American Chemical Society* **1984,** *106* (22), 6638-6646.

33. Vlugt, T.; Krishna, R.; Smit, B., Molecular simulations of adsorption isotherms for linear and branched alkanes and their mixtures in silicalite. *The Journal of Physical Chemistry B* **1999,** *103* (7), 1102-1118.

34. Martin, M. G.; Siepmann, J. I., Transferable potentials for phase equilibria. 1. United-atom description of n-alkanes. *The Journal of Physical Chemistry B* **1998,** *102* (14), 2569-2577.

35. Wang, Y.; Hill, K.; Harris, J. G., Confined thin films of a linear and branched octane. A comparison of the structure and solvation forces using molecular dynamics simulations. *The Journal of chemical physics* **1994,** *100* (4), 3276-3285.

36. Schüring, A.; Auerbach, S. M.; Fritzsche, S.; Haberlandt, R., On entropic barriers for diffusion in zeolites: A molecular dynamics study. *The Journal of chemical physics* **2002,** *116* (24), 10890-10894.

37. Macedonia, M. D.; Maginn, E. J., A biased grand canonical Monte Carlo method for simulating adsorption using all-atom and branched united atom models. *Molecular Physics* **1999,** *96* (9), 1375-1390.

APPENDIX D. ADDITIONAL CATION-FRAMEWORK VALIDATION

D.1 Cation-Framework Validation

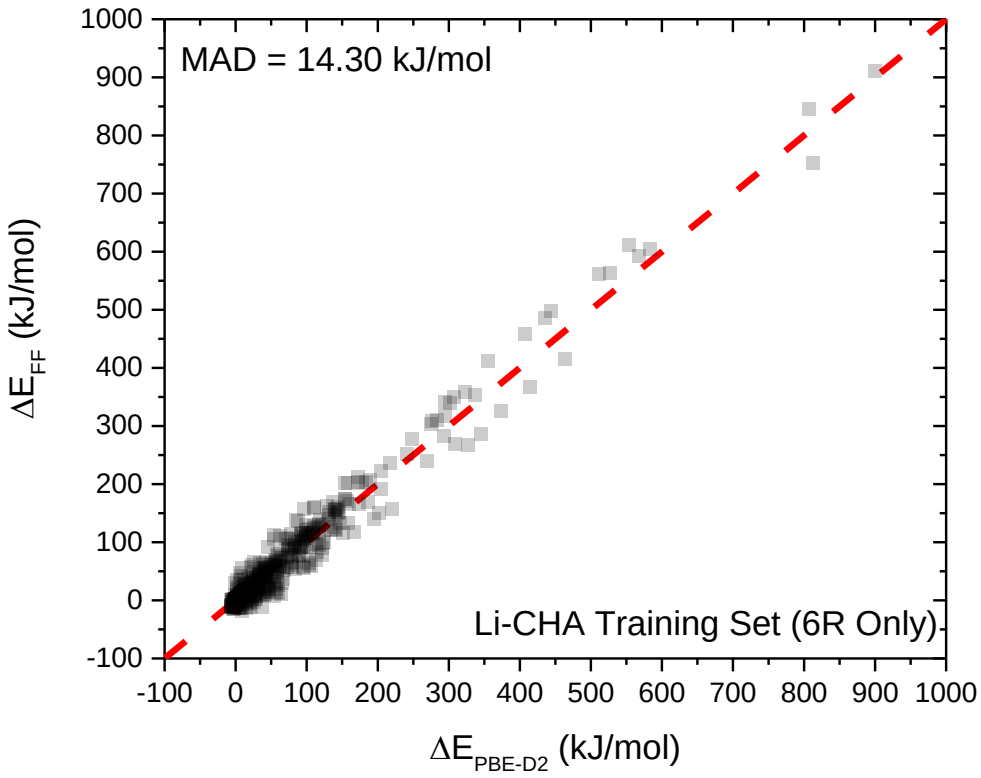

Figure D.1 – A comparison between PBE-D2 energies and FF energies that were fit to the PBE-D2 energies in Li-CHA. The label "6R Only" refers to the cation distribution in Li-CHA, where almost all cations are observed to occupy 6MR positions.

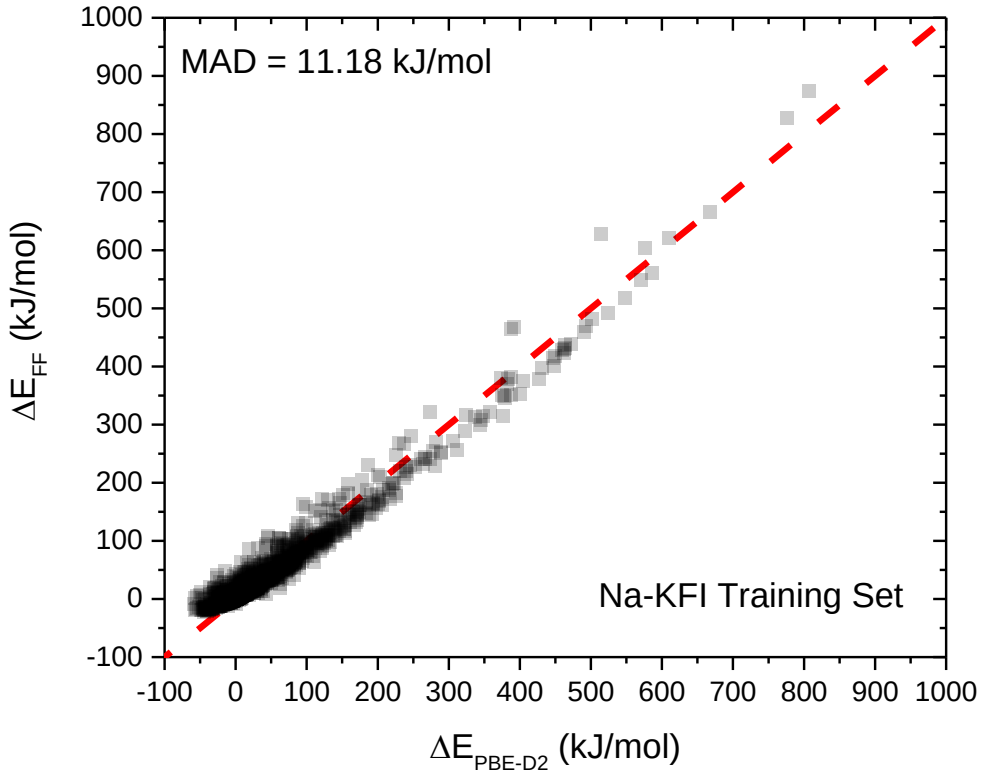

Figure D.2 - A comparison between PBE-D2 energies and FF energies that were fit to the PBE-D2 energies for this set of configurations in Na-KFI..

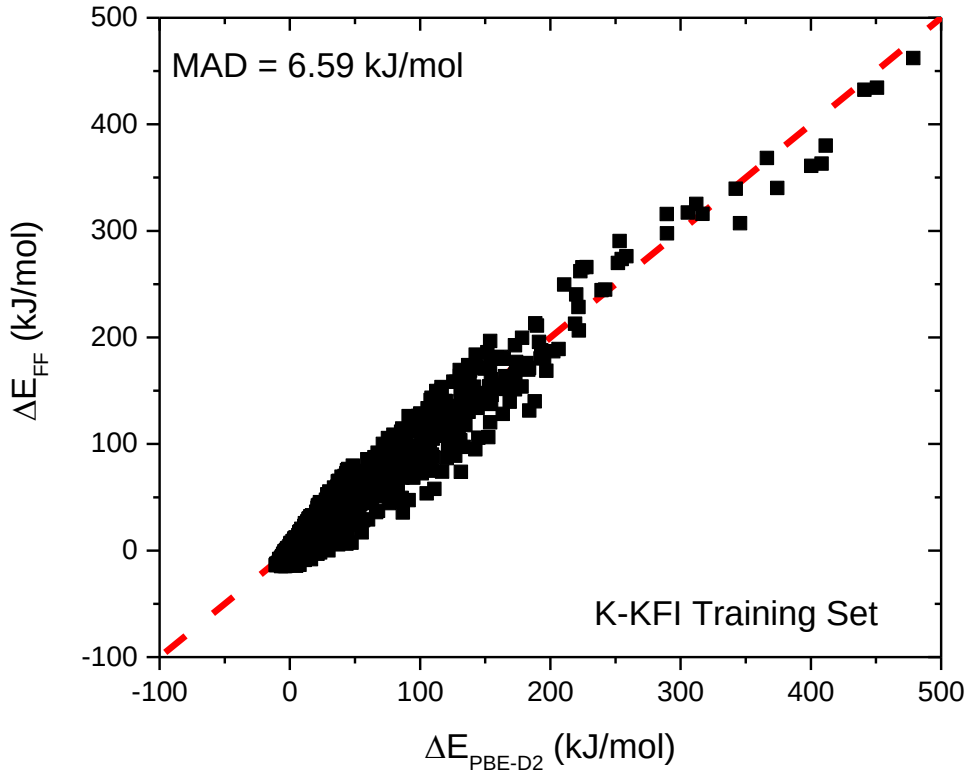

Figure D.3 - A comparison between PBE-D2 energies and FF energies that were fit to the PBE-D2 energies for this set of configurations in K-KFI.

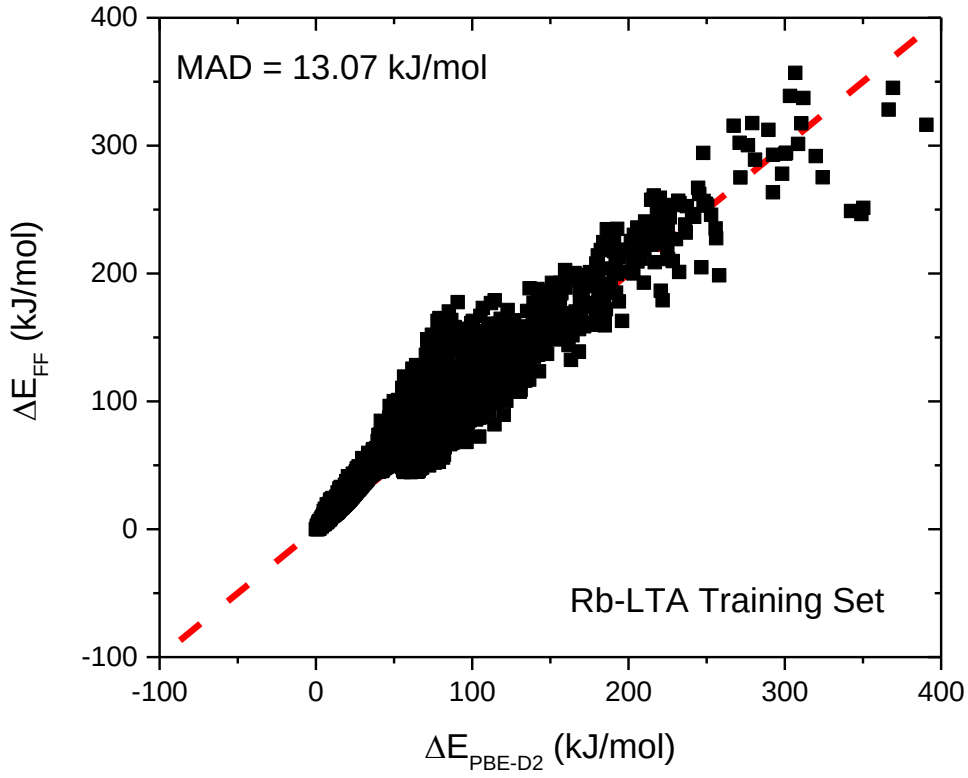

Figure D.4 - A comparison between PBE-D2 energies and FF energies that were fit to the PBE-D2 energies for this set of configurations in Rb-LTA.

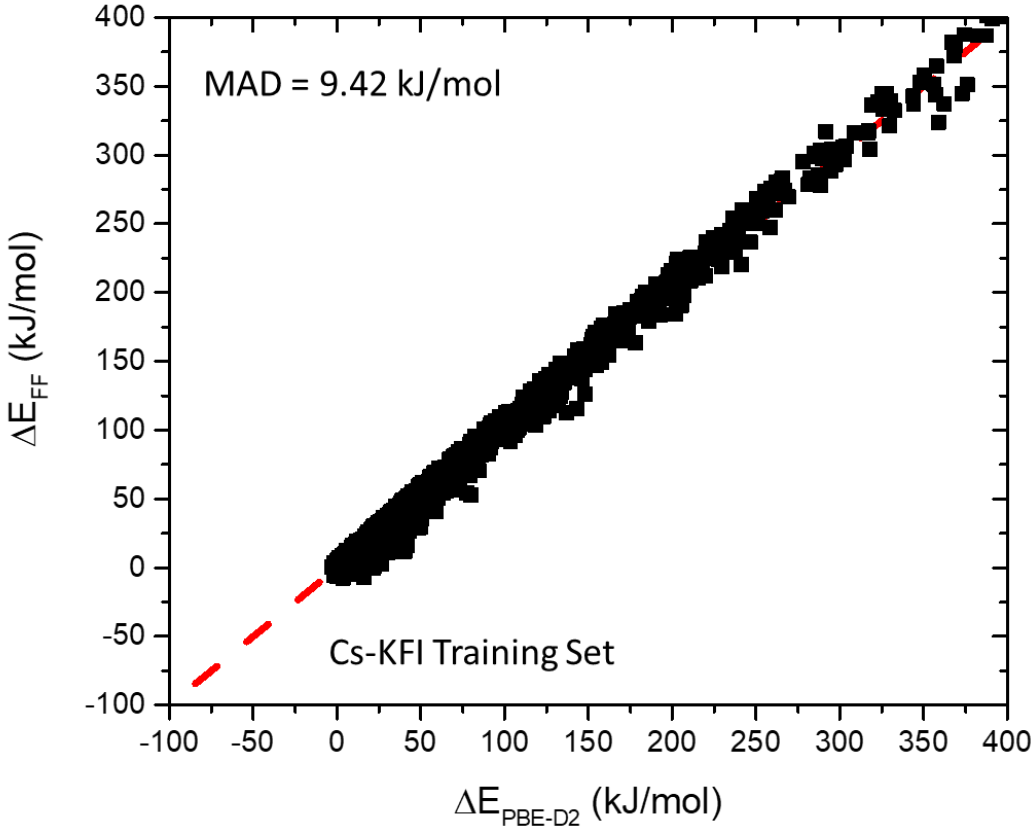

Figure D.5 - A comparison between PBE-D2 energies and FF energies that were fit to the PBE-D2 energies for this set of configurations in Cs-KFI.

The importance of correctly fitting cation-framework interactions was heavily emphasized in this work. Appendix D contains additional information on the validation for cation-framework interactions. To test the transferability of our Na-Oz interactions, we generated a set of configurations for Na in Na-RHO using the same methods as in Section 4.3.1. Figure D.6 shows a comparison between CCFF energies and PBE-D2 energies for these configurations. Good agreement is observed between the two quantities, which demonstrates the transferability of our FF.

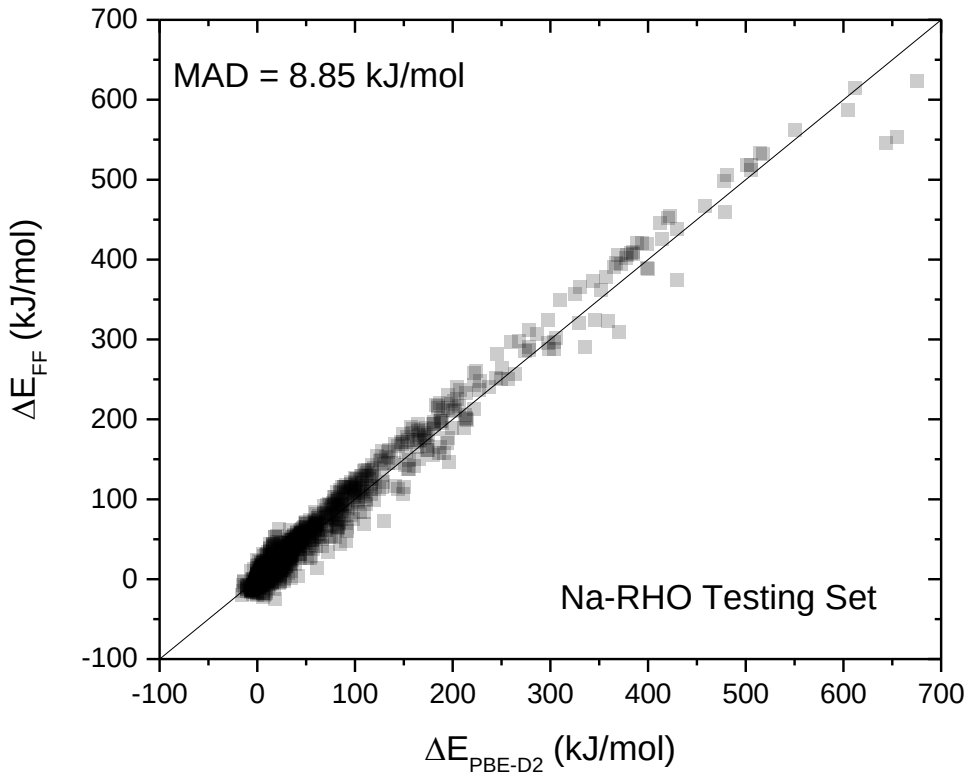

Figure D.6 – A comparison between PBE-D2 energies and energies calculated using the CCFF for different Na-distributions in Na-RHO. The Na configurations were generated using the same procedure as in Section 4.3.1.

The following tables show comparisons between simulated and experimental cation distributions for Na-LTA, Na-FAU, K-LTA, K-FAU and Cs-RHO. Our FF can accurately predict the cation distribution in these zeolites.

Table D.1 – A comparison between simulated and experimental cation positions in Na-LTA (Si/Al=1). The experimental data was taken from Pluth and Smith[1].

Na-LTA(Si/Al=1)	8 MR	6 MR	4 MR
Simulated	24	64	8
Expt. (Pluth and Smith)[1]	24	64	8

Table D.2 – A comparison between three sets of simulated cation positions and one set of experimental cation positions in Na-FAU (Si/Al = 2.5) is shown. The experimental data was taken from Jirak et al.[2]

Na-FAU(Si/Al=2.5)	SI	SI'	SII	SIII	Total
Simulated (Sparse)	16	3	31	5	55
Simulated (Random)	18	1	29	7	55
Simulated (Clustered)	0	16	25	14	55
Expt (Jirak et al.)[2]	18	4	32	1	55

Table D.3 – A comparison between experimental and simulated cation positions in K-LTA (Si/Al=2). The experimental results were taken from Ikeda et al.[3]

K-LTA(Si/Al=2)	8 MR	6 MR	4 MR
Expt. (Ikeda et al.)[3]	24	40	0
Simulated	21	43	0

Table D.4 – A comparison between two sets of experimental cation positions with simulated cation positions in K-FAU (Si/Al=2.5). The experimental results were taken from Mortier et al.[4] and Van Dun et al.[5]

K-FAU(Si/Al=2.5)	SI	SI'	SII	SIII	Total
Simulated	12	3	28	13	56
Expt. (Mortier et al., 1972)[4]	5	18	27	4	54
Expt. (Van Dun et al., 1985)[5]	6.5	6.5	30	13	56

Table D.5 – A comparison between experimental and simulated cation positions in Cs-RHO(Si/Al=3.9). The experimental results were taken from Losinzka et al.[6]

Cs-RHO (Si/Al=3.9)	D8R	S8R	6R
Expt. (Lozinska et al.)[6]	24	0	56
Simulated	21	0	59

D.2 Appendix D References

1. Pluth, J. J.; Smith, J. V., Accurate redetermination of crystal structure of dehydrated zeolite A. Absence of near zero coordination of sodium. Refinement of silicon, aluminum-ordered superstructure. *Journal of the American Chemical Society* **1980,** *102* (14), 4704-4708.

2. Jirak, Z.; Vratislav, S.; Bosáček, V., A neutron diffraction study of H, Na-Y zeolites. *Journal of Physics and Chemistry of Solids* **1980,** *41* (10), 1089-1095.

3. Ikeda, T.; Kodaira, T.; Oh, T.; Nisawa, A., K+ ion distribution in zeolite ZK-4's with various Si/Al ratios and the contribution of K+ ions to K cluster formation. *Microporous and mesoporous materials* **2003,** *57* (3), 249-261.

4. Mortier, W.; Bosmans, H.; Uytterhoeven, J., Location of univalent cations in synthetic zeolites of the Y and X type with varying silicon to aluminum ratio. II. Dehydrated potassium exchanged forms. *The Journal of Physical Chemistry* **1972,** *76* (5), 650-656.

5. Van Dun, J.; Mortier, W.; Uytterhoeven, J., Influence of the temperature and the adsorption of benzene on the location of K, Ca and Sr in Y-type zeolites. *Zeolites* **1985,** *5* (4), 257-260.

6. Lozinska, M. M.; Mowat, J. P.; Wright, P. A.; Thompson, S. P.; Jorda, J. L.; Palomino, M.; Valencia, S.; Rey, F., Cation gating and relocation during the highly selective "trapdoor" adsorption of CO_2 on univalent cation forms of zeolite RHO. *Chemistry of Materials* **2014,** *26* (6), 2052-2061.

APPENDIX E. ADDITIONAL MODEL DETAILS ADSORPTION VALIDATION (CATIONIC CCFF)

E.1 All-atom Model for CH_4

Table E.1 – The Lennard-Jones parameters for the new OPLS-AA model for CH_4 that was refit by Dr. Hanjun Fang.

Pairwise Interaction	ε (K)	σ (Å)	q (e)
C_ch4 – C_ch4	58.0	3.825	C_ch4 (-0.24)
H_ch4 – H_ch4	7.5	2.400	H_ch4 (+0.06)

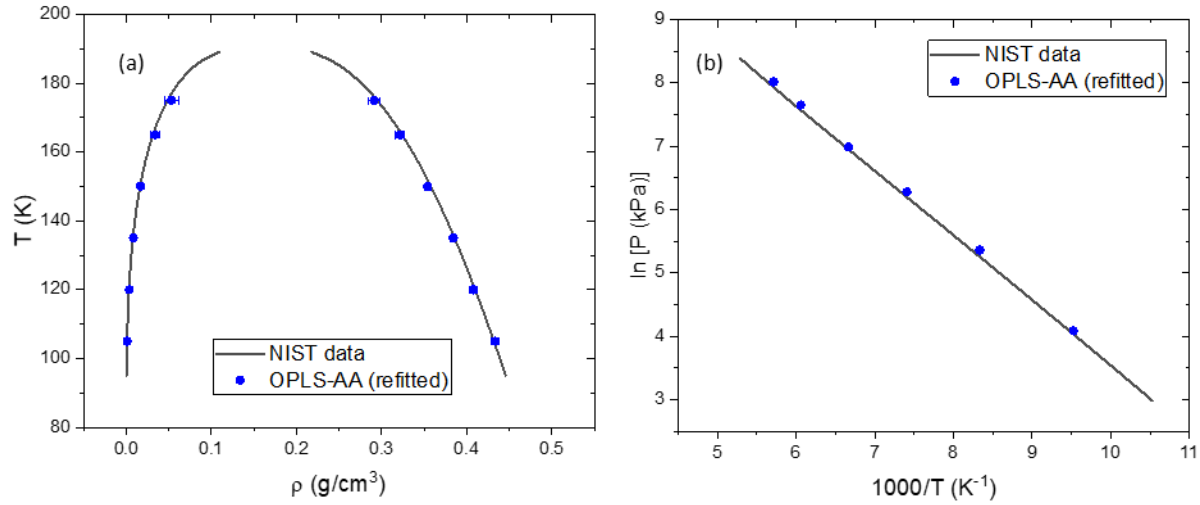

Figure E. 1 – Vapor-liquid coexistence curves for CH_4 were simulated with the OPLS-AA model and compared to experimental data from NIST[1]. Vapor and liquid density vs temperature are shown in (a) and saturation vapor pressure is shown in (b). Simulations and force field fitting for this model were performed by Dr. Hanjun Fang.

Table E.2 – The Lennard-Jones parameters for CH_4 interactions with a pure-silica zeolite. Parameters were fit by Dr. Hanjun Fang using the methods from Chapter 3.

Pairwise Interaction	ε (K)	σ (Å)	q (e)
C_ch4 – Si	35.14	3.830	C_ch4 (-0.24)
C_ch4 – O	20.56	3.378	H_ch4 (+0.06)
H_ch4 – Si	24.97	3.285	Si (1.8708)
H_ch4 - O	16.72	2.833	O (-0.9354)

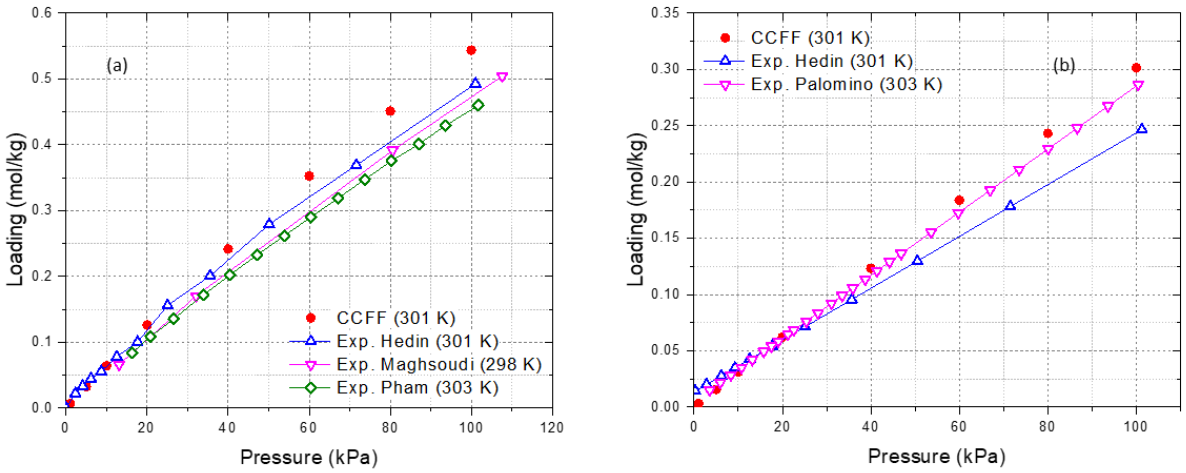

Figure E.2 – Simulated adsorption isotherms for the CCFF for all-atom CH_4 are compared to experimental adsorption isotherms in pure-silica CHA[2-4] (a) and pure-silica LTA[2, 5] (b). Simulations were performed by Dr. Hanjun Fang.

E.2 Additional Adsorption Isotherms

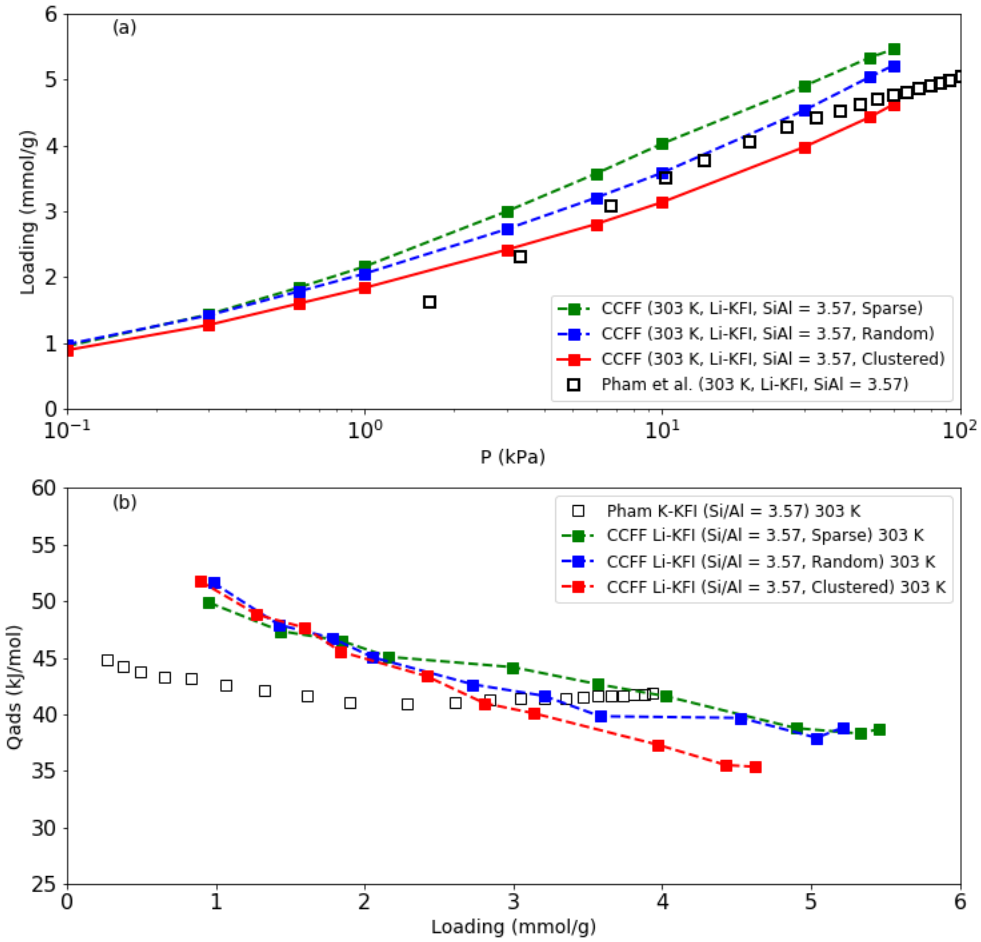

Figure E.3 - A comparison of simulated (filled symbols) CO_2 (a) adsorption isotherms and (b) heats of adsorption with experimental (open symbols) data[6] in Li-KFI (Si/Al=3.57). GCMC simulations using sparse (green), random (blue) and clustered (red) Al distributions were performed.

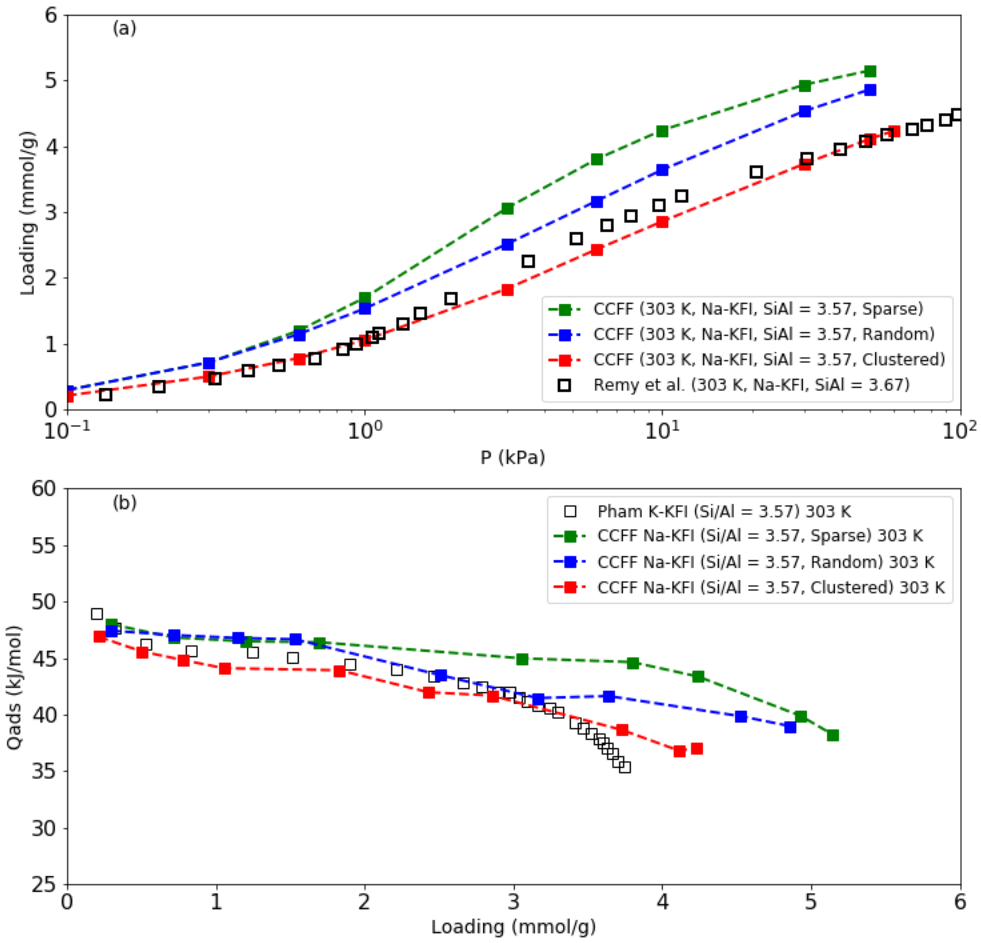

Figure E.4 - A comparison of simulated (filled symbols) CO_2 (a) adsorption isotherms and (b) heats of adsorption with experimental (open symbols) data[6] in Na-KFI (Si/Al=3.57). GCMC simulations using sparse (green), random (blue) and clustered (red) Al distributions were performed.

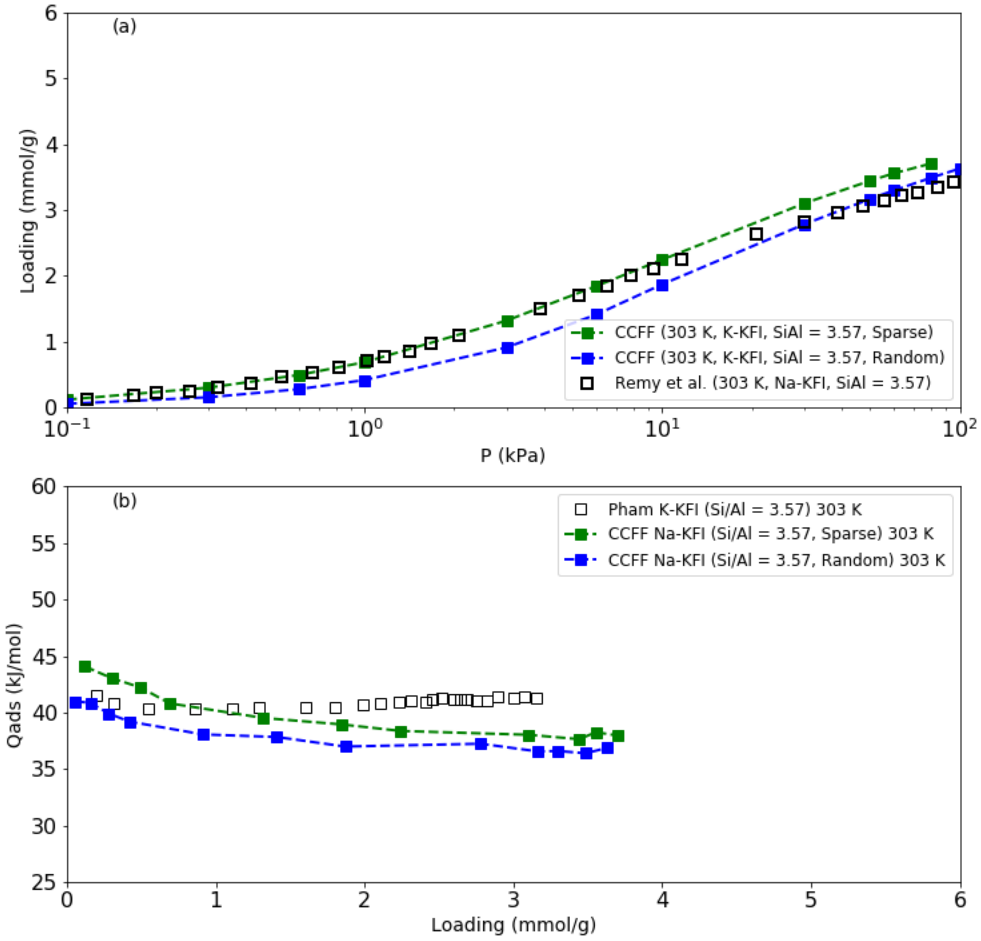

Figure E.5 - A comparison of simulated (filled symbols) CO_2 (a) adsorption isotherms and (b) heats of adsorption with experimental (open symbols) data[6] in K-KFI (Si/Al=3.57). GCMC simulations using sparse (green) and random (blue) Al distributions were performed.

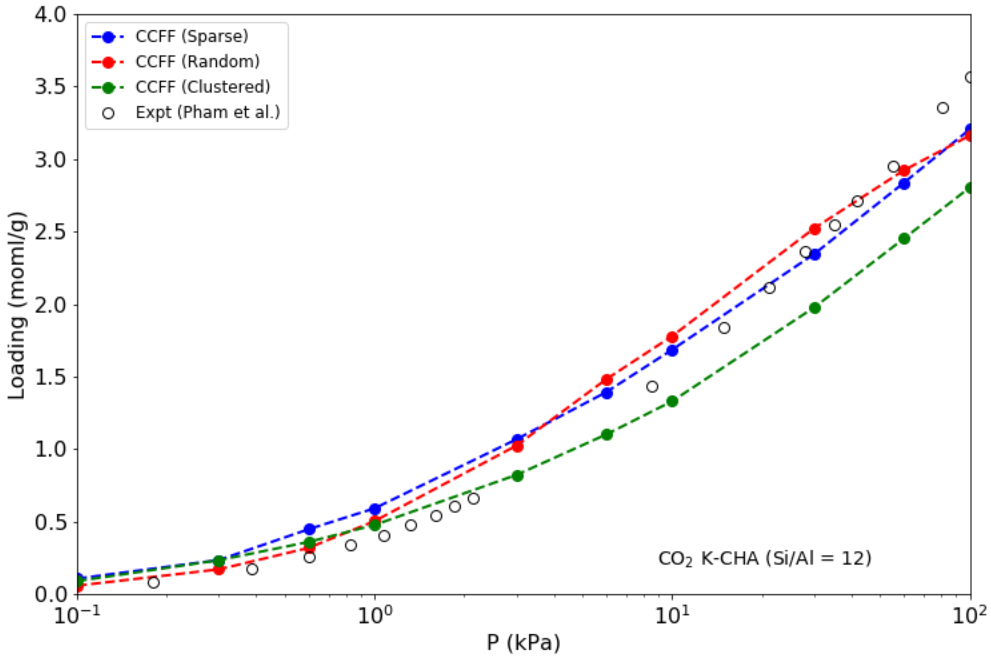

Figure E.6 - A comparison of simulated (filled symbols) CO_2 adsorption isotherms with experimental[7] (open symbols) adsorption isotherms in K-CHA (Si/Al=12). GCMC simulations using sparse (green), random (blue) and clustered (red) Al distributions were performed.

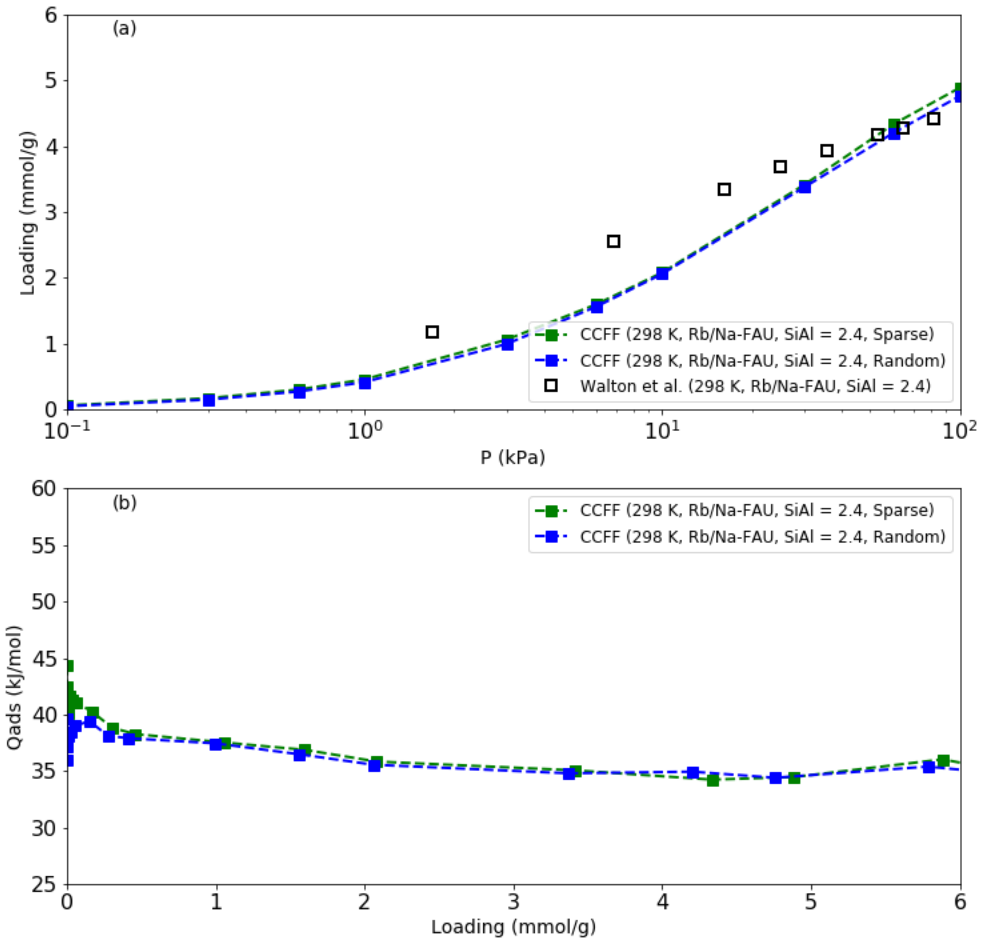

Figure E.7 - A comparison of simulated (filled symbols) CO_2 (a) adsorption isotherms with experimental (open symbols) adsorption isotherms[8] in Rb/Na-FAU (Si/Al=2.4). GCMC simulations using sparse (green) and random (blue) Al distributions were performed. The dependence of isosteric heat of adsorption on Al-distribution is shown in (b).

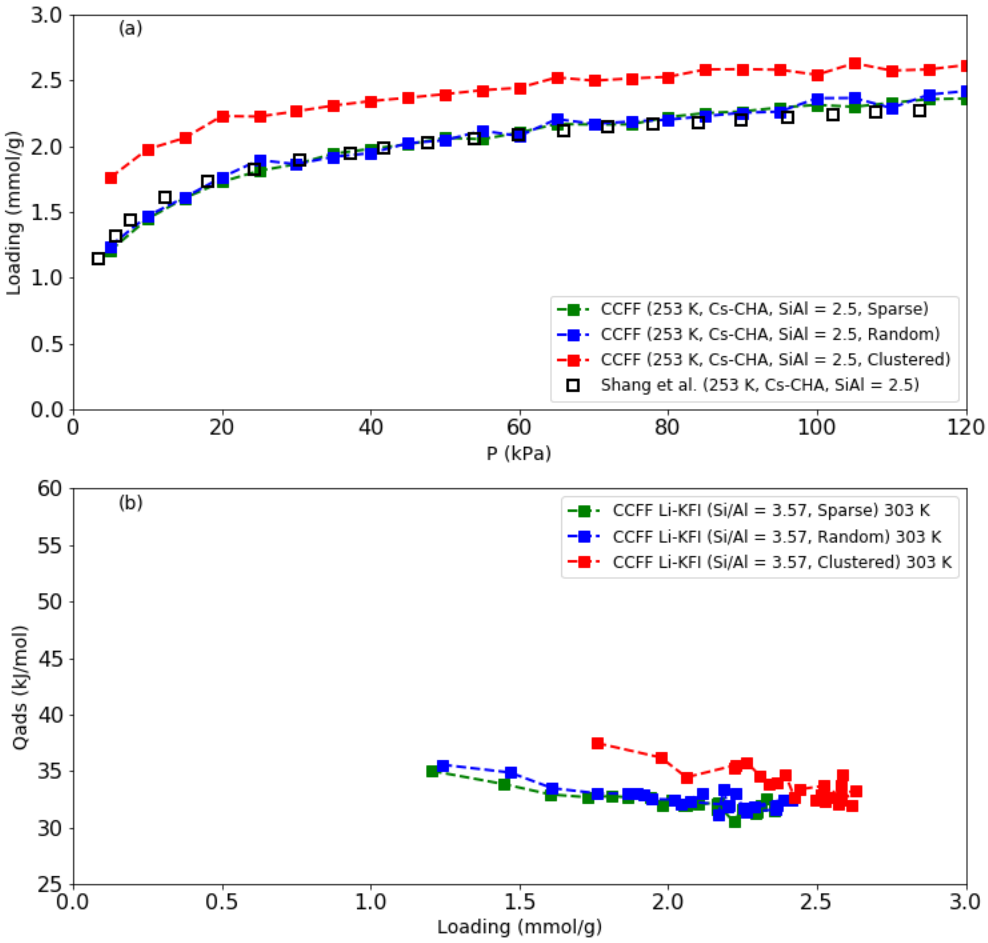

Figure E.8 - A comparison of simulated (filled symbols) CO_2 (a) adsorption isotherms with experimental (open symbols) adsorption isotherms[9] in Cs-CHA (Si/Al=2.5). GCMC simulations using sparse (green), random (blue), and clustered ()red Al distributions were performed. The dependence of isosteric heats of adsorption on Al-distribution is shown in (b). This set of GCMC simulations were performed by Alan Daou.

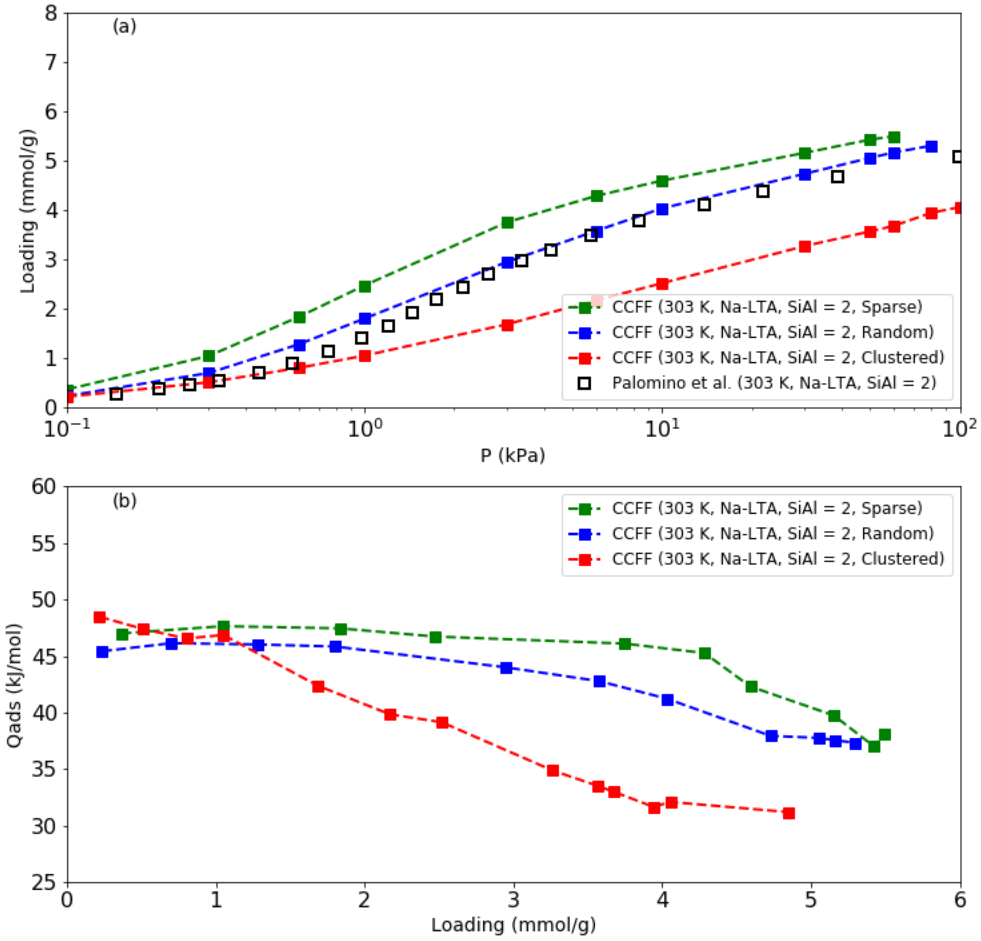

Figure E. 9 - A comparison of simulated (filled symbols) CO_2 (a) adsorption isotherms with experimental (open symbols) adsorption isotherms[5] in Na-LTA (Si/Al=2). GCMC simulations using sparse (green), random (blue), and clustered (red) Al distributions were performed. The dependence of isosteric heats of adsorption on Al-distribution is shown in (b).

E.3 Appendix E References

1. Lemmon, E. W.; McLinden, M. O.; Friend, D. G., Thermophysical properties of fluid systems. In *NIST Chemistry WebBook, NIST Standard Reference Database Number 69*, Linstrom, P. J.; Mallard, W. G., Eds. National Institute of Standards and Technology: Gaithersburg, MD, 20899, 1998.

2. Hedin, N.; DeMartin, G. J.; Roth, W. J.; Strohmaier, K. G.; Reyes, S. C., PFG NMR self-diffusion of small hydrocarbons in high silica DDR, CHA and LTA structures. *Microporous and Mesoporous Materials* **2008,** *109* (1-3), 327-334.

3. Maghsoudi, H.; Soltanieh, M.; Bozorgzadeh, H.; Mohamadalizadeh, A., Adsorption isotherms and ideal selectivities of hydrogen sulfide and carbon dioxide over methane for the Si-CHA zeolite: comparison of carbon dioxide and methane adsorption with the all-silica DD3R zeolite. *Adsorption* **2013,** *19* (5), 1045-1053.

4. Pham, T. D.; Lobo, R. F., Adsorption equilibria of CO_2 and small hydrocarbons in AEI-, CHA-, STT-, and RRO-type siliceous zeolites. *Microporous and Mesoporous Materials* **2016,** *236*, 100-108.

5. Palomino, M.; Corma, A.; Rey, F.; Valencia, S., New Insights on CO_2− Methane separation using LTA zeolites with different Si/Al ratios and a first comparison with MOFs. *Langmuir* **2010,** *26* (3), 1910-1917.

6. Pham, T. D.; Hudson, M. R.; Brown, C. M.; Lobo, R. F., On the Structure–Property Relationships of Cation-Exchanged ZK-5 Zeolites for CO_2 Adsorption. *ChemSusChem* **2017,** *10* (5), 946-957.

7. Pham, T. D.; Liu, Q.; Lobo, R. F., Carbon dioxide and nitrogen adsorption on cation-exchanged SSZ-13 zeolites. *Langmuir* **2013,** *29* (2), 832-839.

8. Walton, K. S.; Abney, M. B.; LeVan, M. D., CO_2 adsorption in Y and X zeolites modified by alkali metal cation exchange. *Microporous and Mesoporous Materials* **2006,** *91* (1-3), 78-84.

9. Shang, J.; Li, G.; Singh, R.; Gu, Q.; Nairn, K. M.; Bastow, T. J.; Medhekar, N.; Doherty, C. M.; Hill, A. J.; Liu, J. Z., Discriminative separation of gases by a "molecular trapdoor" mechanism in chabazite zeolites. *Journal of the American Chemical Society* **2012,** *134* (46), 19246-19253.